# Structural and chemical heterogeneity of Proterozoic organic microfossils of the ca. 1 Ga old Angmaat Formation, Baffin Island, Canada

Sami Nabhan, Linda C Kah, Bhoopesh Mishra, Kilian Pollok, Ashley R Manning-berg, Mark A Zuilen

▶ **To cite this version:**

Sami Nabhan, Linda C Kah, Bhoopesh Mishra, Kilian Pollok, Ashley R Manning-berg, et al.. Structural and chemical heterogeneity of Proterozoic organic microfossils of the ca. 1 Ga old Angmaat Formation, Baffin Island, Canada. Geobiology, 2021, 19 (6), pp.557 - 584. ⟨10.1111/gbi.12463⟩. ⟨hal-03426869⟩

**HAL Id: hal-03426869**

**https://hal.science/hal-03426869v1**

Submitted on 22 Nov 2021

**HAL** is a multi-disciplinary open access archive for the deposit and dissemination of scientific research documents, whether they are published or not. The documents may come from teaching and research institutions in France or abroad, or from public or private research centers.

L'archive ouverte pluridisciplinaire **HAL**, est destinée au dépôt et à la diffusion de documents scientifiques de niveau recherche, publiés ou non, émanant des établissements d'enseignement et de recherche français ou étrangers, des laboratoires publics ou privés.

HAL Authorization

# Structural and chemical heterogeneity of Proterozoic organic microfossils of the ca. 1 Ga old Angmaat Formation, Baffin Island, Canada

**Sami Nabhan [1], Linda C. Kah [2], Bhoopesh Mishra [3], Kilian Pollok [4], Ashley R. Manning-Berg [5], Mark A. van Zuilen [1]**

[1] Université de Paris, Institut de Physique du Globe de Paris, CNRS, F-75005 Paris, France

[2] Department of Earth and Planetary Sciences, University of Tennessee, Knoxville, TN, USA

[3] School of Chemical and Process Engineering, University of Leeds, Leeds, UK

[4] Institute of Geosciences, Friedrich Schiller University Jena, Jena, Germany

[5] Department of Biology, Geology and Environmental Science, University of Tennessee at Chattanooga, Chattanooga, TN, USA

## Abstract

Organic microfossils in Meso- and Neoproterozoic rocks are of key importance to track the emergence and evolution of eukaryotic life. An increasing number of studies combine Raman-spectroscopy with synchrotron-based methods to characterize these microfossils. A recurring observation is that Raman-spectra of organic microfossils show negligible variation on a sample scale and that variation between different samples can be explained by differences in thermal maturation or in the biologic origin of organic precursor material. There is a paucity of work, however, that explores the extent to which the petrographic framework and diagenetic processes might influence the chemical structure of organic materials. We present a detailed Raman-spectroscopy based study of a complex organic microfossil

assemblage in the ca. 1 Ga old Angmaat Formation, Baffin Island, Canada. This formation contains abundant early diagenetic chert that preserves silicified microbial mats with numerous, readily identifiable organic microfossils. Individual chert beds show petrographic differences with discrete episodes of cementation and recrystallization. Raman-spectroscopy reveals measurable variation of organic maturity between samples and between neighboring organic microfossils of the same taxonomy and taphonomic state. Scanning transmission X-ray microscopy performed on taphonomically similar coccoidal microfossils from the same thin section shows distinct chemical compositions, with varying ratios of aromatic compounds to ketones and phenols. Such observations imply that geochemical variation of organic matter is not necessarily coupled to thermal alteration or organic precursor material. Variation of the Raman signal across single samples is most likely linked to the diagenetic state of analyzed materials and implies an association between organic preservation and access to diagenetic fluids. Variation in the maturity of individual microfossils may be a natural outcome of local diagenetic processes and potentially exceeds differences derived from precursor organic material. These observations stress the importance of detailed in-situ characterization by Raman-spectroscopy to identify target specimens for further chemical analysis.

**Keywords**

Mesoproterozoic, organic microfossils, Angmaat Formation, Raman-spectroscopy

## 1. Introduction

### 1.1. Carbonization and graphitization of organic matter

Organic material (OM) in sedimentary and metasedimentary rocks experiences irreversible alteration that includes both carbonization and subsequent graphitization processes (Romero-Sarmiento et al., 2014; Buseck and Beyssac, 2014; Rouzaud et al., 2015; Delarue et al., 2016). Carbonization refers to the broad set of organic processes that take place at temperatures typically lower than approximately

330 °C, where OM becomes dehydrated, long chained organic molecules break down into shorter chains, and the ratio of aromatic molecules increases (Buseck and Beyssac, 2014; Rouzaud et al., 2015). These changes are frequently determined by proxies such as the H:C ratio which decreases with increasing degree of carbonization (Vendenbroucke and Largeau 2007; Ferralis et al., 2016). At low degrees of carbonization, equivalent to the oil window (50-150 °C), OM in Phanerozoic rocks can be further subdivided into three different types of kerogen with chemical fingerprints that have been crudely assigned to different organic precursor materials including lacustrine algae, marine and lacustrine planktonic algae, and terrestrial plants (Vendenbroucke and Largeau 2007). At higher degrees of carbonization, equivalent to the gas window (150-200 °C), organic precursor materials can be examined using a combination of analytic techniques including Raman-spectroscopy, micro-FTIR, micro-XANES and STXM (Bernard et al., 2007; Bernard et al., 2009; Qu et al., 2015 and 2018; Bonneville et al., 2020). These techniques, however, allow only for a limited assignment to the three primary domains of life, namely Archaea, Bacteria and Eukarya, and assignation is often limited to the simpler subdivision between Prokaryotes and Eukaryotes (Igisu et al., 2009; Qu et al., 2015). Nevertheless, such classification of organic precursor material is particularly interesting for Precambrian sedimentary rocks that may preserve evidence of the early emergence of eukaryotic life (Javaux et al., 2001; Knoll, 2014; Butterfield, 2015; Javaux and Lepot, 2018).

During metamorphism organic material experiences dominantly physical transformation to crystalline graphite while chemical transformations associated with carbonization gradually ceases (Beyssac et al., 2002; Buseck and Beyssac, 2014). This change is associated with the onset of graphitization at metamorphic temperatures of ca. 330 °C (Delarue et al., 2016). A direct correlation between increasing peak metamorphic temperature and the degree of graphite crystallinity has led to the widely accepted use of Raman spectroscopy as geothermometer to estimate maximum metamorphic temperatures (Beyssac et al., 2002; Rahl et al., 2005; Beyssac et al., 2007; Aoya et al., 2010; Lahfid et al., 2010; Kouketsu et al., 2014). Thermometry based on graphite crystallinity, however, is most reliable at a thermal alteration of the host rock between ca. 330 °C and 650 °C (Beyssac et al., 2002;

74 Rahl et al., 2005; Beyssac et al., 2007; Aoya et al., 2010). Above 650 °C OM is mostly, if not completely,
75 converted to graphite with a uniform and stable Raman signal (Beyssac et al., 2002). Furthermore,
76 chemical characterization of preserved microfossils is strongly limited to lower graphitization and only
77 possible in rare cases of pristine preservation by the use of nano-structural identification techniques
78 like STXM and TEM (Bernard et al., 2007; Bernard et al., 2009; Lepot et al., 2009).

79 The development of a variety of spectral fitting protocols to infer temperatures of maturation prior to
80 graphitization highlight spectral change derived from a number of ancillary spectral peaks (Sadezky et
81 al., 2005; Lahfid et al., 2010; Kouketsu et al., 2014; Lünsdorf et al., 2014a and b; Henry et al., 2019).
82 However, there is substantial difficulty in producing accurate geothermometers at temperatures
83 equivalent to burial diagenetic overprints (<150 °C) that reflect the lowest levels of carbonization
84 because most Raman parameters used to estimate thermal overprint do not show a linear behavior
85 at such low temperatures (Lahfid et al., 2010; Kouketsu et al., 2014; Henry et al., 2019). Other spectral
86 fitting techniques have been used to assign a Raman Index of Preservation (RIP; Schopf et al., 2005;
87 Czaja et al., 2016).

88 **1.2. Understanding maturity within Proterozoic microfossiliferous rocks**

89 Proterozoic sedimentary rocks that contain recognizable organic microfossils commonly preserve OM
90 that has undergone some extent of carbonization (in diagenetic and burial environments), but less
91 frequently have reached graphitization stages associated with metamorphism. Exceptions are
92 reported from extraordinary examples (Schopf et al., 2005). As noted above, in less thermally mature
93 samples Raman spectroscopy is commonly used to characterize the maturity (or degree of alteration)
94 of OM residues of individual microfossils (Schopf et al., 2005; Ferralis et al., 2016; Baludikay et al.,
95 2018; Guo et al., 2018; Manning-Berg et al., 2019; Pang et al., 2020). A commonality among most of
96 these studies is that the Raman signal is broadly homogeneous on a sample-, outcrop- and often even
97 formation-scale. The recent discovery of microfossiliferous units with heterogeneous Raman signals

led to the conclusion that the observed difference in the Raman signal must relate to differences in organic precursors (Qu et al., 2015; Pang et al., 2020).

It remains unclear, however, whether (and to what extent) small-scale differences in the diagenetic framework of geological samples may influence the maturity of the OM they host. Precambrian chert is well-known to preserve microfossils across an array of taphonomic states (Schopf et al., 2005; Edwards et al., 2012; Guo et al., 2018; Manning-Berg et al., 2019), and that microfossil-preserving chert can also show fabrics that potentially arise from discrete stages of silicification (Manning-Berg and Kah, 2017). Although the primary taphonomic differences reflect a time-frame of days to months (Bartley, 1996), we have little understanding of the role that diagenetic changes, including the timing of the precipitation of primary and secondary mineral phases, and the recrystallization of microfossil-associated diagenetic phases, may play in the maturation of preserved OM. It therefore remains to be determined whether, in low-temperature diagenetic environments, variation in maturity reflects differences in the diversity of organic precursors, or diagenesis.

Here we present a detailed investigation of chert from the ca. 1.0 Ga Angmaat Formation, Arctic Canada (Figure 1), that combines petrographic assessment of microfossiliferous and OM-bearing mineral phases with Raman-spectroscopy and Scanning transmission x-ray microscopy (STXM) of discrete organic phases. Microfossil assemblages in the strata of the Angmaat Formation experienced low-grade diagenesis involving silicification, diagenetic silica infill of structural voids, late-stage emplacement of dolomite veins, and dolomitic recrystallization of the carbonate host rock. To explore the extent to which discrete diagenetic episodes may affect the composition of OM, Raman spectroscopy was used to analyze and characterize OM (unrecognizable OM, microfossils, and distinct taphonomic states) within the context of their diagenetic history. STXM mapping was subsequently used to further characterize the organic chemistry of two coccoidal microfossils with distinct Raman-signals to determine the extent to which spectral differences can be correlated with the chemical composition of the organic microfossils. Our results indicate that small-scale variation in diagenetic

history, determined via changes in the petrographic framework of individual samples may have a greater effect on variation in the maturity of OM than the composition of microbial precursor materials.

## 2. Geological background

### 2.1. Geologic description of the Angmaat Formation

The Mesoproterozoic (~1.05 Ga; Gibson et al., 2018) Angmaat Formation, Bylot Supergroup, consists of ~500 meters of unmetamorphosed and undeformed carbonate exposed within the fault-bounded Borden Basin of northern Baffin and Bylot islands (Figure 1; Jackson and Iannelli, 1981; Kah et al., 1999; Turner, 2009). Initiation of carbonate deposition within the basin is marked by sea-level rise, restriction of terrigenous input into the basin and the formation of several discrete, deep-water carbonate build-ups associated with fault-derived fluids (Hahn et al., 2015). This is succeeded, with continued sea level rise, by carbonate ramp deposition that includes the laterally adjacent Angmaat and Nanisivik formations (which, along with the underlying Iqqittuq Formation, were formerly termed the Society Cliffs Formation; Turner, 2009). The Angmaat Formation is represented by a broad microbial flat in the southeastern regions of the basin, bounded to the west by an oolitic shoal. Periodic subaerial exposure of the oolitic shoal resulted in restriction and evaporation of associated nearshore environments that are dominated by microbial dolostone, sea floor precipitates, and abundant early diagenetic chert (Hofmann and Jackson, 1991; Kah and Knoll, 1996; Manning-Berg and Kah, 2017; Manning-Berg et al., 2019). Northwest of the oolitic shoal, offshore deposits of the carbonate ramp consist predominantly of finely laminated microbial dolostone and are referred to as the Nanisivik Formation (Turner, 2009).

Chert is common in the Angmaat Formation, although microfossil-bearing chert occurs almost exclusively within non-oolitic peritidal facies that are most prevalent southeast of the Milne Inlet (Jackson and Ianelli, 1981; Hofmann and Jackson, 1991; Kah and Knoll, 1996). Microfossil-bearing chert

148 is typically black in color, and occurs as cm-scale lenses and nodules and semi-continuous decimeter-
149 scale beds that can be traced for >100 meters along outcrop exposures. An early diagenetic origin is
150 inferred from exquisite microfossil preservation (Kah and Knoll, 1996; Knoll et al., 2013), the
151 preservation of mesoscale microbial fabrics, and the reworking of lithified chert fragments in syn-
152 depositional high-energy deposits. Later diagenetic chert phases are typically yellow to grey to white
153 in color, and occur as smooth nodules that cross-cut bedding features. With rare exception (cf.
154 Hofmann and Jackson, 1991), these nodules have not been found to be microfossil-bearing.

155 The presence of at least two diagenetic stages of chert formation, synsedimentary and late-stage,
156 dolomitization of the host carbonate (Kah 2000), and the presence of quartz-bearing, cross-cutting
157 veins indicate a complex diagenetic history of Angmaat chert. Although the timing of discrete
158 diagenetic events is unknown, the time-equivalent Nanisivik Formation hosts Mississippi-Valley-Type
159 (MVT) deposits, that mark a clear episode of fluid flow, although primary deposition of MVT deposits
160 occurred >300 km northwest of chert-bearing strata of the Angmaat Formation (Turner, 2009). Fluid
161 inclusion data from ore materials suggest temperatures of 165-210 °C for the main ore body
162 (McNaughton and Smith, 1986; Arne et al., 1991), potentially reaching 313 °C where the ore body is
163 intersected by mid-Neoproterozoic intrusive dikes. The vast majority of late-stage mineralization,
164 associated with late-stage MVT deposition, however, occurred at temperatures only near 100 °C (Arne
165 et al., 1991; Hnatyshin et al., 2016). Relatively low temperatures of the majority of Angmaat diagenesis
166 is consistent with initial Raman analysis of OM within Angmaat cherts (Manning-Berg et al., 2019) that
167 suggest the presence of dominantly immature organic matter.

168 **2.2. Micropaleontology and mineral associations of Angmaat chert**

169 Organic microfossils are abundant in black chert of the Angmaat Formation and display large
170 taxonomic (Knoll et al., 2013) and taphonomic (Manning-Berg et al., 2019) variation. Preserved
171 microfossils and associated organic material are remnants of microbial mats that formed in peritidal
172 evaporitic, carbonate- rich environments. Within these environments, subaqueous and lower

intertidal environments are dominated by filamentous communities (Kah and Knoll, 1996) consisting predominantly of sheaths of filamentous cyanobacteria, mainly *Siphonophycus capitaneum* (Nyberg and Schopf, 1984; Knoll et al., 2013) and *Eomicrocoleus crassus* (Horodyski and Donaldson, 1980; Nyberg and Schopf, 1984; Knoll et al., 2013). By contrast, more frequently exposed intertidal to supratidal environments are characterized by an increase in abundance of coccoidal populations, including *Eogloeocapsa bella* (Golovenok and Belova, 1984; Knoll et al., 2013), *Gloeodiniopsis* sp. (Schopf, 1968; Knoll and Golubic, 1979), and the colonial coccoid *Eoentophysalis blecherensis* (Hofmann, 1976).

Preserved microbial mats within Angmaat chert show both a range of taphonomic state, from well preserved microfossils to unrecognizable organic matter. Previous Raman analysis showed similar Raman spectra for organic microfossils of different taphonomic grade, consistent with taphonomic processes via natural decomposition, rather than by post-depositional diagenetic conditions (Manning-Berg et al., 2019). Angmaat chert, however, also preserve a variety of silicified and non-silicified mineral phases (Manning-Berg and Kah, 2017). Carbonate strata of the Angmaat Formation, for example, are fully dolomitized, and show evidence of primary precipitation of aragonite (Kah and Knoll, 1996) and both fabric-retentive and fabric-destructive dolomitization (Kah, 2000). Within chert phases, mats are indicative of more persistent subaqueous environments and commonly interlaminated with silicified carbonate drapes and a variety of distinct, sub-mm to mm-diameter voids (Knoll et al., 2013). Voids may represent structural elements within the mat that derive from microbial gas bubble production (Knoll et al., 2013; Bosak et al., 2010), from the post-depositional dissolution—and in rare cases, preservation—of mm-scale gypsum nodules (Kah, 2000), or from the post-depositional dissolution of micritic drapes. By contrast, mats associated with peritidal to supratidal environments are commonly associated with silicified aragonitic fans (Kah and Knoll, 1996; Knoll et al., 2013), silicified gypsum (Kah et al., 2001), and rare occurrences of silicified halite (Kah et al., 2001).

## 3. Background on Raman-spectroscopy of organic material

Raman spectra of organic material in sedimentary and metasedimentary rocks are generally subdivided into a first-order (ca. 1200 – 1700 $cm^{-1}$) and a second-order region (ca. 2500 – 3000 $cm^{-1}$) of which the first order region, which shows two distinct maximum intensity regions at ca. 1350 $cm^{-1}$ and at ca. 1600 $cm^{-1}$, is most commonly used to determine the degree of alteration of OM (Beyssac et al., 2002; Beyssac et al., 2007; Lahfid et al., 2010; Lünsdorf et al., 2014a and b). These peak regions, commonly referred to as the G- and D- kerogen peaks include both primary and secondary peaks that record changes in the carbon bonding (*sp2* and *sp3* hybridization) within OM resulting from loss of aliphatic Sp3 bonds and an increase in aromatic Sp2 bonds—and ultimately the degree of organization of aromatic features—during maturation. Primary peaks in this region are composed of a peak at 1580 $cm^{-1}$, commonly referred to as G-peak, that is caused by the in-plane $E_{2g}$ stretching of graphitic carbon bonds, and a peak at 1350 $cm^{-1}$, commonly referred to as D- (or D1-) peak, that reflects out-of-plane vibration of these bonds (Wopenka and Pasteris, 1993; Ferrari and Robertson, 2000; Beyssac et al., 2002; Sforna et al., 2014).

Secondary peaks include the D2-peak at 1620 $cm^{-1}$ that is caused by double resonance effects of defects in the crystalline structure of graphite, a D3-peak at ca. 1500 $cm^{-1}$ and a D4-peak at ca. 1250 $cm^{-1}$ (expressed as shoulders of the 1350 $cm^{-1}$ maximum), which are caused by out-of-plane defects, tetrahedrally coordinated carbon, dangling bonds, and heteroatoms (Guedes et al., 2010; Lahfid et al., 2010; Kouketsu et al., 2014; Ferralis et al., 2016). Additionally, in some analyses, the spectral region around D4 (1100 – 1300 $cm^{-1}$) is further divided into two peaks at ca. 1180 $cm^{-1}$ and 1250 $cm^{-1}$, referred to as the D4- and D5-peaks, respectively, and the spectral area region of the D3-peak (ca. 1380 – 1560 $cm^{-1}$), which forms the minimum between the two main D- (D1-) and G-peaks. This region is divided into two peaks at ca. 1420 $cm^{-1}$ and ca. 1540 $cm^{-1}$, both referred to as the D3-peaks (Guedes et al., 2010; Ferralis et al., 2016).

At low degrees of carbonization, the spectral maximum at 1600 $cm^{-1}$ is dominantly caused by aromatic ring-stretching vibrations, also known as "Я" motion of polycyclic aromatic hydrocarbons while the influence of the $E_{2g}$ stretching bonds of graphitic carbon is minor (Mapelli et al., 1999; Mayo et al., 2003; Schopf et al., 2005). This change in dominance often results in the use of a single peak solution for the spectral maximum at ca. 1600 $cm^{-1}$ of highly disordered OM, with the resulting peak inconsistently named as D2-, D2+G- or G-peak (Guedes et al., 2010; Kouketsu et al., 2014; Ferralis et al., 2016).

Within this scheme, the D1-, D2-, and G-peaks form the main components of Raman-spectra of highly mature OM that experienced graphitization or higher carbonization (Beyssac et al., 2002; Kouketsu et al., 2014). Disordered OM that experienced moderate carbonization commonly preserve evidence of the D3- and D4-peaks (Lahfid et al., 2010; Kouketsu et al., 2014). Highly disordered OM that experienced low degrees of carbonization preserve a greater number of structural defects and disorders, leading to preservation of a larger number of recognizable peak-shoulders around the 1350 $cm^{-1}$ maximum including the D3- and D5-peaks (Guedes et al., 2010; Ferralis et al., 2016) and the use of a single peak solution for the 1600 $cm^{-1}$ maximum (Guedes et al., 2010; Kouketsu et al., 2014; Ferralis et al., 2016).

## 4. Samples and Methods

Four samples of the Angmaat chert were analyzed in detail in this study (WWB-17-10, WWB-17-5, NL-17-M and NL-17-N). The first two of these were obtained from the west shore of White Bay (WWB), and the latter two from North Lake (NL; Figure 1; Table 1). All samples were collected from 3-10 cm thick black chert beds intercalated with dolomitic carbonate. One standard petrographic thin section of 30 µm thickness was prepared from each sample for microscopic and Raman-spectroscopic examination, and two were prepared from sample WWB-17-5 (A and B). Petrographic microscopy was performed to identify (1): the mineralogy of the samples (2): sedimentological and diagenetic features

and (3): organic material either preserved as organic microfossils or as unrecognizable organic material (UOM) with UOM including all forms of OM that are preserved in the analyzed samples and do not resemble or are not recognizable as distinct microfossils. Six double polished thin sections of ca. 50 µm thickness mounted with sodium silicate to avoid possible contamination with epoxy resin were prepared from sample WWB-17-5 for additional petrographic microscopy, Raman spectroscopy and preparation of FIB-foils for STXM-mapping. Sodium silicate is soluble in water and therefore the preparation procedure requires the use of ethanol for sawing and polishing while distilled water can be used to dissolve the mounting agent when sample transfer to different sample holders is needed.

### 4.1. Raman spectroscopy

Raman spectroscopy was performed on polished thin sections using the LabRAM HR Evolution instrument of the Department for Geosciences, Friedrich-Schiller-University Jena, Germany. This instrument has a focal length of 800 mm, and is equipped with a 532 nm and a 633 nm laser. We used a 600 l/mm grating and a 50 $cm^{-1}$ cut-off edge filter combined with a 1024 x 128-pixel EM-CCD detector. The central position of the spectrometer was set to 1350 $cm^{-1}$, recording the spectral region from ca. 530 $cm^{-1}$ to ca. 2100 $cm^{-1}$ for all measurements with the 532 nm laser and from ca. 800 $cm^{-1}$ to ca. 1860 $cm^{-1}$ for all spectra measured with a 633 nm laser. The technical resolution of the instrument is 1.86 $cm^{-1}$ for spectra acquired with the 532 nm laser and 1.3 $cm^{-1}$ for spectra acquired with the 633 nm laser. All acquired Raman spectra were calibrated for the Raman-shift ($cm^{-1}$) using an internal calibration objective with an imbedded polymer. This calibration was applied prior to each analytical session, after sample changes and changes of the setup like switching between lasers. We used an exposure time of 15 - 30 s with two accumulations for single point measurements and for line-maps of up to 20 points per line. The exposure time for area maps was 5 – 10 s per point with two accumulations at each point of the map. All maps were performed with an excitation wavelength of 532 nm. The laser intensity on the sample was measured with a handheld laser power meter “Coherent” from Edmund Optics. The maximum laser power on the samples surfaces was ca. 250 µW

for single point measurements and line-maps performed with a 532 nm laser and ca. 120 µW for measurements with a 633 nm laser. For the mapping performed with the 532 nm laser the power on the sample surface was approximately 520 µW. To avoid polishing effects, a 50X-VIS or 100X-VIS objective was focused on OM below the surface of transparent mineral phases (quartz or dolomite).

i. Spectral treatment

All single point spectra were consequently treated using the curve fitting software Fityk to estimate the maturation, to calculate H:C ratios, and to better understand maximum thermal alteration of the analyzed OM. The baseline of each spectrum was corrected with a second-order polynomial (Supplementary Figure 1). Because of the variable number of possible peaks (up to 7) the first order Raman spectrum of disordered OM requires complex fitting procedures. Several protocols have been developed to allow reproducible interpretations of Raman spectra of highly disordered OM (Sadezky et al., 2005; Schopf et al., 2005; Lahfid et al., 2010; Kouketsu et al., 2014; Rouzaud et al., 2015; Delarue et al., 2016; Ferralis et al., 2016). The protocols used in this study are described in detail below and a summary is shown in Table 2. The precision of the fit of each spectrum was determined graphically by subtracting the modeled spectra from the original spectra to obtain residual spectra (Supplementary Figures 2 and 3).

Area maps were treated using LabSpec 6 first with a baseline correction using second order polynomials and subsequently with classical least squares (CLS) fitting to define areas of similar spectral characteristics.

Raman spectra recorded with an excitation wavelength of 532 nm were initially characterized without using any peak-fitting procedure. The intensity values of the spectral maxima at ca. 1350 $cm^{-1}$ and ca. 1600 $cm^{-1}$, the intensity at 1540 $cm^{-1}$ and the full width at half maximum (FWHM) of the spectral maximum at ca. 1600 $cm^{-1}$ were extracted from all spectra. From these values the ratios I-1600/I-1350 and I-1540/I-1600 were calculated. The extracted values and calculated ratios were used to describe and visualize the progressive changes of the spectral area between ca. 1520 and ca. 1620 $cm^{-1}$.

Additionally, the intensity ratio I-1600/I-1350 and the FWHM of the 1600 $cm^{-1}$ spectral maximum were used for a first maturity estimate and to evaluate the needed peak-fitting method to calculate maximum thermal alteration.

After the initial characterization a 4-peak fit was applied (Figure 2a and Supplementary Figure 2) that allowed us to estimate the approximate maturation of OM and to calculate maximum thermal alteration (Kouketsu et al., 2014). This procedure usually involves the use of Pseudo-Voigt functions for spectral decomposition to avoid the breakdown of the use of Voigt functions for the decomposition of Raman spectra of low mature OM (Kouketsu et al., 2014). However, because peak decomposition with Pseudo-Voigt functions was largely inconclusive (Supplementary Figure 3) and because Pseudo-Voigt functions are mostly used to model Voigt functions if they are not applicable the procedure was performed using Voigt functions. For this procedure the spectral maximum at ca. 1600 $cm^{-1}$ was treated as a single peak referred to as D2-peak. A D1 and D2 peak were set with starting positions at ca. 1350 $cm^{-1}$ and ca. 1600 $cm^{-1}$ respectively. A D3 and D4 peak were set to fixed position at 1510 $cm^{-1}$ and 1245 $cm^{-1}$ respectively. The FWHM of D1 was then used to calculate maximum thermal overprint wherein T(D1) = -2.15(FWHM-D1) + 478. The error of T(D1) is estimated with ca. ±30°C (Kouketsu et al., 2014). A second geothermometer based on the FWHM-D2 was established by Kouketsu et al., 2014 but found to be less reliable. Therefore we refrained from reporting temperatures calculated with this geothermometer.

We used a 5-peak fitting procedure (Figure 2b and Supplementary Figure 2) suitable for OM that experienced a range of alteration reaching from moderate carbonization up to graphitization to potentially estimate the degree of carbonization of OM from the Angmaat Formation (Sadezky et al., 2005; Delarue et al., 2016). Spectra were decomposed as described in Delarue et al. (2016) using Lorentzian/Gaussian functions into a D1, D2, D3, D4 and G band with the D1 band being fixed to the maximum intensity of the D-area around 1350 $cm^{-1}$. This procedure requires a 2-peak fitting solution for the spectral maximum at ca. 1600 $cm^{-1}$ with a G-peak at ca. 1580 $cm^{-1}$ and a D2-peak at ca. 1620

323 $cm^{-1}$. From this analysis we then extracted the intensity ratio $R1_{(5p)}$ = D1/G and the FWHM of the D1-
324 and G-peaks.

325 A seven-peak fitting procedure was then used to deconvolute the same Raman spectra (532 nm) into
326 discrete and recognizable peak maxima and shoulders (Figure 2c and Supplementary Figure 2) using
327 Voigt functions. Similar procedures were used previously to describe Raman spectra of low mature
328 organic microfossils (Schopf et al., 2005; Ferralis et al., 2016). The procedure includes the disorder
329 bands D1 and D2, here defined with positions at ca. 1340 $cm^{-1}$ and ca. 1610 $cm^{-1}$ respectively. We
330 applied a 2-peak solution for the D3 region with a band at ca. 1415 $cm^{-1}$ and one at ca. 1540 $cm^{-1}$. A
331 D4 band is applied at ca. 1165 $cm^{-1}$ and a D5 band at ca. 1230 $cm^{-1}$. A weak G band was added at ca.
332 1570 $cm^{-1}$. All bands were applied in the order they are listed above. After deconvolution we extracted
333 the FWHM-D1, the FWHM-D2 and the position of the G-peak and calculated the intensity ratio $R1_{(7p)}$
334 = D1/D2 and the intensity ratio $R3_{(7p)}$ = D3/D2. The use of a particularly small G-peak in our
335 deconvolution procedure, consistent with the immaturity of OM in our samples, requires that we
336 define the intensity ratio $R1_{(7p)}$ as the intensity of the D1-peak divided by the intensity of the D2-peak
337 (D1/D2). This peak deconvolution procedure was used to visualize the progressive change of the
338 spectral maximum at 1600 $cm^{-1}$ mainly represented by the D2- and G-peaks and the R3 ratio.

339 Spectra recorded with an excitation wavelength of 633 nm were fitted with the procedure described
340 in Guedes et al., (2010) and Ferralis et al. (2016). This procedure is similar to the described seven-peak
341 procedure and includes the peaks at similar starting positions (Figure 2d and Supplementary Figure 2).
342 The Raman band at 1600 $cm^{-1}$ is treated with a single peak solution with the resulting peak named as
343 G-peak in Guedes et al., (2010) and as G+D2-peak in Ferralis et al., 2016. In this study the peak will be
344 referred to as (G+D2)-peak. The full width at half maximum of all peaks was restricted to a maximum
345 of 100 $cm^{-1}$. We extracted the intensity ratio D1/(G+D2) and the FWHM-D1. The intensity ratios of
346 D5/(G+D2) and of (D4+D5)/(G+D2) obtained from this fitting procedure were used to calculate H:C

ratios of OM, wherein H:C = 0.871 * D5/(G+D2) - 0.0508 and H:C = 0.6024 * (D4+D5)/(G+D2) - 0.0739 (Ferralis et al., 2016).

### 4.2. STXM

Two ultrathin foils of ca. 20 x 15 x 0.12 µm were prepared using a FIB single-beam instrument at the Institute de Physique du Globe de Paris (IPGP) following the procedure described by Wirth (2009) to maintain textural integrity of sensitive materials. The foils were collected to intersect two coccoidal organic microfossils ca. 4 mm apart in sample WWB-17-5 and analyzed by STXM mapping for the chemical composition of the organic material. The foils were mounted on a copper half grid sample holder using a platinum strap. STXM mapping of carbon was performed at the I08-SXM beamline at the Diamond Light Source (UK).

Near edge X-ray absorption fine structure (NEXAFS) spectra were collected at the carbon K-edge from 275 to 320 eV on two FIB foils taken from a double polished thin section mounted on a glass holder with sodium silicate to avoid contamination by epoxy resin. On the first foil an area of 5x5 µm, and on the second an area of 6x6 µm was raster-scanned with the transmitted x-rays detected by a photo diode at a fixed energy. The spot size was 66 nm and a dwell time of 10 ms per energy step per pixel was used. Energy steps were set to 0.15 eV steps in the region of interest (283 – 300 eV) and to 0.5 eV in pre- (275 – 283 eV) and post- (300 – 320 eV) regions. Received signals were converted to optical density using incident signal ($I_0$) measurements from an adjacent, empty region of the image above the carbon K-edge (284.5 eV). All data was processed with MANTiS (Lerotic et al., 2014) first by principal component analysis and subsequently by cluster analysis to visualize potential chemical zoning of carbon species within the mapped areas. Mantis was also used to normalize the carbon K-edge spectra and subtract dark current. In both maps the NEXAFS spectra at the C K-edge were deconvoluted using the software Fityk, following the procedure described in Bonneville et al. (2020) and references therein. After background subtraction using a linear regression line over the range of 278 to 282 eV, the spectra were normalized to the area between 280 and 291.5 eV. Gaussian functions

were applied with a constant FWHM of 0.8 eV at fixed energy peak-positions (Centroid of the Gaussian) that are representative for specific functional carbon groups (Supplementary Table 1). Two indexes were extracted from the spectra, the aromaticity index (AI) that describes the contribution of aromatic and olefinic carbons and the unsaturated index (UI) that describes the contribution of unsaturated bonds between carbon and OH groups and carbon and heteroatoms like oxygen, nitrogen (Bernard et al., 2012; Alleon et al., 2017). AI is defined as sum of the areas (*A*) of the Gaussian functions between 284 eV and 285.4 eV (AI = *A*284 + *A*284.4 + *A*284.9 + *A*285.4). UI is defined as the sum of the areas (*A*) of the Gaussian functions between 285.8 eV and 286.6 eV normalized by AI (UI = [*A*285.4 + *A*286.2 + *A*286.6]/AI). These parameters are semi-quantitative with an uncertainty of ±10 % that is inherited from the normalization procedure.

### 4.3. TEM-EDX

FIB sections were inspected after STXM analysis using a FE-TEM (FEI Tecnai G2 FEG) equipped with an Oxford 80 $mm^2$ energy-dispersive SDD X-ray detector and a Gatan UltraScan 2k CCD camera at the Institute for Geosciences, University of Jena, Germany. Bright-field (BF) imaging and selected area electron diffraction were performed in conventional TEM mode. EDX analysis was operated in scanning TEM (STEM) mode in companion with high-angle annular dark-field (HAADF) imaging. Furthermore, low angle annular dark-field (LAADF) at long camera length STEM mode was used to image the diffraction contrast of the entire FIB foils at low magnification. TEM analysis was performed to check for photodeposition of organic matter after STXM and to characterize the textural relations between organic material and mineral matrix of the analyzed materials.

## 5. Results

### 5.1. Mineralogy and petrology

Petrographic microscopy shows that the analyzed samples are predominantly composed of chert and dolomite with accessory pyrite and iron oxide phases. Chert forms the majority of the sampled

material, although samples contain subordinate dolomite as discrete laminae and fracture filling material as indicated by the distribution of the elements that form these minerals (Supplementary Figures 4 and 5). Pyrite is present as euhedral or subhedral grains <100 µm in size within the chert matrix, and iron oxides are primarily associated with dolomite laminations as thin films along laminae and crystal boundaries. Fracture-filling secondary dolomite is free of iron-oxide phases. Detrital material is sparse, with only a few ca. 200 µm large well-rounded quartz-grains. Occasionally, the presence of mm-scale angular chert clasts with a similar fabric to the surrounding chert matrix supports previous observation of syndepositional silicification and penecontemporaneous reworking. Samples record both laminated or nodular chert, with a variety of organic microfossils primarily within the chert phase.

Sample WWB-17-10 consists of mm-thick interlaminations of chert and dolomite. Chert laminae contain abundant filamentous sheaths of ca. 25 µm diameter (Figure 3a) attributed to *Eomicrocoleus* (Horodyski and Donaldson, 1984; Knoll et al., 2013). UOM is ubiquitous in both chert and dolomite laminations (Table 1). Two samples (NL-17-M and NL-17-N) show planar to wavy mm-scale laminae, with subordinate 1 mm diameter chert nodules (Table 1). Both samples contain predominantly 15 - 30 µm diameter coccoidal microfossils recognized as *Eogloeocapsa* (Golovenok and Belova, 1984; Figure 3b), and rare, fragmented 3 µm diameter filamentous sheaths (Figure 3c). UOM is ubiquitous within chert and dolomite in both samples. Finally, sample 17-5 preserves a network of <2 mm nodules interspersed within dolomite matrix (Table 1). Microfossils are predominantly coccoidal, especially *Gloeodiniopsi* species (Schopf, 1968; Knoll and Golubic, 1979) that vary from 10 µm to 40 µm in diameter (Figure 3d). Filamentous microfossils are rare and often poorly preserved (Figure 3e). UOM is ubiquitous in both chert and dolomite phases but the majority is accumulated in secondary pore spaces between nodules (Figure 3f).

The most apparent difference between laminated and nodular chert fabrics is the porosity. Laminated chert is typically dense and preserves only micrometer scale pore-spaces; nodular chert in contrast,

contains pore-spaces as large as 3 mm in diameter. Despite these differences, all samples show a similar range of diagenetic fabrics, with alternating dominance of specific features between samples. In all samples, both dolomite and chert are microcrystalline, with crystal sizes < 50 µm (Figure 4a, b). Chert often preserves a microfabric that consists of chalcedony spherules (Dunham and Kah, 2018; Figure 4c). Nodular chert preserves numerous pseudomorphs after dolomite (Figure 4d). Samples containing nodular chert also record pore spaces between nodules that can be as large as the surrounding nodules. This void space is commonly filled by UOM and can contain discrete chert spherules that might represent late-stage silica growth in void space (Figs 3e and 4e, f). Chert spherules are ca. 20 µm in diameter and can coalesce to form nodules up to 1 mm in diameter (Figure 4e). These nodules preserve UOM and dolomite pseudomorphs (Figure 4f) but do not show preservation of discrete microfossils or contain spherules with coatings of organic material. Laminated chert does not contain chert spherules.

In contrast, laminated chert contains evidence for primary void space (up to 5 mm diameter) that has been filled with dolomite, chalcedony and mega-quartz (Figure 5a and b). Such void spaces contain botryoidal, inward growing chalcedony (Fig. 5). Void spaces commonly show zoning with an outer edge composed of fine-grained (< 50 µm), partly silicified dolomite, followed by a ca. 300 µm thick zone of chalcedony, and a central filling of mega-quartz crystals (Figure 5a and b). Chalcedony lining primary voids is often intergrown with varying amounts of UOM. Most voids show organic staining that highlights radial growth patterns of void lining chalcedony (Figure 5c), some contain substantial OM that appears as a black mass overprinting chalcedony lining (Figure 5d). Microfossils are generally not preserved in void -lining chalcedony, with the rare exception of a few voids in sample WWB-17-5 that contain filamentous microfossils that appear to protrude into the former void spaces (Figure 5c). Central void fillings of mega-quartz, or more rarely dolomite, contain no organic material.

Fractures that crosscut chert are generally thin in laminated chert, and mostly without secondary fillings; some contain secondary dolomite or UOM. Veins within nodular chert are wide and filled by

447 secondary euhedral dolomite, in places with crystals as large as 500 µm (Figure 6a and b). These larger
448 dolomite crystals grew often into interstitial space between nodules and incorporated late-stage chert
449 spherules as solid inclusions (Figure 6a and b). Some dolomite crystals that formed in contact with
450 chert nodules preserve spherical structures that preserve faint internal textures and might represent
451 coccoidal microfossils or chert spherules coated by organic carbon (Figure 6c; Supplementary Figure
452 6). Euhedral dolomite that formed as a late-stage fill within voids occurs primarily in close proximity
453 to fractures.

454 Chert also occurs as mixed-phase nodules within dolomitic regions. In these instances, dolomite shows
455 partial silicification resulting in a mixed fabric of equally small (< 50 µm) dolomite and chert crystals
456 (Figure 6d) or in full replacement of the inner zone of a nodule by radially aligned chalcedony and
457 mega-quartz resembling void fillings in chert (Figure 6e). Organic material is ubiquitous as thin films
458 between crystals and often as slightly thicker and darker films between nodules or laminae (Figure
459 6e). Secondary dolomite is easily recognizable by its larger crystal size and its brighter appearance due
460 to the lack of OM in its growth fabric (Figure 6f). Occasionally, stylolites can be observed in dolomite
461 lamination forming ca. 20 µm thick anastomosing dark traces filled by UOM (Figure 6f). No microfossils
462 are preserved in dolomite beds.

463 **5.2. Diagenetic sequence**

464 Observations highlighted in the previous section provide evidence of multiple, discrete episodes of
465 mineralization that represent fluid interaction from early through late-stage diagenesis (Figure 7).
466 Initial silicification occurred penecontemporaneous with deposition and represents both the primary
467 mineralization of microbial mats and the replacement of synsedimentary mineral phases, including
468 dolomite, gypsum, and halite (see also Kah et al., 2001; Knoll et al., 2013; Manning-Berg and Kah,
469 2017). Initial silicification is the primary phase responsible for well-preserved microbial remains.
470 Laminated chert, containing mainly filamentous microbial mats, contains evidence for primary
471 constructional voids (Figure 5a, b; Knoll et al., 2013; Manning-Berg and Kah, 2017). Voids are lined

with isopachous chalcedony that transitions, with increasing crystal size to void-filling mega-quartz, suggesting continued silica precipitation from a single fluid source. In contrast voids within nodular chert reflect creation of porosity during silicification or associated diagenetic processes. These voids are commonly filled with UOM and less frequently lined with chalcedony (Figure 5c). That signifies either in-situ organic decomposition or later migration of organic-rich fluids. Substantial incorporation of UOM into void-lining chalcedony (Figure 5d) indicates silica precipitation that post-dates the primary microfossil-bearing silica phase. Discrete, optically clear chalcedony spherules that displace UOM within these voids may be associated with this secondary silica precipitation event. Chalcedony spherules are observed as solid inclusions within euhedral, late-stage dolomite (Figure 6a, b) associated with fractures that formed during burial diagenesis. Stylolites observed in these samples also represent fluid interaction during burial diagenesis. Termination of late-stage, dolomite-filled fractures at stylolites indicates that stylolite formation is the final diagenetic stage.

### 5.3. Raman spectroscopic results

Using the 532 nm laser, we recorded 339 single point Raman spectra of organic microfossils and UOM involved in all previously described diagenetic processes. We also recorded 12 line-maps on individual microfossils and 6 area maps of small microfossil populations and individual microfossils. The Raman signal of preserved OM from the Angmaat formation is highly variable, and variation is clear even prior to peak fitting by a visual comparison of Raman spectra (Figure 8). Two distinct spectral shapes (S1 and S4) can be recognized, with multiple recorded spectra of each shape. A similarly large number of spectra have intermediate shapes that indicate transitional states between the two end-members. These intermediate states have been roughly categorized into two groups S2 and S3 (Figure 8). The two most identifiable differences in the spectral shapes are a change in the intensity ratio of the 1350 $cm^{-1}$ (D1) and the 1600 $cm^{-1}$ (D2/G) spectral region, and a substantial change of the width of the 1600 $cm^{-1}$ spectral region (Figure 8). Notably spectral shape S4 was only recorded from coccoidal microfossils of sample WWB-17-5, whereas S1, S2 and S3 spectral shapes were measured in all samples, although one specific shape tended to dominate within individual samples.

i. 532 nm laser-based results

The Raman spectra of OM show large variations of extracted values and ratios. Several of these parameters were obtained before any peak fitting procedure was applied, and could be used to decide on the exact peak fitting strategy. The intensity ratio I-1600/I-1350 or varies between 1.19 and 1.89 while the intensity ratio I-1540/I-1600 or varies from 0.14 to 0.59. The FWHM-D2 ranges from 41.8 $cm^{-1}$ to 79.4 $cm^{-1}$ (Table 3). High I-1600/I-1350 ratios coincide with low FWHM-D2 (Figure 9a) and low I-1540/I-1600 ratios with the best correlation appearing between the FWHM-D2 and the I-1540/I-1600 ratio (Supplementary Figure 7). Values of the intensity ratio I-1600/I-1350 above 1.5 indicate that a 4-peak fitting procedure needs to be used to calculate paleo-temperatures (Kouketsu et al., 2014). Spectra with ratios below 1.5 show FWHM-D2 values above 60 $cm^{-1}$ that also indicate low maturity that requires the use of the same 4-peak fitting procedure.

Using the 4-peak fitting procedure (G) of Kouketsu et al. (2014), the FWHM of D1 ranges from 101.63 to 138 $cm^{-1}$, and the FWHM of D2 from 36.41 to 79.9 $cm^{-1}$. Temperatures calculated using the FWHM-D1 span between ca. 180°C to 260°C (Table 3, Figure 9b).

Using the 5-peak fitting procedure of Delarue et al. (2016), the $R1_{(5p)}$ ratio (Table 2) ranges from 1.06 to 2.03; the FWHM of D1 ranges from 110.9 $cm^{-1}$ to 148.7 $cm^{-1}$ and the FWHM of G ranges from 32.9 $cm^{-1}$ to 126.35 $cm^{-1}$ (Table 3). High $R1_{(5p)}$ ratios coincide with high FWHM-D1 and FWHM-G values. The correlation of the $R1_{(5p)}$ ratios with the FWHM-G values is better pronounced than its correlation to the FWHM-D1 values (Figure 9c, d).

Using the 7-peak fitting procedure, the $R1_{(7p)}$ ratio ranges from 0.53 to 1.05, the $R3_{(7p)}$ ratio (Table 2) ranges from 0.14 to 0.59; and the FWHM-D1 and FWHM-D2 range from 80.5 $cm^{-1}$ to 122.5 $cm^{-1}$ and from 32.0 $cm^{-1}$ to 67.5 $cm^{-1}$, respectively (Table 3). The position of the G-peak obtained in the 7-peak fitting procedure is also highly variable and occurs between 1551.2 $cm^{-1}$ to 1578.5 $cm^{-1}$ (Table 3). High $R1_{(7p)}$ ratios coincide with high FWHM-D1 and high FWHM-D2 values (Figure 9e, f); and low $R3_{(7p)}$ ratios

coincide with low FWHM-D2 values (Figure 9g) and higher wavenumbers of the G-peak position (Supplementary Figure 8).

ii. 633 nm laser-based results

Using the 633 nm laser, 171 single point spectra of both, discrete microfossils and UOM, were recorded on sample WWB-17-5 to calculate H:C ratios and estimate the maturity of organic microfossils. Spectra are assigned to the same categories as for the 532 nm Raman-spectra (Tables 3 and 4). Higher H:C ratios correspond to less mature OM while lower H:C ratios correspond to more mature OM. H:C ratios calculated by using D5/(G+D2) intensity-ratios are slightly higher (0.32-0.41) than H:C ratios calculated by using (D4+D5)/(G+D2) intensity-ratios (0.28-0.38). The highest H:C ratios are calculated for UOM (Table 4; Figure 10), and the lowest ratios are calculated for coccoidal microfossils that show the spectral shape S4 of 532 nm spectra (Table 4; Figure 10). Standard deviations show large differences in their values between the defined types of OM. Coccoidal microfossils have been subdivided according to the shape of the recorded spectra (S1 and S4) and show SD between 0.036 and 0.025. A subdivision of organic matter populations by host mineral (coccoids in chert or SOS in dolomite) results in SD as high as 0.054 (Table 4; Supplementary Table 2). The intensity ratio D1/(G+D2) reaches from 0.72 to 1 and the FWHM-D1 from 81.18 to 92.3 $cm^{-1}$ (Table 4). High D1/(G+D2) ratios coincides with high values of the FWHM-D1 (Figure 10c).

iii. Variations in OM between and within samples

In order to better understand the observed variation of the Raman spectra of OM we sorted spectra by sample, by their general taxonomy (filaments vs. coccoids), and by diagenetic context (i.e., their association with mineral phases) and, for sample WWB-17-5, by spectral shape (Table 3). Considering the full set of samples, the variation between Raman spectra of OM is substantial. Individually however, each sample shows a smaller range of variation amongst discrete types of OM (Table 3; Figure 9 and 10). Variation between spectral measurements within discrete types of OM is mostly negligible with exception of OM within sample WWB-17-5, which shows significant overlaps within

547 specific types of OM. Most apparent are the listed differences in maturity of OM between coccoidal
548 microfossils (Table 3). Raman spectroscopic line-maps from individual microfossils however, do not
549 show intra-target variation (Figure 11a – h).

550 Sample WWB-17-10 contains both filamentous microfossils (filaments) and unrecognizable organic
551 matter embedded in chert (UOM-chert). Extracted Raman parameters from these two types of OM
552 show similar values except for intensity ratios I-1600/I-1350, $R1_{(5p)}$ and $R1_{(7p)}$ (Table 3). The calculated
553 maximum thermal alteration of these two types of OM is similar with T(D1) = 255 and 242°C (Table 3;
554 Figure 9b).

555 Sample NL-17-M contains coccoidal microfossils (coccoids), free unrecognizable organic matter
556 (UOM), UOM embedded in secondary chalcedony (UOM-chc) and in chert spherules (UOM-sph).
557 Variation among the Raman proxies of different types of OM in this sample are substantial with
558 particularly large variation of the FWHM-D1 and -D2 parameters that were extracted from the 4-peak
559 fit. Variation between UOM and UOM-sph occur at µm-scale where spherules formed within UOM
560 filled pore spaces, wherein OM trapped as inclusions within spherules shows a different Raman signal
561 than OM surrounding the spherules (Figure 11i, j). However, OM inclusions within chert spherules are
562 small and rarely observed. The calculated maximum thermal alteration T(D1) varies between ca.
563 180°C for UOM and ca. 230°C for coccoidal microfossils (Table. 3; Figure 9). The lowest calculated
564 temperatures of the whole set of samples are from sample Nl-17-M.

565 Sample NL-17-N contains ubiquitous UOM, coccoidal microfossils (coccoids) and filamentous
566 microfossils (filaments) all preserved in chert. Variation between the Raman proxies of all types of OM
567 are generally low (Table 3). The calculated maximum thermal alteration T(D1) varies between 207°C
568 for filamentous microfossils and 224°C for UOM-chert (Table. 3; Figure 9).

569 Sample WWB-17-5 contains free UOM, mostly occurring as black masses in pore spaces (Figure 3f, 4e
570 and 5c), coccoidal microfossils embedded in chert (cod-chert), spherical organic structures (SOS)
571 embedded within secondary vein-filling dolomite (cod-dol), and filamentous microfossils embedded

572 in chert and chalcedony (filaments). Filaments embedded in chert and chalcedony were not treated
573 separately due to their rarity in this sample (Table 3). The 4 types of OM described here display roughly
574 two different degrees of alteration with filamentous microfossils and UOM both showing low maturity
575 while coccoidal microfossils and SOS in dolomite can display both alteration states high and low
576 mature. The calculated maximum thermal alteration T(D1) of filamentous microfossils and UOM is
577 approximately 230°C, just slightly lower than that of coccoidal microfossils in chert and SOS in
578 dolomite with a temperature of ca. 250°C (Table 3; Figure 9b).

579 Coccoidal microfossils in Sample WWB-17-5 can also be divided according to the basic spectral shape
580 (S1 and S4; Figure 10). Such division results in calculated differences in maturity that are larger than
581 the variation observed across all other samples (Table 3; Figures 9). Coccoidal microfossils with the
582 spectral shape S1 show similar Raman proxies and maximum thermal overprint (T(D1) ~230°C) as UOM
583 and filamentous microfossils. Coccoidal microfossils with the spectral shape S4 show Raman proxies
584 that correspond to the highest calculated maximum thermal overprint of the whole set of samples
585 (T(D1) ~260°C). The observed variation in spectral shape, and subsequently in extracted Raman-
586 proxies can occur within a spatial distance of only a few µm and between OM of the same and of
587 different types (Figure 12).

588 **5.4. STXM results**

589 Two coccoidal microfossils from a double polished thin section of sample WWB-17-5 were selected
590 for STXM analysis based on their contrasting Raman signals and their taxonomic and taphonomic
591 appearance. The two microfossils are approximately 4 mm apart (Figure 13a), both spherical with a
592 diameter of ca. 40 µm, and appear uniformly dark in light microscopy (Figure 13b and c). The uniformly
593 dark appearance does not allow for the identification of internal cellular structures but ensures that
594 the amount of OM within the produced FIB cuts was maximized. The identification of these two
595 structures as microfossils and not as structures such as carbon coated chert spherules is based on: (1)
596 Their size of ca. 40 µm diameter is conform with the size of individuals of *Gloeodiniopsis sp.* while

chert spherules are ca. 20 µm in diameter. (2): The chosen microfossils are imbedded in chert nodules. Chert nodules do not contain chert spherules with the exception of nodules that are entirely composed of chert spherules. However, nodules composed of chert spherules do not preserve organic microfossils. (3): The chosen coccoidal microfossils resemble individuals identified as *Gloeodiniopsis sp.* and microfossil-A is part of a small colony of this species while microfossil-B is situated next to a neighboring individual of *Gloeodiniopsis sp.* that shows internal cellular structures (Supplementary Figure 9). Within this sample, one microfossil records the Raman spectral shape S1 (microfossil-A) and the other records the Raman spectral shape S4 (microfossil-B; Figure 13d). Raman analyses at 633 nm implies a large difference in their H:C ratios (Figure 13d, e).

NEXAFS spectra of the two mapped areas show significant differences, specifically of the intensity of the aromatic spectral range (284 – 285.4 eV) relative to that of ketones and phenols (286.2 – 287.1). The intensity of the NEXAFS spectral region representative for aromatic groups is lower in microfossil-A than in microfossil-B (Figure 14; Supplementary Figure 10). The aromaticity index (AI) of microfossil-A is 0.136, the unsaturated index (UI) is 0.955 (Supplementary Figure 10). Microfossil B shows an AI of 0.252 and an UI of 0.699 (Supplementary Figure 10). Cluster analysis indicates that the mapped area of microfossil-A shows limited chemical zoning (Figure 14a). The majority of the mapped area shows approximately equal intensities of the spectral range of aromatic groups and the spectral range of ketones and phenols with the occurrence of some micro- to nano-inclusions that show a weak signal in the aromatic range (Figure 14). In turn cluster analysis of the mapped area of microfossil-B indicates a homogeneous composition of OM that is most apparent by the similarity of the resulting spectra and the undefined edges of the different cluster (Figure 14a).

### 5.5. TEM-EDX results

EDX mapping and HAADF imaging was performed equivalent to the area mapped by STXM in microfossil-A (Figure 15a). The FIB-foil of microfossil-B experienced physical damage after STXM analysis and prior to TEM analysis and the area mapped by STXM was lost. Consequently, TEM analysis

was performed on the remaining part of the foil adjacent to the area mapped by STXM (Figure 15b). The position of the FIB-foil in relation to the probed microfossil indicates that the foil is fully composed of microfossiliferous material (Figure 13c). Both FIB-foils are composed of a homogeneous micro- to nano-crystalline matrix with crystal sizes of ca. <200 nm and low porosity. Obtained diffraction patterns and EDX mapping show that the mineral matrix is composed of polycrystalline quartz (Si+O) with minor, homogeneously distributed portions of carbon (C) that form most likely thin films on quartz surfaces and at pore walls (Figure 15 c, d and Supplementary Figure 11). Additionally, the FIB-foils show sporadic coverage by < 100 nm large salt crystals (bright dots in HAADF image of Figure 15d), most likely a result of the preparation with sodium silicate that included repeated transfers of the samples to different sample holders by dissolving the mounting agent in distilled water.

## 6. Data interpretation

Several deconvolution protocols with changing numbers of peaks (up to 6) have been developed to allow for reproducible interpretations of Raman spectra of highly disordered OM (Sadezky et al., 2005; Schopf et al., 2005; Guedes et al., 2010; Lahfid et al., 2010; Kouketsu et al., 2014; Delarue et al., 2016; Ferralis et al., 2016). This requires adaptable fitting procedures to characterize the degree of alteration or maturity of OM and to visualize differences in maturation of OM in geological samples relative to each other.

### 6.1. Maturity estimation based on 4-peak fitting

Of the three fitting procedures we used for spectra acquired with a 532 nm laser, the 4-peak fitting of Kouketsu et al. (2014) is the best-known method to estimate the maximum thermal alteration of generally immature OM (i.e. temperatures of alteration between 150 – 400°C). A first evaluation of the Raman proxies I-1600/I-1350 and FWHM-D2 provides evidence to determine the exact peak-fitting procedure required for calculation of peak-temperatures (Kouketsu et al., 2014). Highly disordered OM usually shows I-1600/I-1350 ratios > 1.5 and an increase of the FWHM-D2 with increasing degree

of disorder. Such trends are recorded in both Phanerozoic rocks (Kouketsu et al., 2014) and Proterozoic organic microfossils (Baludikay et al., 2018; Pang et al., 2020). However, OM of low maturity from Proterozoic organic microfossils is also known to show I-1600/I-1350 ratios < 1.5 that coincide with FWHM-D2 values above 60 $cm^{-1}$ (Qu et al., 2015; Pang et al., 2020). Such OM still needs to be treated with the G-fitting described in Kouketsu et al., 2016.

OM from the Angmaat Formation shows a trend similar to that of low mature Proterozoic organic microfossils (Qu et al., 2015; Pang et al., 2020). All spectra that show the spectral shape S1 and S2 have I-1600/I-1350 ratios < 1.5, as low as 1.21, despite increasing FWHM-D2 values (Table 3; Figure 9a). The unusually high FWHM-D2 values but relatively normal T(D1) temperatures suggest that spectra with the peak shapes S1 and S2 display highly disordered OM, possibly of an unusual chemical composition of OM that results in a spectral maximum at 1600 $cm^{-1}$ with an unusually high relative width and low relative intensity. However, although the temperatures obtained with the T(D1) geothermometer appear relatively normal with ca. 260°C - 180°C, deviation from expected trends (Figure 9a) does not permit for an exact estimate of the thermal alteration of the OM of the lowest maturity.

### 6.2. Maturity estimation based on 5-peak fitting

An even more apparent deviation from expected alteration paths appears when using the 5-peak fitting procedure of Delarue et al. (2015). This procedure allows visualization of the OM maturation pathway (carbonization or graphitization) by plotting the intensity ratio $R1_{(5p)}$ against FWHM-D1 (Delarue et al., 2016). With an increasing degree of carbonization, the FWHM-D1 decreases while the $R1_{(5p)}$ ratio increases. When carbonization shifts to graphitization, the values of FWHM-D1 are approximately < 40 $cm^{-1}$ and the $R1_{(5p)}$ ratio starts to decrease again (Rouzaud et al., 2015; Delarue et al., 2016). Disordered OM that experienced lower degrees of carbonization typically shows low $R1_{(5p)}$ ratios (<1) and high FWHM-D1 values (>100 $cm^{-1}$). OM from the Angmaat Formation shows FWHM-D1 values >110 $cm^{-1}$, as expected, but also shows unusually high $R1_{(5p)}$ ratios > 1.21 even up to 2.03 (Figure

672 9c). Only Raman spectra with a peak shape S4 provide data that correspond to the expected
673 carbonization path (Figure 9c). An estimate of the degree of carbonization can also be made using the
674 FWHM-G instead of the FWHM-D1 where the FWHM-G decreases while the $R1_{(5p)}$ ratio increases with
675 increasing degree of carbonization (Delarue et al., 2016). OM from the Angmaat Formation however,
676 shows a trend, oblique to that expected, where the $R1_{(5p)}$ ratios decrease with decreasing FWHM-G
677 values (Figure 9d). Deviation of the extracted Raman proxies from previously predicted maturation
678 pathways does not allow for a consistent estimate of the maturity of OM from the Angmaat
679 Formation.

680 **6.3. Maturity estimates based on 633 nm results**

681 Organic microfossils of the Angmaat formation show estimated H:C ratios between 0.41 and 0.29
682 (Figure 10; Table 4) as typical for OM that experienced lower carbonization equivalent to that in the
683 zone of gas formation (Vendenbroucke and Largeau 2007). The intensity ratio D1/(G+D2) and the
684 FWHM-D1 extracted from these spectra are also similar to those of collotelinite of coal from the Penn
685 State Coal Bank (Figure 10c; Guedes et al., 2010) indicative of highly disordered OM with low maturity.

686 **6.4. Raman and STXM**

687 Overall, Raman spectroscopic methods show that spectra of OM from Angmaat Formation chert are
688 consistent with highly disordered OM of low maturity that is highly variable between samples and
689 within samples. The highest maturity is detected in coccoidal microfossils from sample WWB-17-5,
690 which appear to have undergone moderate carbonization with a maximum thermal alteration of ca.
691 260°C. The lowest mature OM occurs in UOM of sample NL-17-M, which likely experienced a
692 maximum thermal overprint of ca. 180°C. However, the OM in this sample and OM of similarly low
693 maturity from other samples deviates from established measures of alteration (Figure 9a-d). Standard
694 analysis of Raman spectra does not explain the maturation processes or chemical differences that
695 caused these variations. STXM mapping and subsequent cluster-analysis reveal distinct differences in
696 chemical composition of organic microfossils that record the S1 and S4 end member shapes of Raman

spectra. Specifically, we find that NEXAFS spectra of organic microfossils of low maturity (Raman shape S1) within Angmaat chert show lower amounts of aromatic groups in relation to phenols and ketones whereas NEXAFS spectra of more highly mature organic microfossils (Raman shape S4) that are more consistent with established maturation pathways defined by Raman spectra show higher amounts of aromatic groups in relation to phenols and ketones (Figure 14).

### 6.5. Effect of chemical variation on Raman spectra

The observed differences in the ratio of aromatic groups relative to ketones and phenols could potentially explain the differences in the Raman spectra. Raman active vibrations associated with stretching and shear modes of aromatic groups cause an intense Raman response around 1600 $cm^{-1}$ (Mapelli et al., 1999; Mayo et al., 2003). Most phenolic compounds have a less intense Raman response at ca. 1600 $cm^{-1}$. However, the intensity of the Raman response in this spectral area varies strongly between different phenolic compounds independent of their bonding to single or polycyclic aromatic groups (Pompeu et al., 2018). Raman active vibrations of ketones show an extremely weak Raman response at 1600 $cm^{-1}$ and a strong signal in the area between ca. 1560 and 1580 $cm^{-1}$ (Forrest et al., 1976). Relatively low intensities and high widths of the 1600 $cm^{-1}$ maximum of Raman spectra of low mature OM accompanied by high intensities of the D3 area (ca. 1540 $cm^{-1}$) as observed here would therefore potentially reflect a decrease of aromatic groups in a mixture of organic compounds. STXM-NEXAFS spectral results indicate that the described Raman-spectral properties are linked to a relatively low amount of aromatics while the relative amount of ketones and phenols is high (Figure 14a, b). This implies that the spectral properties of the Raman spectral maximum of OM at ca. 1600 $cm^{-1}$ in relation to the spectral area around 1540 $cm^{-1}$ can be used to determine the degree of aromaticity. However, since phenolic and ketonic compounds can also be coupled to aromatic groups and the UI index describes the contribution of unsaturated bonds between carbon and OH groups or heteroatoms (Bernard et al., 2012; Alleon et al., 2017) the described Raman-spectral variation could

721 also indicate differences in the H:C, O:C or N:C ratios similar to the relation shown between H:C ratios
722 and the intensity of the pre-1350 $cm^{-1}$ area of Raman spectra of low mature OM (Ferralis et al., 2016).

723 In all used peak fitting procedures, the FWHM-D2 shows a better linear correlation to the
724 corresponding intensity ratio R1 than the FWHM-D1 and a single-peak solution for the 1600 $cm^{-1}$
725 maximum achieves a better correlation than a 2-peak solution (Figure 9). Such spectral differences are
726 also apparent in the 7-peak procedure (Figure 9e-f) where the FWHM-D2 of the D2-peak shows a
727 strong linear correlation with the R3 ratio (Figure 9g), the position of the G-peak or even the I-1540/I-
728 1600 ratio (Supplementary Figure 8b, c). Here the FWHM-D2 is clearly used as general measure for
729 the width of this spectral area while R3 and the position of the G-peak both constrains the changing
730 left-sided asymmetry of the 1600 $cm^{-1}$ spectral area (Figure 8) and allows for a precise estimate of a
731 possible maturation path based on the degree of this asymmetry vs. the width of D2 (Figure 9g). The
732 appearance of the same linear correlation with the use of the I-1540/I-1600 ratio indicates that this
733 relation is truly originated from the obtained spectra and not an artefact of the used peak-fitting
734 procedures. Although this study includes only two valid STXM-NEXAFS measures and does therefore
735 not allow for a direct correlation between the displayed Raman parameters and the NEXAFS-based AI
736 and UI it appears reasonable that the Raman parameters of the D2- and D3-peaks can potentially be
737 used as measure for aromaticity and the contribution of unsaturated bonds between carbon and OH
738 groups or heteroatoms in highly disordered OM.

739

740 ## 7. Discussion

741 Our results show large variations of the Raman signal of OM both between samples and within
742 samples, between organic microfossils of different taphonomic grades, between microfossils of
743 different taxonomy and between microfossils of the same taxonomy (Table 3). These variations are
744 reflected in the degree of maturation (Figure 9), in calculated H:C ratios (Figure 10) and in the chemical
745 composition of organic microfossils (Figures 14 and 15). Our observations imply that preserved OM,

and specifically OM associated with preserved microfossils in sedimentary rocks do not necessarily become homogenized during early diagenesis. However, despite the observed chemical differences between discrete microfossils it is not clear what mechanism underlies these differences. The observed deviation from the traditional carbonization path could be caused by a number of processes including, but not limited to: (1) the structural ordering of OM along the surfaces of authigenic mineral phases (2) potential differences in organic precursor materials (e.g. prokaryotic vs. eukaryotic); (3) or chemical ordering of OM caused by localized fluid flow and preferential migration of soluble organic components.

### 7.1. Physical-structural ordering

The maturity of organic material in rocks can vary on the micro- and nano-scale due to alignment around authigenic minerals such as quartz and chlorite (Bustin et al., 1995; van Zuilen et al., 2012; Qu et al., 2020). However, such ordering is typically linked to intense hydrothermal circulation and to temperatures more consistent with greenschist or higher metamorphism (Bustin et al., 1995; Qu et al., 2020). Black chert of the Angmaat Formation shows no direct evidence for hydrothermal circulation or metamorphic overprint. Most organic microfossils and a large portion of UOM are imbedded in chert that is characterized as penecontemporaneous with deposition or of early diagenetic origin. Still, some UOM and organic microfossils occur in direct contact with or are found imbedded within later diagenetic phases such as chert spherules (Figures 3f and 4e, f, 11i, j), chalcedony void fillings (Figure 5) and dolomite fracture fills (Figures 7a-c). This is particularly true for sample WWB-17-5, which is the sample with the largest variation of the Raman signal (Table 3). In this sample, however, the overall maturity of coccoidal microfossils imbedded in early diagenetic chert and of spherical organic structures embedded in burial diagenetic dolomite as well as the detected variation between individual neighboring organic microfossils and structures in each of these minerals is similar (Figures 9, 10 and 12), which argues against a significant influence by the formation of secondary minerals. The same is true for filamentous microfossils in sample WWB-17-5 that are either

imbedded in early diagenetic chert (Figure 3e) or in later stage chalcedony (Figure 5c), which show no difference in their Raman signal. In turn, in both samples with significant sample-scale variation (NL-17-M and WWB-17-5), organic microfossils and UOM imbedded in the mineral matrix show mostly a higher maturity than free UOM in pore space, thereby indicating that early diagenetic mineralization may have influenced the maturity pathway of OM. This is most apparent but rarely observed on a small scale in sample NL-17-M where free UOM shows lower maturity than that of inclusions of UOM in neighboring later diagenetic chert spherules (Figure 11i, j). This observation implies that the actual preservation of OM in a mineral matrix may affect the maturation pathway similarly as to what has been demonstrated experimentally (Li et al., 2014). We expect that such a process, however, only accounts for a minor portion of the observed differences in maturity because of the rarity and the small size of the observed inclusions of OM in the spherules.

### 7.2. Organic precursors

Variations of the Raman signal of OM caused by different organic precursor materials are generally only detectable in low mature (lower carbonization) OM (Vendenbroucke and Largeau 2007; Igisu et al., 2009; Qu et al., 2015 and 2018; Bonneville et al., 2020; Pang et al., 2020). Interpretations are primarily limited to the very basic subdivision of OM derived from the three domains of life, and need to be backed up by other analytical methods (Igisu et al., 2009; Qu et al., 2015 and 2018; Bonneville et al., 2020). The taxonomy of organic microfossils in the Angmaat Formation appears to be diverse, with multiple filamentous and coccoidal form taxa (Figures 3, 8, 11, 12 and 13). These are described in detail in Knoll et al. (2013) and are interpreted as cyanobacteria, although a variety of small often poorly preserved coccoidal microfossils could also include heterotrophic bacteria (Knoll et al., 2013). The only non-bacterial microfossil known from the Angmaat Formation but not observed in this study is the early red alga *Bangiomorpha pubescens* (Butterfield, 2000; Knoll et al., 2013). The strong dominance of organic microfossils with a cyanobacterial origin suggests that variations of the Raman-signal based on differences of organic precursor material as observed before (Igisu et al., 2009; Qu et

al., 2015 and 2018; Bonneville et al., 2020) should be minor and cannot be resolved with the data presented here.

Differences in the Raman-signal occur independent of taxonomic classification. The two coccoidal microfossils chosen for STXM-analysis are from the same taxonomic group, yet display a strong difference in both Raman character and their chemical composition. Differences between taxonomic groups are not found, in this study, to be large. Generally, filamentous microfossils record lower variation in maturity than that observed in coccoidal microfossils (Table 3; Figure 9). However, such taxonomic patterns of maturity do not occur across all samples, indicating that observations should not be taken as a robust trend.

### 7.3. Early diagenesis and migration of OM

Localized early diagenetic mineralization potentially triggered by metabolic reactions has been proposed to cause differences in OM-chemistry observed in weakly metamorphosed rocks (Lepot et al., 2009). The circulation of hydrothermal fluids and potential migration of soluble organic compounds in greenschist metamorphic rocks has also been proposed as possible cause for inconsistencies in the maturity of OM (Qu et al., 2020). The potential for migration of soluble compounds of low mature OM is likely enhanced by the porosity of sedimentary rocks and the higher content of soluble organic compounds in highly disordered OM compared to more mature OM in metasedimentary rocks. Generally, low porous cherts have been suggested to limit such migration; as a result, chert has been used preferentially to derive our understanding of maturation pathways for OM (Delarue et al., 2016).

Apparent correlation between the homogeneity of the Raman signal on a sample scale and the overall diagenetic history recorded in the sample suggest that chert is not immune to effects of diagenetic fluid flow and potential migration of organic compounds. The Raman character of OM in laminated chert, that records relatively low porosity (WWB-17-10 and NL-17-N), is largely homogeneous, while the Raman character of OM in nodular chert, which shows wide fractures and pore spaces occupied

821 by free UOM, is highly variable (WWB-17-5 and NL-17-M; Figure 9; Table 1, 3). This indicates that the
822 overall porosity of the host rock is indeed a critical factor for the maturity of OM within these samples.
823 Low porosity samples, however, despite showing overall homogeneous Raman signatures of OM, still
824 record differences in maturity between each other (ΔT of ca. 40°C), indicating that porosity, although
825 most likely the cause of intra-sample variation, may not be the only factor in determination of Raman
826 signals.

827 In highly porous samples, free UOM entrapped within pore spaces is the least mature type of OM
828 (Table 3) and other types of OM, such as organic microfossils or UOM imbedded in a mineral matrix,
829 that are in close proximity to large masses of free UOM show mostly a lower maturity than their more
830 distant counterparts. This suggests that OM of low maturity could have migrated into the pore spaces
831 of nodular chert from rocks that experienced a lower diagenetic overprint. This cannot explain,
832 however, the low maturity of organic microfossils that clearly occur in their original positions (e.g.
833 Figure 13b). In an alternate scenario, exposure of UOM to fluids percolating through the pore spaces
834 could have prevented dehydration of OM which substantially contributes to the carbonization
835 pathway (Vendenbroucke and Largeau 2007; Buseck and Beyssac, 2014). Organic microfossils
836 preserved within chert nodules or spherical organic structures (SOS) preserved in secondary dolomite
837 crystals could be similarly influenced by fluid circulation through micro- and nano- pores. The lower
838 AI and higher UI of the STXM-analyzed low-mature coccoidal microfossil (Figures 14 and
839 Supplementary Figure 10) could be a result of the presence of pore fluids circulating through a
840 neighboring micro-fracture (Figure 12b). Regardless of this mechanism, presumably synsedimentary
841 silicification allowed for excellent chemical preservation of OM and the low permeability of the
842 preserved chert units and pristine preservation of microbial mat structures suggest that OM is still
843 locally derived.

844

845 **8. Conclusion**

Organic microfossils and unrecognizable organic material from black cherts of the Angmaat Formation show large variation in Raman spectra resulting in large variation in estimated maturity and calculated H:C ratios between different samples and between organic microfossils and UOM of the same sample. STXM-mapping of two coccoidal microfossils of the same taxonomy and similar taphonomy but with significantly different Raman spectra shows large differences in the chemical composition of the preserved OM that can be attributed to varying ratios of aromatic compounds relative to ketones and phenols. Physical structural ordering and differences in organic precursor material have only minor influence on the observed differences in Raman spectroscopy and STXM. The most likely explanation for the observed variation is chemical ordering or the lack thereof caused by the suppression of carbonization-induced dehydration due to the presence of diagenetic pore fluids. This is strongly influenced by the porosity of the analyzed chert where higher porosity correlates directly to a higher variability of the maturity and underlying chemical composition of OM. The large differences in the involvement of aromatic groups and carbon bound heteroatoms and OH groups shown by STXM-mapping indicate that the diversion of Raman-parameters from the known carbonization pathway of OM is most likely representative of an alternative maturation pathway triggered by these chemical variations. This alternative pathway is most evident by the strongly changing intensity ratio R3 and an equally strong change of the width of the spectral maximum at ca. 1600 $cm^{-1}$. Our study shows that diverse populations of microfossils in ancient sedimentary rocks show significant small-scale variation in their chemical maturity that are potentially caused by multiple processes. Raman spectroscopy, is a valuable, fast and non-destructive method to identify the least altered specimens in diverse populations of ancient organic microfossils that however, needs to be applied in-situ on petrographically well characterized samples to fully understand the meaning of individual measurements. This is especially important for organic microfossils that show such exceptional preservation as in the chert of the Angmaat Formation where the low chemical and structural alteration potentially allowed for the preservation of the observed variation.

872 **References**


873 Alleon, J., Bernard, S., Le Guillou, C., Daval, D., Skouri-Panet, F., Kuga, M., Robert, F., 2017. Organic molecular
874 heterogeneities can withstand diagenesis. Sci. Rep. 7, 1508. https://doi.org/10.1038/s41598-017-
875 01612-8

876 Aoya, M., Kouketsu, Y., Endo, S., Shimizu, H., Mizukami, T., Nakamura, D., Wallis, S., 2010. Extending the
877 application of Raman carbonaceous-material geothermometer using data from contact metamorphic
878 rocks. J. metamorphic Geol., 28, 895-914. https://doi.org/10.1111/j.1525-1314.2010.00896.x

879 Arne, D.C., Duddy, I.R., Sangster, D.F., 1990. Thermochronological constraints on ore formation at the Gays
880 River Pb-Zn deposit, Nova Scotia, Canada, from apatite fission track analysis. Canadian Journal of
881 Earth Sciences, 27, 1013-1022.

882 Baludikay, B.K., Francois, C., Sforna, M.C., Beghin, J., Cornet, Y., Storme, J.-Y., Fagel, N., Fontaine, F., Littke, R.,
883 Baudet, D., Delvaux, D., Javaux, E.J., 2018. Raman microspectroscopy, bitumen reflectance and illite
884 crystallinity scale: comparison of different geothermometry methods on fossiliferous Proterozoic
885 sedimentary basins (DR Congo, Mauritania and Australia). International Journal of Coal Geology, 191,
886 80-94. https://doi.org/10.1016/j.coal.2018.03.007

887 Bartley, J.K., 1996. Actualistic Taphonomy of Cyanobacteria: Implications for the Precambrian Fossil Record.
888 PALAIOS, 11, 571–586.

889 Bernard, S., Benzerara, K., Beyssac, O., Menguy, N., Guyot, F., Brown Jr., G.E., Goffe, B., 2007. Preservation of
890 plant fossils in high-pressure metamorphic rocks. Earth and Planetary Science Letters 262 (1–2), 257–
891 272.

892 Bernard S., Benzerara K., Beyssac O., Brown, Jr., G. E., Grauvogel-Stamm L. and Duringer P. 2009.
893 Ultrastructural and chemical study of modern and fossil sporoderms by Scanning Transmission X-ray
894 Microscopy (STXM). Review of Palaeobotany and Palynology 156, 248–261.

895 Bernard, S., Horsfield, B., Schulz, H-M., Wirth, R., Schreiber, A., Sherwood, N., 2012. Geochemical evolution of
896 organic-rich shales with increasing maturity: A STXM and TEM study of the Posidonia Shale (Lower
897 Toarcian, northern Germany). Marine and Petroleum Geology, 31, 70-89.

898 Beyssac, O., Goffe, B., Chopin, C., Rouzaud, J.N., 2002. Raman spectra of carbonaceous material from
899 metasediments: a new geothermometer. J. metamorphic Geol., 20, 859–871.
900 https://doi.org/10.1046/j.1525-1314.2002.00408.x

901 Beyssac, O., Simoes, M., Avouac, J-P., Farley, K., Chen, Y-G., Chan, Y-C., Goffe, B., 2007. Late Cenozoic
902 metamorphic evolution and exhumation of Taiwan. Tectonics, 26, TC6001.
903 https://doi.org/10.1029/2006TC002064

904 Bonneville, S., Delpomdor, F., Preat, A., Chevaller, C., Araki, T., Kazemlan, M., Steel, A., Schreiber, A., Wirth, R.,
905 Benning, L.G., 2020. Molecular identification of fungi microfossils in Neoproterozoic shale rock.
906 Science Advances, 6, eaax7599. https://doi.org/10.1126/sciadv.aax7599

907 Bosak, T., Bush, J., Flynn, M., Liang, B., Ono, S., Petroff, A.P., Sim, M.S., 2010. Formation and stability of
908 oxygen-rich bubbles that shape photosynthetic mats: Geobiology, 8, 45–55.
909 http://doi.org/10.1111/j.1472-4669.2009.00227.x.

910 Buseck, P.R., and Beyssac, O., 2014. From organic matter to graphite: Graphitization. Elements 10, 421-426.
911 https://doi.org/10.2113/gselements.10.6.421

912 Bustin, R.M., Ross, J.V. and Rouzaud, J.N., 1995. Mechanism of graphite formation from kerogen: experimental
913 evidence. International Journal of Coal Geology, 28, 1-36. https://doi.org/10.1016/0166-
914 5162(95)00002-U

915 Butterfield, N.J., 2000. Bangiomorpha pubescens n. gen., n. sp.: Implications for the evolution of sex,
916 multicellularity and the Mesoproterozoic/Neoproterozoic radiation of eukaryotes: Paleobiology, 26,
917 386-40. https://dx.doi.org/10.1666/0094-8373(2000)026%3C0386:BPNGNS%3E2.0.CO;2

Butterfield, N.J., 2015. Early evolution of the Eukaryota. Palaeontology, 58, 5–17. https://doi.org/10.1111/pala.12139

Czaja, A.D., Beukes, N.J., and Osterhout, J.T., 2016. Sulfur-oxidizing bacteria prior to the Great Oxidation Event from the 2.52 Ga Gamohaan Formation of South Africa. Geology, 44, 983–986. doi:10.1130/G38150.1

Delarue, F., Rouzaud, J-N., Derenne, S., Bourbin, M., Westall, F., Kremer, B., Sugitani, K., Deldicque, D., Robert, F., 2016. The Raman-Derived Carbonization Continuum: A Tool to Select the Best-Preserved Molecular Structures in Archean Kerogens. Astrobiology, 16, 407-417. https://dx.doi.org/10.1089%2Fast.2015.1392

Dunham, J.J. and Kah, L.C., 2018. Crystallization of opal to length-fast chalcedony within Proterozoic microfossiliferous chert. GSA Annual Meeting, Indianapolis, Indiana, USA. https://doi.org/10.1130/abs/2018AM-322571

Edwards C.T., Pufahl P.K., Hiatt E.E., Kyser T.K. 2012. Paleoenvironmental and taphonomic controls on the occurrence of Paleoproterozoic microbial communities in the 1.88Ga Ferriman Group, Labrador Trough, Canada. Precambrian Research, 212/213, 91-106. https://doi.org/10.1016/j.precamres.2012.04.020

Ferralis, N., Matys, E.D., Knoll, A.H., Hallmann, C., Summons, R.E., 2016. Rapid, direct and non-destructive assessment of fossil organic matter via microRaman spectroscopy. Carbon, 108, 440-449. https://doi.org/10.1016/j.carbon.2016.07.039

Ferrari, A.C. and Robertson, J., 2000. Interpretation of Raman spectra of disordered and amorphous carbon. Physical Review B, 6, 14095–14107. https://doi.org/10.1103/PhysRevB.61.14095

Forrest, G., Vilcins, G, Lephardt, J.O., 1976. Structural characterization of cyclopropyl pyridyl ketones by i.r. and Raman spectroscopy. Spectrochimica Acta, 32A, 511-518.

Gibson, T.M., Shih, P.M., Cumming, V.M., Fischer, W.W., Crockford, P.W., Hodgskiss, M.S.W., Wörndle, S., Creaser, R.A., Rainbird, R.H., Skulski, T.M., Halverson, G.P., 2018. Precise age of Bangiomorpha pubescens dates the origin of eukaryotic photosynthesis. Geology, 46, 135–138. https://doi.org/10.1130/G39829.1

Golovenko, V.K., & Belova, N.YU, 1984. Riphean microbiotas in cherts of the Billyakh Group on the Anabar Uplift: Paleontogical Journal, 4, 20–30.

Guedes, A., Valentim, B., Prieto, A.C., Rodrigues, S., Noronha, F., 2010. Micro-Raman spectroscopy of collotelinite, fusinite and macrinite. International Journal of Coal Geology, 83, 415 – 422. https://doi.org/10.1016/j.coal.2010.06.002

Guo, Z., Peng, X., Czaja, A.D., Chen, S., Ta, K., 2018. Cellular taphonomy of well-preserved Gaoyuzhuang microfossils: A window into the preservation of ancient cyanobacteria. Precambrian Research, 304, 88-98. https://doi.org/10.1016/j.precamres.2017.11.007

Hahn, K.E., Turner, E.C., Babechuk, M.G., Kamber, B.S., 2015. Deep-water seep-related carbonate mounds in a Mesoproterozoic alkaline lake, Borden Basin (Nunavut, Canada). Precambrian Res., 271, 173–197.

Henry, D.G., Jarvis, I., Gillmore, G., Stephenson, M., 2019. Raman spectroscopy as a tool to determine the thermal maturity of organic matter: Application to sedimentary, metamorphic and structural geology. Earth-Science Reviews, 198, 102936. https://doi.org/10.1016/j.earscirev.2019.102936

Hnatyshin, D., Kontak, D.J., Turner, E.C., Creaser, R.A., Morden, R., Stern, R.A., 2016. Geochronologic (Re-Os) and fluid-chemical constraints on the formation of the Mesoproterozoic-hosted Nanisivik Zn-Pb deposit, Nunavut, Canada: evidence for early diagenetic, low-temperature conditions of formation; Ore Geology Reviews, 79, 189–217. https://doi.org/10.1016/j.oregeorev.2016.05.017

Hofmann, H.J., 1976. Precambrian microflora, Belcher Island, Canada: Significance and systematic: Journal of Paleontology, 50, 1040–1073.

963 Hofmann, H.J., Jackson, G.D., 1991. Shelf-Facies Microfossils from the Uluksan Group (Proterozoic Bylot
964 Supergroup), Baffin Island, Canada. J. Paleontol., 65, 361–382.

965 Horodyski, R.J., and Donaldson, J.A., 1980. Microfossils from the middle Proterozoic Dismal Lakes Group, arctic
966 Canada: Precambrian Research, 11, 125–159. https://doi.org/10.1016/0301-9268(80)90043-1

967 Igisu, M., Ueno, Y., Shimojima, M., Nakashima, S., Awramik, S.M., Ohta, H., Maruyama, S., 2009. Micro-FTIR
968 spectroscopic signatures of Bacterial lipids in Proterozoic microfossils. Precambrian Research, 173, 19-
969 26. https://doi.org/10.1016/j.precamres.2009.03.006

970 Jackson, G., Iannelli, T., 1981. Rift-related cyclic sedimentation in the Neohelikian Borden Basin, northern
971 Baffin Island. Geol. Surv. Can. Pap., 81, 269–302.

972 Javaux, E.J., Knoll, A.H., Walter, M.R., 2001. Morphological and ecological complexity in early eukaryotic
973 ecosystems. Nature 412, 66–69. https://doi.org/10.1038/35083562

974 Javaux, E.J., Lepot, K., 2018. The Paleoproterozoic fossil record: Implications for the evolution of the biosphere
975 during Earth's middle-age. Earth-Science Reviews, 176, 68-86.
976 https://doi.org/10.1016/j.earscirev.2017.10.001

977 Kah, L.C., 2000. Depositional δ18O signatures in Proterozoic dolostones: Constraints on seawater chemistry
978 and early diagenesis. SEPM (Society for Sedimentary Geology), Special Publication 67.

979 Kah, L.C., Knoll, A.H., 1996. Microbenthic distribution of Proterozoic tidal flats: Environmental and taphonomic
980 considerations. Geology, 24, 79–82.

981 Kah, L.C., Lyons, T.M., Chelsey, J.T., 2001. Geochemistry of a 1.2 Ga carbonate-evaporite succession, northern
982 Baffin and Bylot Islands: Implication for Mesoproterozoic marine evolution: Precambrian Research,
983 111, 203–234. https://doi.org/10.1016/S0301-9268(01)00161-9

984 Kah, L.C., Sherman, A.G., Narbonne, G.M., Knoll, A.H., Kaufman, A.J., 1999. δ13C stratigraphy of the
985 Proterozoic Bylot Supergroup, Baffin Island, Canada: Implications for regional lithostratigraphic
986 correlations. Can. J. Earth Sci., 36, 313–332.

987 Knoll, A. H., 2014. Paleobiological perspectives on early eukaryotic evolution. Cold Spring Harbor Perspectives
988 in Biology, 6 (1), https://doi.org/10.1101/cshperspect.a016121

989 Knoll, A.H., and Golubic, S., 1979. Anatomy and taphonomy of a Precambrian algal stromatolite: Precambrian
990 Research, 10, 115–151. https://doi.org/10.1016/0301-9268(79)90022-6

991 Knoll, A.H., Wörndle, S., Kah, L.C., 2013. Covariance of microfossil assemblages and microbialite textures across
992 an upper Mesoproterozoic carbonate platform. Palaios, 28, 453–470.
993 https://doi.org/10.2110/palo.2013.p13-005r

994 Kouketsu, Y., Mizukami, T., Mori, H., Endo, S., Aoya, M., Hara, H., Nakamura, D., and Wallis, S., 2014. A new
995 approach to develop the Raman carbonaceous material geothermometer for low-grade
996 metamorphism using peak width. Island Arc, 23, 33-50. https://doi.org/10.1111/iar.12057

997 Lahfid, A., Beyssac, O., Deville, E., Negro, F., Chopin, C. and Goffe, B., 2010. Evolution of Raman spectrum of
998 carbonaceous material in low-grade metasediments of the Glarus Alps (Switzerland). Terra Nova, 22,
999 354–360. https://doi.org/10.1111/j.1365-3121.2010.00956.x

1000 Lepot K., Benzerara K., Rividi N., Cotte M., Brown, Jr., G. E. and Philippot P. 2009. Organic matter
1001 heterogeneities in 2.72 Ga stromatolites: alteration versus preservation by sulfur incorporation.
1002 Geochimica et Cosmochimica Acta, 73(21), 6579–6599. https://doi.org/10.1016/j.gca.2009.08.014

1003 Lerotic, M., Mak, R., Wirick, S., Meirer, F., Jacobsen, C., 2014. MANTiS: a program for the analysis of X-ray
1004 spectromicroscopy data. Journal of Synchrotron Radiation, 21, 1206–1212.
1005 https://doi.org/10.1107/S1600577514013964

1006 Li, J., Bernard, S., Benzerara, K., Beyssac, O., Allard, T., Cosmidis, J., Moussou, J., 2014. Impact of
1007 biomineralization on the preservation of microorganisms during fossilization: An experimental
1008 perspective, Earth and Planetary Science Letters, 400, 113-122.

Lünsdorf, N.K., Dunkl, I., Schmidt, B.C., Rantitsch, G., von Eynatten, H., 2014a. Towards a Higher Comparability of Geothermometric Data obtained by Raman Spectroscopy of Carbonaceous Material. Part I: Evaluation of Biasing Factors. Geostandards and Geoanalytical Research, 38, 73-94. https://doi.org/10.1111/j.1751-908X.2013.12011.x

Lünsdorf, N.K., Dunkel, I., Schmidt, B.C., Rantitsch, G., von Eynatten H., 2014b. Towards a Higher Comparability of Geothermometric Data obtained by Raman Spectroscopy of Carbonaceous Material. Part 2: A Revised Geothermometer. 41, 593-612. https://doi.org/10.1111/ggr.12178

Manning-Berg, A.R., and Kah, L.C., 2017. Proterozoic microbial mats and their constraints on environments of silicification. Geobiology, 15, 469-483. https://doi.org/10.1111/gbi.12238

Manning-Berg, A.R., Wood, R.S., Williford, K.H., Czaja, A.D., Kah, L.C., 2019. The Taphonomy of Proterozoic Microbial Mats and Implications for Early Diagenetic Silicification. Geosciences, 9, 40. https://doi.org/10.3390/geosciences9010040

Mapelli, C., Castiglioni, C., Zerbi, G., and Müllen, K. 1999. Common force field for graphite and polycyclic aromatic hydrocarbons. Phys. Rev. B 60, 12710–12725.

Mayo, D.W., Miller, F.A., Hannah, R.W., 2003. Course Notes on the Interpretation of Infrared and Raman Spectra: John Wiley & Sons, Inc, pp. 567. https://doi.org/10.1002/0471690082

McNaughton, K., Smith, T.E., 1986. A fluid inclusion study of sphalerite and dolomite from the Nanisivik lead-zinc deposit, Baffin Island, Northwest Territories, Canada. Economic Geology, 81, 713–20.

Nyberg, A.V., Schopf, J.W., 1984. Microfossils in stromatolitic cherts from the upper Proterozoic Min'Yar Formation, southern Ural Mountains, USSR: Journal of Paleontology, 58, 738–772.

Pang, K., Tang, Q., Wu, C., Li, G., Chen, L., Wan, B., Yuan, X., Bodnar, R.J., Xiao, S., 2020. Raman spectroscopy and structural heterogeneity of carbonaceous material in Proterozoic organic-walled microfossils in the North China Craton. Precambrian Research, 346, 105818. https://doi.org/10.1016/j.precamres.2020.105818

Pompeu, D.R., Larondelle, Y., Rogez, H., Abbas, O., Fernandez Pierna, J.A., Baeten, V., 2018. Characterization and discrimination of phenolic compounds using Fourier transform Raman spectroscopy and chemometric tools. Biotechnol. Agron. Soc. Environ., 22, 13-28. https://doi.org/10.25518/1780-4507.16270

Qu, Y., Engdahl, A., Zhu, S., Vajda, V., McLoughlin, N., 2015. Ultrastructural Heterogeneity of Carbonaceous Material in Ancient Cherts: Investigating Biosignatures Origin and Preservation. https://doi.org/10.1089/ast.2015.1298

Qu, Y., van Zuilen, M.A., Lepland, A., 2020. Hydrothermal circulation and oil migration at the root of the heterogeneous micro-structure of carbonaceous material in the 2.0 Ga Zaonega Formation, Onega Basin, Russia. Precambrian Research, 343, 105705. https://doi.org/10.1016/j.precamres.2020.105705

Qu, Y., Zhu, S., Whitehouse, M., Engdahl, A., McLoughlin, N., 2018. Carbonaceous biosignatures of the earliest putative macroscopic multicellular eukaryotes from 1630 Ma Tuanshanzi Formation, north China. Precambrian Research, 304, 99-109. https://doi.org/10.1016/j.precamres.2017.11.004

Rahl, J.M., Anderson, K.M., Brandon, M.T., Fassoulas, C., 2005. Raman spectroscopic carbonaceous material thermometry of low-grade metamorphic rocks: Calibration and application to tectonic exhumation in Crete, Greece. Earth and Planetary Science Letters, 240, 339-354. https://doi.org/10.1016/j.epsl.2005.09.055

Romero-Sarmiento, M.F., Rouzaud, J.-N., Bernard, S., Deldicque, D., Thomas, M., Littke, R., 2014. Evolution of Barnett Shale organic carbon structure and nanostructure with increasing maturation. Org. Geochem. 71, 7–16. https://doi.org/10.1016/j.orggeochem.2014.03.008

Rouzaud, J.-N., Delicque, D., Charon, É., Pageot, J., 2015. Carbons at the heart of questions on energy and environment: A nanostructural approach. C. R. Geoscience, 347, 124-133. http://doi.org/10.1016/j.crte.2015.04.004

Sadezky, A., Muckenhuber, H., Grothe, H., Niessner, R., Pöschl, U., 2005. Raman microspectroscopy of soot and related carbonaceous materials: spectral analysis and structural information. Carbon, 43, 1731–1742.

Schopf, J.W., 1968. Microflora of the Bitter Springs Formation, late Precambrian central Australia: Journal of Paleontology, 42, 651–688.

Schopf, J.W., Kudryavtsev, A.B., Agresti, D.G., Czaja, A.D., and Wdowiak, T.J., 2005. Raman imagery: a new approach to assess the geochemical maturity and biogenicity of permineralized Precambrian fossils. Astrobiology, 5, 333–371. doi:10.1089/ast.2005.5.333

Sforna, M.C., van Zuilen, M.A., and Philippot, P. 2014. Structural characterization by Raman hyperspectral mapping of organic carbon in the 3.46 billion-year-old Apex chert, Western Australia. Geochim Cosmochim Acta, 124, 18–33. https://doi.org/10.1016/j.gca.2013.09.031

Turner, E.C., 2009. Mesoproterozoic carbonate systems in the Borden Basin, Nunavut. Can. J. Earth Sci., 46, 915–938.

Vandenbroucke, M., Largeau, C., 2007. Kerogen origin, evolution and structure. Organic Geochemistry, 38, 719-833. https://doi.org/10.1016/j.orggeochem.2007.01.001

van Zuilen, M.A., Fliegel, D., Wirth, R., Lepland, A., Qu, Y., Schreiber, A., Romashkin, A.E., Philippot, P., 2012. Mineral-templated growth of natural graphite films. Geochim. Cosmochim. Acta, 83, 252–262. https://doi.org/10.1016/j.gca.2011.12.030

Wirth, R., 2009. Focused Ion Beam (FIB) combined with SEM and TEM: Advanced analytical tools for studies of chemical composition, microstructure and crystal structure in geomaterials on a nanometer scale. Chem. Geol. 261, 217–229. https://doi.org/10.1016/j.chemgeo.2008.05.019

Wopenka, B. and Pasteris, J.D., 1993. Structural characterization of kerogens to granulite-facies graphite: applicability of Raman microprobe spectroscopy. Am Mineral, 78, 533–557.

Zhang, Y., 1981. Proterozoic stromatolitic microfloras of the Gaoyuzhuang Formation (early Sinian, Riphean), Hebei, China: Journal of Paleontology, 55, 485–506.

**Figure 1:** General geology of the Bylot Supergroup on northern Baffin Island, Canada (modified after Manning-Berg et al., 2019). **(a):** Western Baffin Island and Bylot Island (upper right). The field area in the red rectangle is shown in b. **(b):** General geology of the east/central Bordan basin on Baffin Island with the Angmaat Formation as part of the Uluksan Group (Legend to the lower left). Sampling locations are marked with red dots. WWB: west White Bay; NL: north lake.

**Figure 2:** Peak-fitting solutions for Raman spectra of organic microfossils of the Angmaat Formation. **(a):** 4-peak deconvolution (fitting G) of Raman spectra obtained with 532 nm laser after Kouketsu et al., (2016). **(b):** 5-peak deconvolution of Raman spectra obtained with 532 nm laser after Delarue et al., (2016). **(c):** 7-peak deconvolution of Raman spectra obtained with 532 nm laser. **(d):** 6-peak deconvolution of Raman spectra obtained with 633 nm laser after Ferralis et al., (2016). Note: the spectrum in d was obtained from the same spot as in a – c. Note: details of fitting solutions and residual spectra are shown in Supplementary Figure 2.

**Figure 3:** Organic microfossils and unrecognizable organic material (UOM) in Angmaat Formation chert. **(a):** Thick filamentous microfossils in laminated chert of sample WWB-17-10. **(b):** Coccoidal microfossils in laminated chert of sample NL-17-M. The image is overexposed to light to visualize the internal structures of individual microfossils. **(c):** Thin, fragmented filamentous microfossil in

laminated chert from sample NL-17-N. **(d):** Colonial coccoidal microfossils in chert from sample WWB-17-5. **(e):** Thin, poorly preserved filamentous microfossils preserved in chert from sample WWB-17-5. **(f):** UOM in pore space between chert nodules and spherules in sample WWB-17-5.

**Figure 4:** Mineral fabrics and pseudomorphs. **(a, b):** Translucent- and polarized-light image of microcrystalline-dolomite (upper left) and -chert (lower right) in sample WWB-17-5. **(c):** Polarized-light image of chert pseudomorphs after gypsum rosettes (sample WWB-17-10). **(d):** Translucent-light image of partly silicified dolomite (black arrow) and chert pseudomorphs after dolomite (white arrows) in sample WWB-17-5. **(e):** Nodule composed of chert spherules (sample WWB-17-5A). The zoning is caused by varying amounts of OM involved in the formation of the nodule. Black arrows point towards fairly well preserved coccoidal microfossils outside the nodule. The area in the dashed rectangle is shown in more detail in f. **(f):** Polarized-light image of spherules showing typical radial alignment of chalcedony.

**Figure 5:** Fillings of former void spaces. **(a, b):** Translucent- and polarized-light image ca. 5 mm large former void in the laminated area of sample NL-17-N. The filling shows zoning starting with a zone of fine crystalline dolomite at the edge followed by radially aligned chalcedony and mega-quartz in the center. **(c):** Former voids in sample WWB-17-5 filled by botryoidal chalcedony. Note the filamentous microfossils at the edges that protrude into the former void (black arrows). **(d):** Former void space filled by botryoidal chalcedony (sample NL-17-M) and a high amount of UOM that forms a dark film covering the radial growth of the chalcedony.

**Figure 6:** Diagenetic fabrics of dolomite. **(a, b):** Translucent- and polarized-light image of up to 500 µm large vein filling idiomorphic dolomite crystals (sample WWB-17-5). The dolomite fills former pore space occupied by UOM and chert spherules that are now preserved as inclusions in dolomite. **(c):** Vein filling euhedral dolomite incorporating spherical organic structures that are potential coccoidal microfossils or chert spherules coated by organic carbon (black arrows). **(d):** Polarized-light image of a partly silicified dolomite nodule. Silicification is more advanced in the center of the nodule. **(e):** Polarized-light image of a strongly silicified dolomite nodule with radially aligned chalcedony as outer zone followed by chert and micro-dolomite and mega-quartz in the center. Note the amalgamations of OM as dark thin layers between dolomite nodules. **(f):** Stylolite in dolomite layer visible as meandering thin trace of OM.

**Figure 7:** Simplified diagenetic sequence of black chert of the Angmaat Formation with emphasis to sedimentary and diagenetic phases that interact with OM.

**Figure 8:** Raman spectral shapes recorded from coccoidal organic microfossils of sample 17-5. The shown coccoidal microfossils are embedded in chert and show cellular structures or are part of a colony of organic microfossils that contains numerous individuals with cellular structures.

**Figure 9:** Raman-parameters extracted from Raman-spectra of organic microfossils and UOM obtained with 533 nm laser. **(a):** FWHM-1600 $cm^{-1}$ vs. intensity ratio R1(I-1600/I-1350). The gray arrow shows the inferred development of the two parameters with increasing maturity of OM after Kouketsu et al., (2014). The black arrow shows the approximate development of the two parameters with increasing

maturity of organic matter from the Angmaat Formation. **(b):** Maximum thermal overprint (T in °C) calculated using the FWHM-D1 extracted from 4-peak fit after Kouketsu et al., (2014). **(c and d):** Intensity ratio $R1_{(5p)}$ vs. FWHM-D1 and -D2 obtained from 5-peak fit after Delarue et al. (2016). Previously predicted carbonization and graphitization paths ([1]Rouzaud et al., 2015; [2]Delarue et al., 2016;) are given for comparison. **(e and f):** Intensity ratio $R1_{(7p)}$ vs. FWHM-D1 and -D2 obtained from 7-peak fit. Blue dashed lines show linear trends of each plot with arrows pointing towards increasing maturity. **(g):** FWHM-D2 vs. $R3_{(7p)}$ obtained from 7-peak fit. **(h):** Legend for a-g showing symbols sorted by sample, diagenetic and taxonomic context.

**Figure 10:** Raman parameters extracted from spectra recorded with 633 nm laser from sample WWB-17-5 **(a):** Intensity ratio D5/(G+D2) vs. H:C ratio. **(b):** Intensity ratio (D4+D5)/(G+D2) vs. H:C ratio. H:C ratios calculated using this intensity ratio are slightly lower than in a. **(c):** Intensity ratio D1/(G+D2) vs. FWHM-D1. Empty symbols are for comparison and show Raman parameters obtained from macerals of coals from the Penn State Coal Bank presented in Guedes et al. 2010. The cutoff at 100 $cm^{-1}$ for the FWHM-D1 is a result of the restriction of the maximum peak width to this value. **(d):** Legend for a – c.

**Figure 11:** Raman characteristics of organic microfossils and UOM. Spectral plots show multiple normalized spectra from the marked spots. Spectra may appear as one if they are similar. **(a, b):** Line-map of filamentous microfossil from sample WWB-17-10. **(c, d):** Line-map of coccoidal microfossil with preserved internal structures of sample NL-17-N. **(e, f):** Line-map of coccoidal microfossil in secondary dolomite from sample WWB-17-5. **(g, h):** Line-map of coccoidal microfossil in chert from sample WWB-17-5. **(i):** Free UOM and UOM-sph in pore-space of sample NL-17-M. Spherules can contain inclusions of OM (light blue lens) or OM can be captured between amalgamated spherules (dark blue lens). **(j):** Normalized Raman spectra of free UOM (yellow), of UOM-inclusion in spherule (light blue) and of UOM between spherules (dark blue).

**Figure 12:** Raman maps of organic microfossils from sample WWB-17-5 with higher mature OM marked in blue and lower mature OM marked in yellow. The respective spectra used to define blue and yellow areas and their parameters are shown to the right of each map. **(a):** Raman map of a filamentous and coccoidal microfossil preserved in chert. **(b):** Raman point map of coccoidal microfossils preserved in chert. **(c):** Raman map of spherical organic structures preserved in dolomite. **(d):** Raman map of coccoidal microfossils in contact to UOM preserved in chert.

**Figure 13:** Organic microfossils from sample WWB-17-5 analyzed by STXM-mapping. **(a):** Polished slide of with position of coccoidal microfossils (in b and c) ca. 4 mm apart. **(b and c):** Coccoidal microfossils chosen for STXM-mapping. The microfossil in b shows the Raman spectral shape S1 (microfossil A), the microfossil in c shows the Raman spectral shape S4 (microfossil B). Raman spots are shown as yellow and blue dots that correlate to the spectra in d and e. Lines are the positions of the FIB cuts. The dashed line in b marks the track of a thin fracture. **(d):** Raman spectra of coccoidal microfossil A obtained with 532 nm and 633 nm laser and extracted Raman parameters indicative of lower maturity. **(e):** Raman spectra of coccoidal microfossil B obtained with 532 nm and 633 nm laser and extracted Raman parameters indicative of higher maturity.

**Figure 14:** STXM maps and corresponding NEXAFS-spectra. **(a):** Position of STXM map (6X6 µm) of organic microfossil-A with Raman spectral shape S1 (Figure 13b, d) on FIB foil and cluster map indicating three areas with different composition of organic matter. **(b):** Position of STXM map (5X5 µm) of organic microfossil-B with Raman spectral shape S4 (Figure 13c, e) indicating three areas with different composition of organic matter. **(c):** NEXAFS spectrum of mapped area in (a) of microfossil-A with corresponding fitting. **(d):** NEXAFS spectrum of mapped area in (b) of microfossil-B with corresponding fitting. Fitting positions of Gaussian functions in (c) and (d) are shown in Supplementary Table 1. **(e):** NEXAFS spectra of cluster analysis of STXM map in (a). Colors correspond to the colormap in (a). **(f):** NEXAFS spectra of cluster analysis of STXM map in (b). Colors correspond to the colormap in (b).

**Figure 15:** TEM images and maps. **(a and b):** LAADF images (diffraction contrast) of the entire FIB foils. Areas mapped by TEM-EDX are outlined by white squares. Note: foil in b is damaged and turned clockwise by 90° compared to SEM image shown in figure 14b, dashed line indicates the position of the area mapped by STXM. **(c and d):** HAADF images, TEM-EDX maps of Si, O, C, and diffraction patterns of mapped areas outlined in a and b. The HAADF image in the lower center in c shows a closeup of the C-rich porous area to the left of the EDX maps. The distribution of Cl to the lower center in d correlates to the bright spots in the HAADF image and indicates the presence of halite. All diffraction spots/rings stem from polycrystalline quartz.

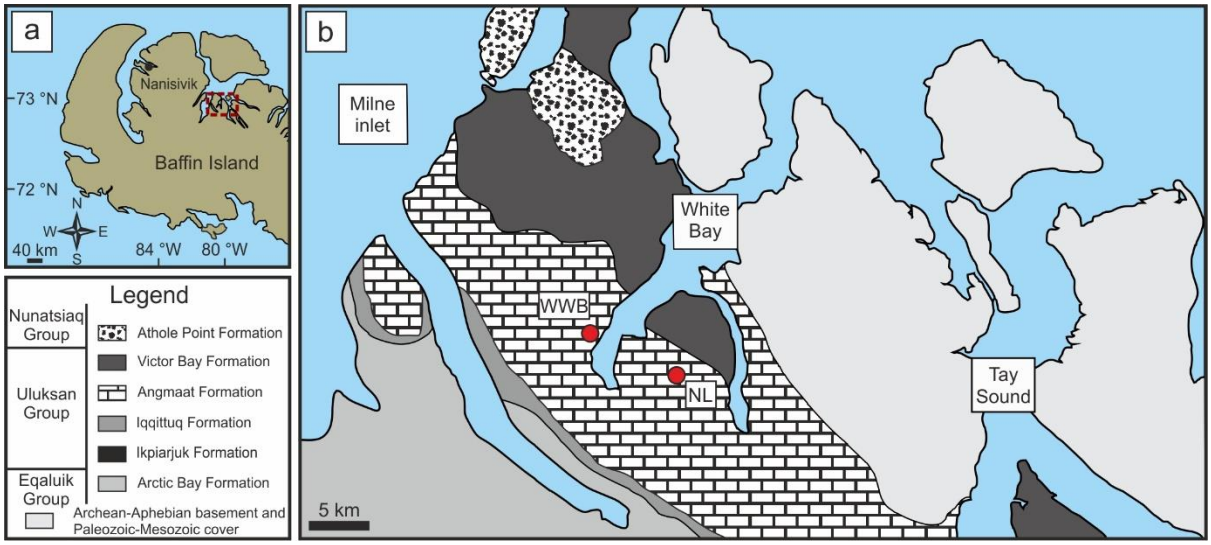
a
Nanisivik
73 °N
72 °N
Baffin Island
N
W
E
S
40 km
84 °W
80 °W
Legend
Nunatsiaq Group
Uluksan Group
Eqaluik Group
Athole Point Formation
Victor Bay Formation
Angmaat Formation
Iqqittuq Formation
Ikpiarjuk Formation
Arctic Bay Formation
Archean-Aphebian basement and Paleozoic-Mesozoic cover
b
Milne inlet
White Bay
WWB
NL
Tay Sound
5 km

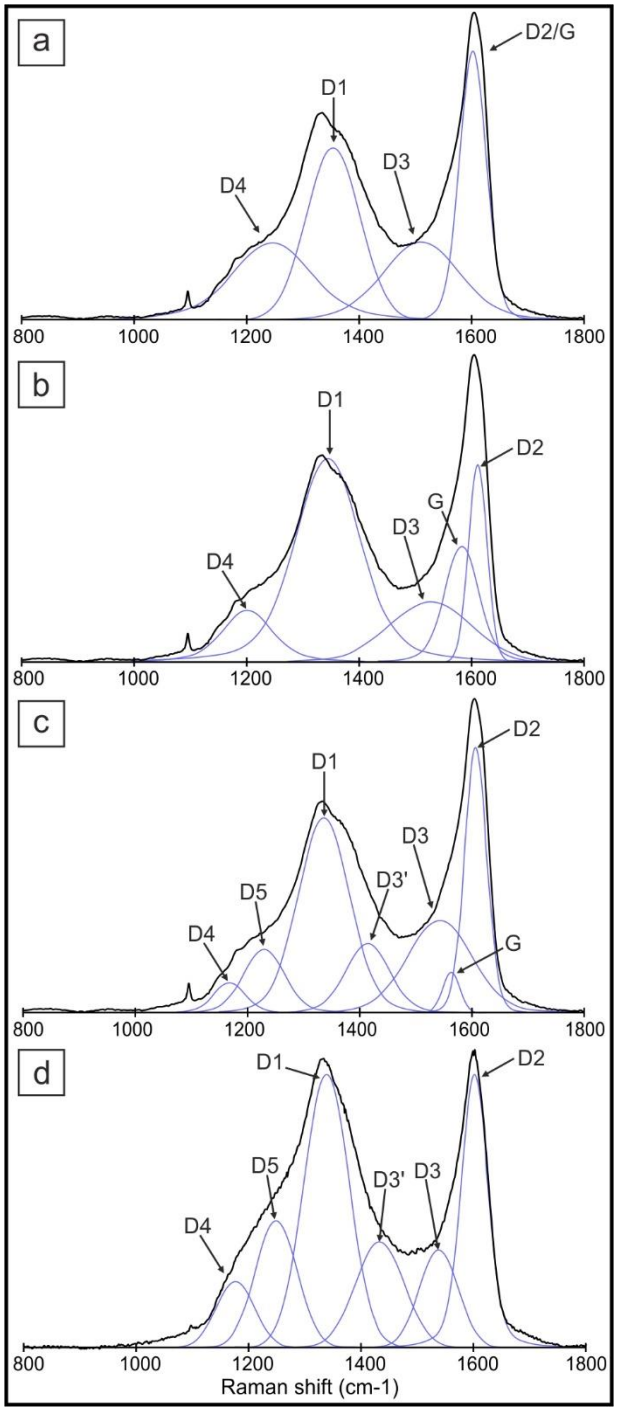
a
D2/G
D1
D3
D4
800
1000
1200
1400
1600
1800
b
D1
D2
G
D3
D4
c
D2
D1
D3
D3'
D5
D4
G
d
D1
D2
D5
D3'
D3
D4
Raman shift (cm-1)

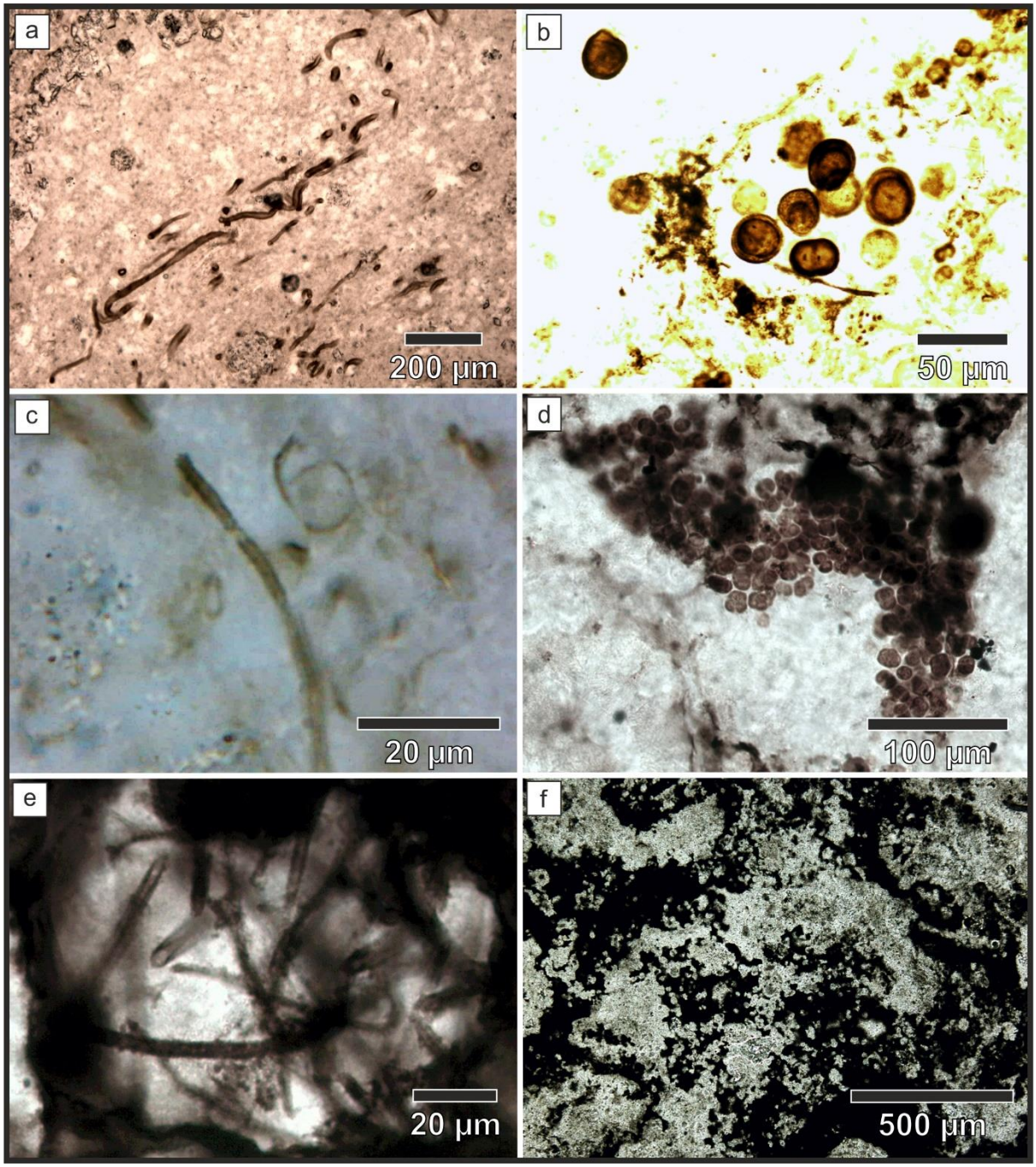
a
200 µm
b
50 µm
c
20 µm
d
100 µm
e
20 µm
f
500 µm

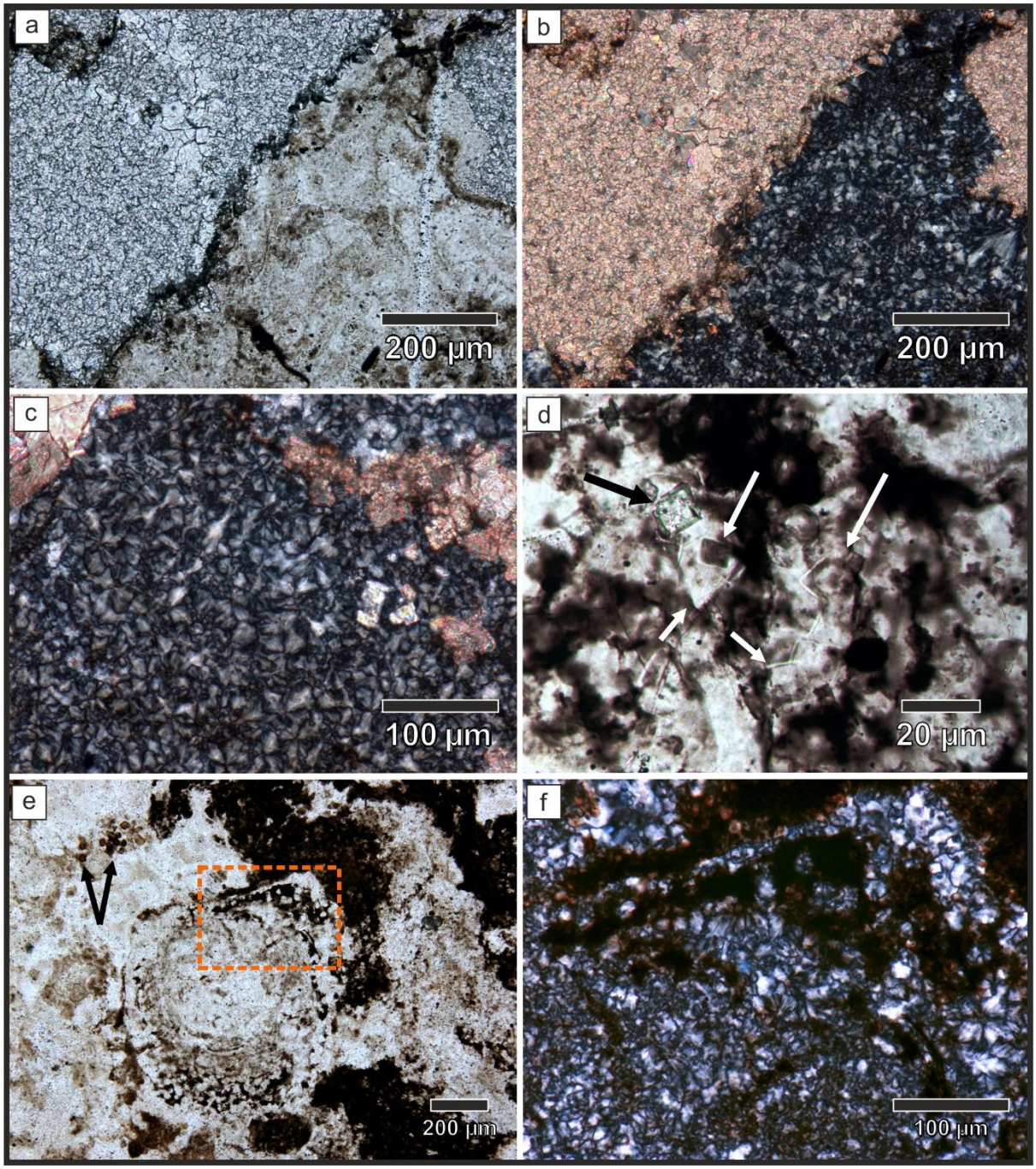
a
200 µm
b
200 µm
c
100 µm
d
20 µm
e
200 µm
f
100 µm

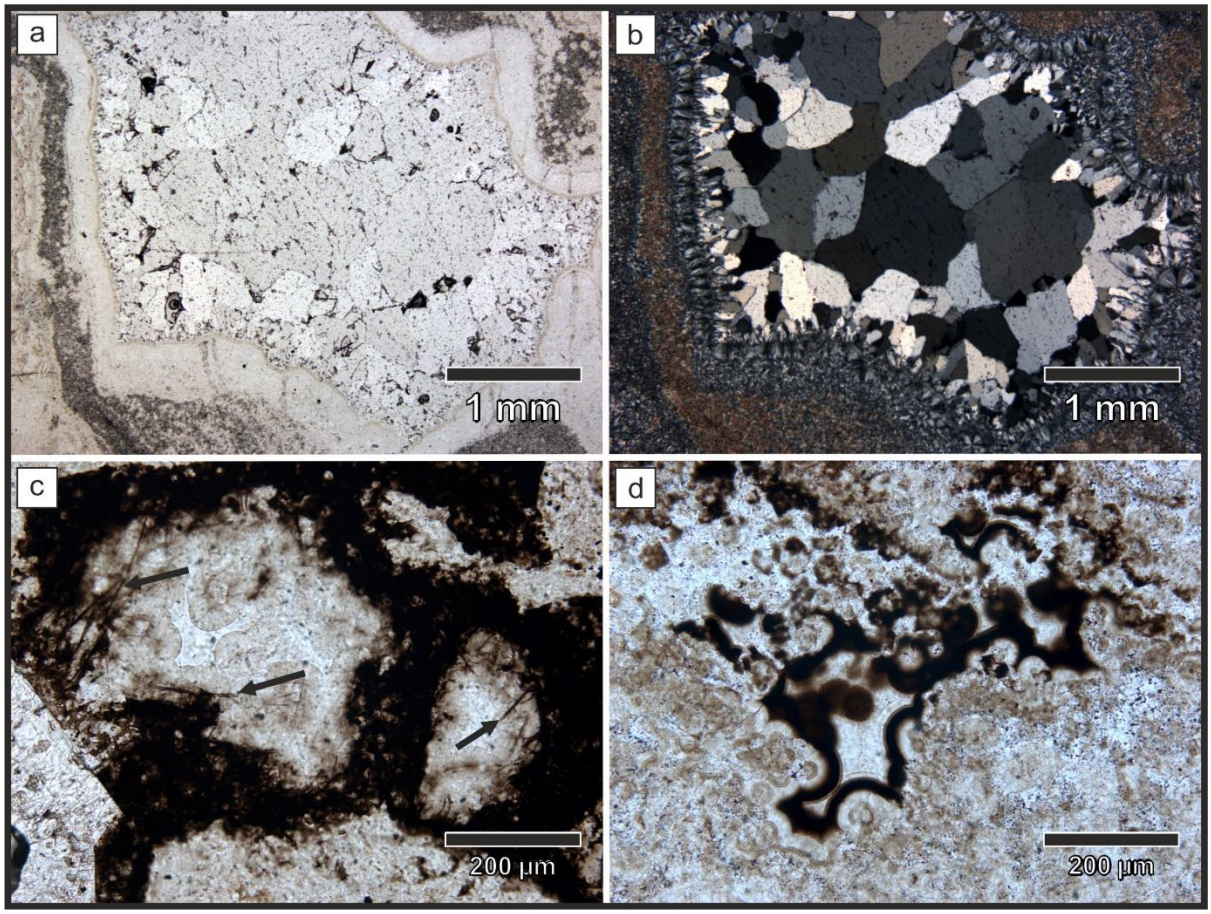
a
1 mm
b
1 mm
c
200 µm
d
200 µm

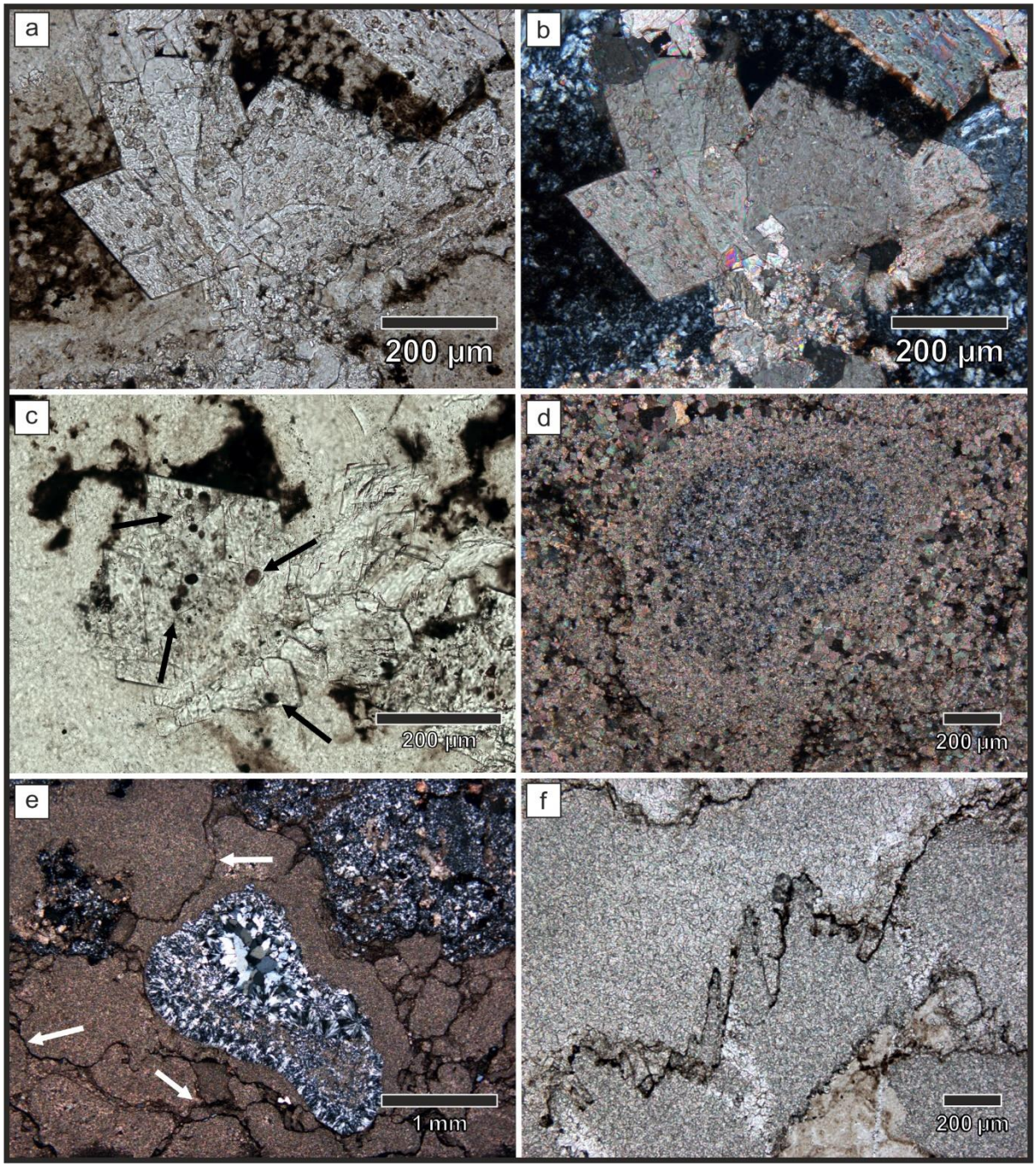
a
200 µm
b
200 µm
c
200 µm
d
200 µm
e
1 mm
f
200 µm

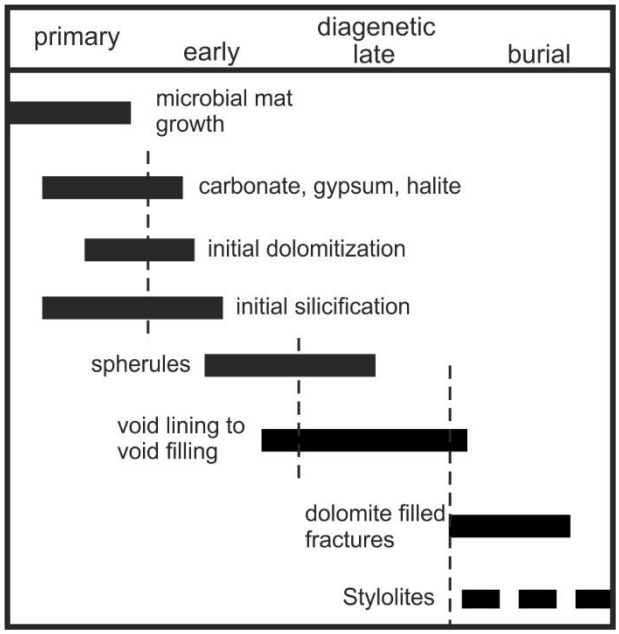
primary
early
diagenetic
late
burial
microbial mat growth
carbonate, gypsum, halite
initial dolomitization
initial silicification
spherules
void lining to void filling
dolomite filled fractures
Stylolites

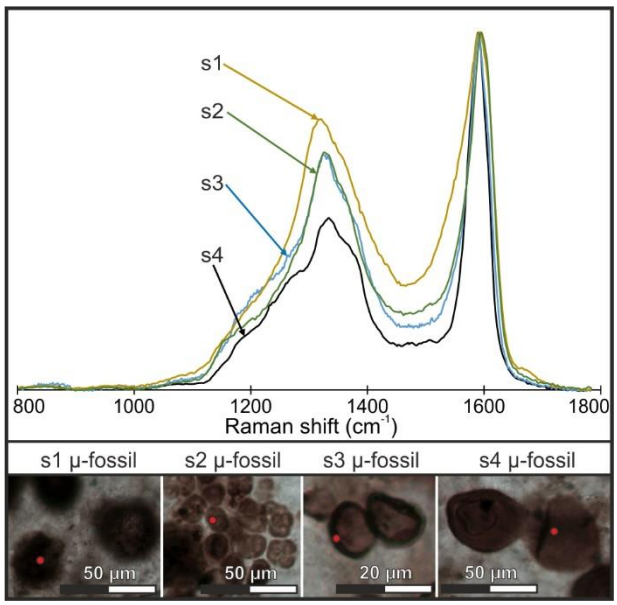
s1
s2
s3
s4
800
1000
1200
1400
1600
1800
Raman shift (cm-1)
s1 µ-fossil
s2 µ-fossil
s3 µ-fossil
s4 µ-fossil
50 µm
50 µm
20 µm
50 µm

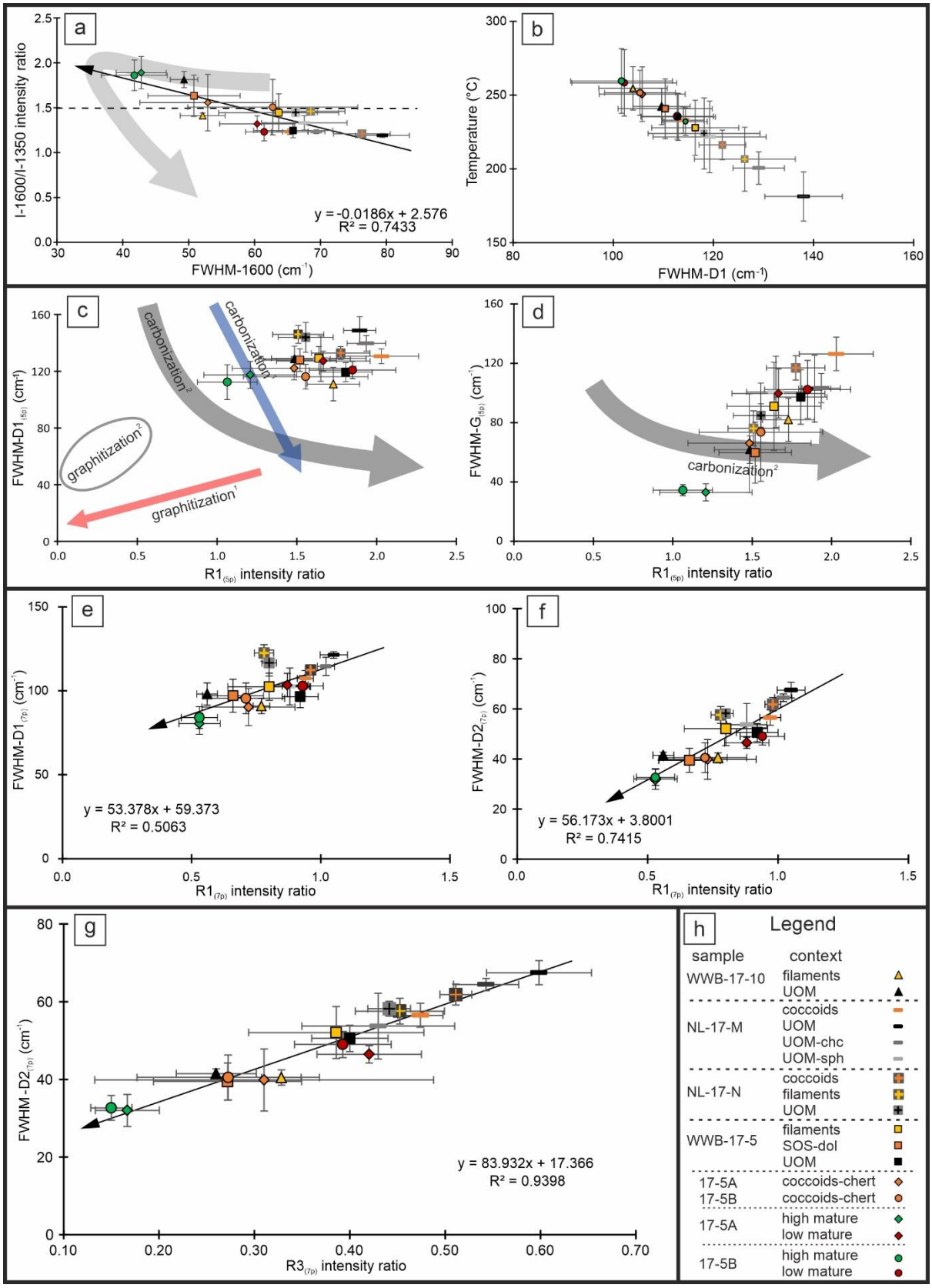
a
I-1600/I-1350 intensity ratio
FWHM-1600 (cm-1)
y = -0.0186x + 2.576
R² = 0.7433
b
Temperature (°C)
FWHM-D1 (cm-1)
c
FWHM-D1(5p) (cm-1)
R1(5p) intensity ratio
carbonization2
carbonization1
graphitization2
graphitization1
d
FWHM-G(5p) (cm-1)
R1(5p) intensity ratio
carbonization2
e
FWHM-D1(7p) (cm-1)
R1(7p) intensity ratio
y = 53.378x + 59.373
R² = 0.5063
f
FWHM-D2(7p) (cm-1)
R1(7p) intensity ratio
y = 56.173x + 3.8001
R² = 0.7415
g
FWHM -D2(7p) (cm-1)
R3(7p) intensity ratio
y = 83.932x + 17.366
R² = 0.9398
h
Legend
sample
context
WWB-17-10
filaments
UOM
NL-17-M
coccoids
UOM
UOM-chc
UOM-sph
NL-17-N
coccoids
filaments
UOM
WWB-17-5
filaments
SOS-dol
UOM
17-5A
coccoids-chert
17-5B
coccoids-chert
17-5A
high mature
low mature
17-5B
high mature
low mature

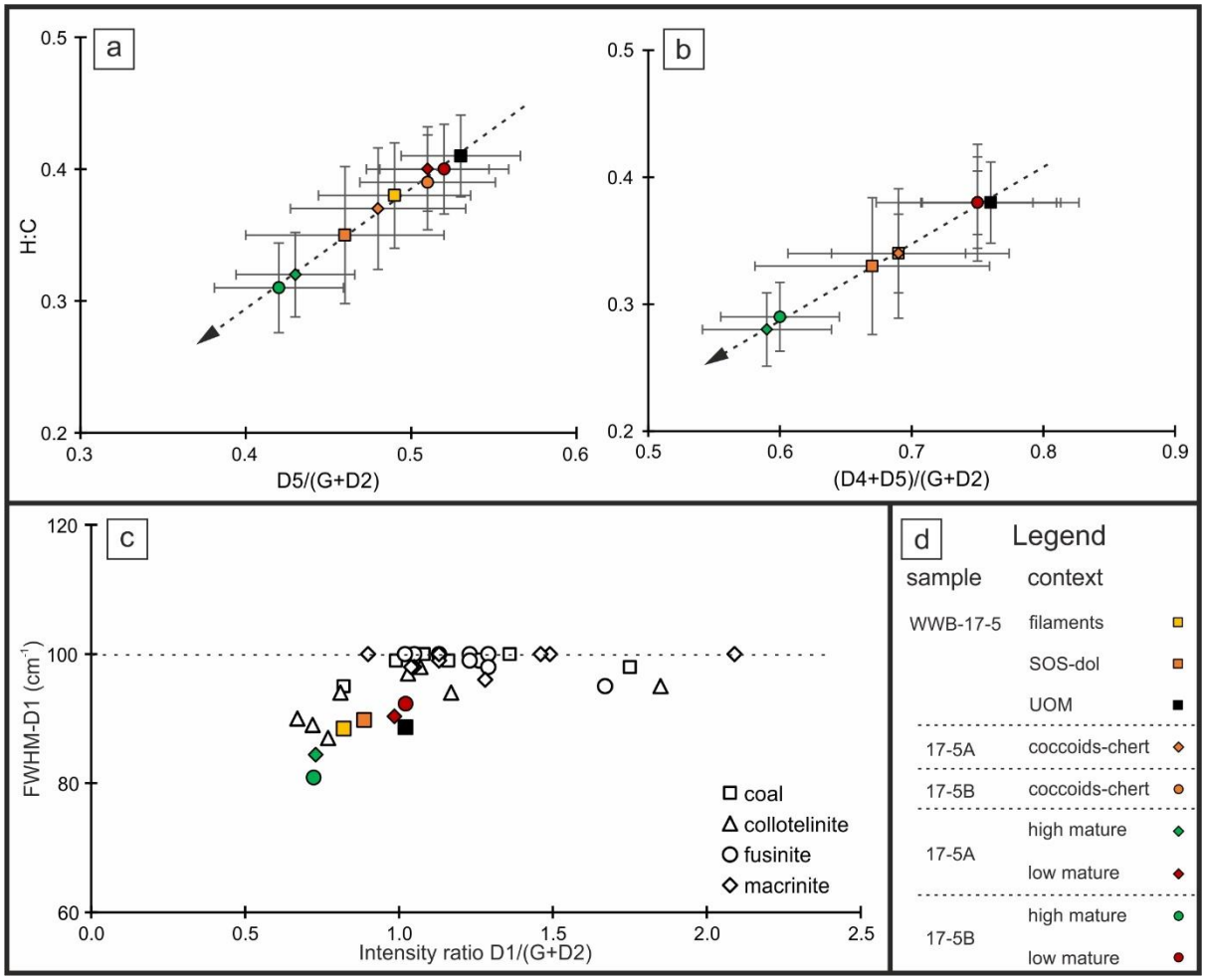
a
H:C
D5/(G+D2)
b
(D4+D5)/(G+D2)
c
FWHM-D1 (cm-1)
Intensity ratio D1/(G+D2)
coal
collotelinite
fusinite
macrinite
d
Legend
sample
context
WWB-17-5
filaments
SOS-dol
UOM
17-5A
coccoids-chert
17-5B
coccoids-chert
17-5A
high mature
low mature
17-5B
high mature
low mature

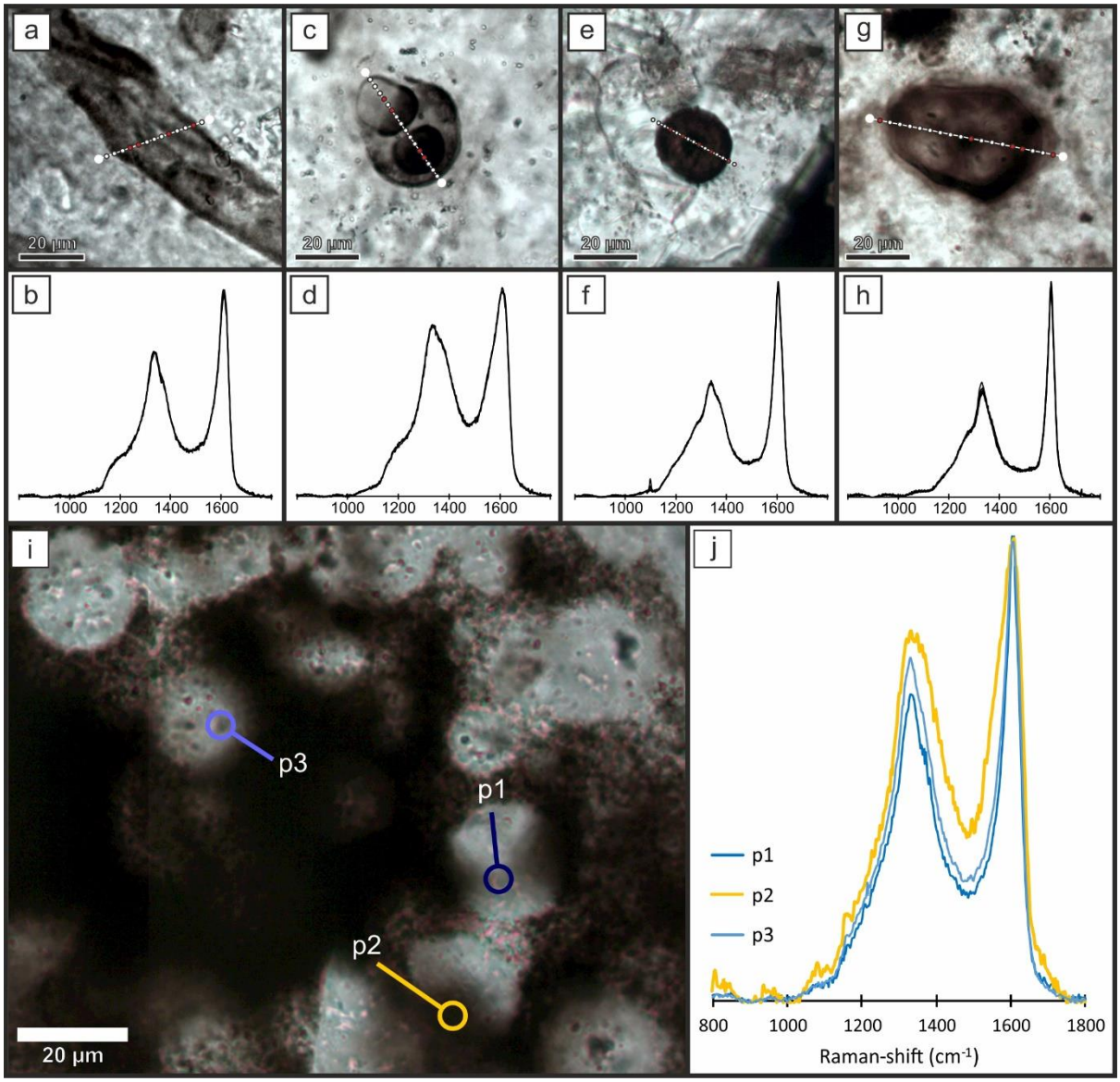
a
c
e
g
20 µm
20 µm
20 µm
20 µm
b
d
f
h
1000 1200 1400 1600
1000 1200 1400 1600
1000 1200 1400 1600
1000 1200 1400 1600
i
p3
p1
p2
20 µm
j
p1
p2
p3
800 1000 1200 1400 1600 1800
Raman-shift (cm-1)

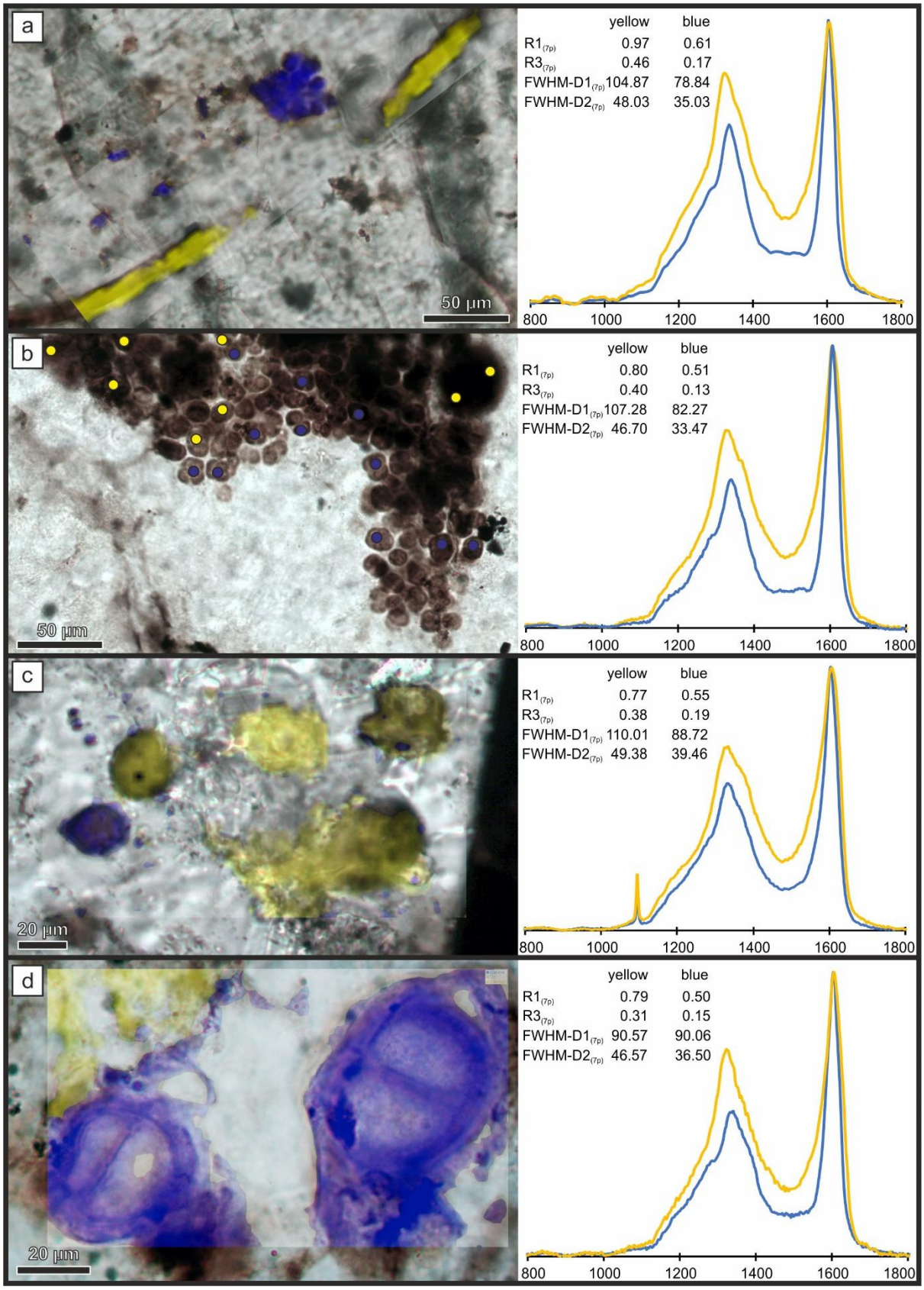
a
50 µm
yellow blue
R1(7p) 0.97 0.61
R3(7p) 0.46 0.17
FWHM-D1(7p) 104.87 78.84
FWHM-D2(7p) 48.03 35.03
800 1000 1200 1400 1600 1800
b
50 µm
yellow blue
R1(7p) 0.80 0.51
R3(7p) 0.40 0.13
FWHM-D1(7p) 107.28 82.27
FWHM-D2(7p) 46.70 33.47
800 1000 1200 1400 1600 1800
c
20 µm
yellow blue
R1(7p) 0.77 0.55
R3(7p) 0.38 0.19
FWHM-D1(7p) 110.01 88.72
FWHM-D2(7p) 49.38 39.46
800 1000 1200 1400 1600 1800
d
20 µm
yellow blue
R1(7p) 0.79 0.50
R3(7p) 0.31 0.15
FWHM-D1(7p) 90.57 90.06
FWHM-D2(7p) 46.57 36.50
800 1000 1200 1400 1600 1800

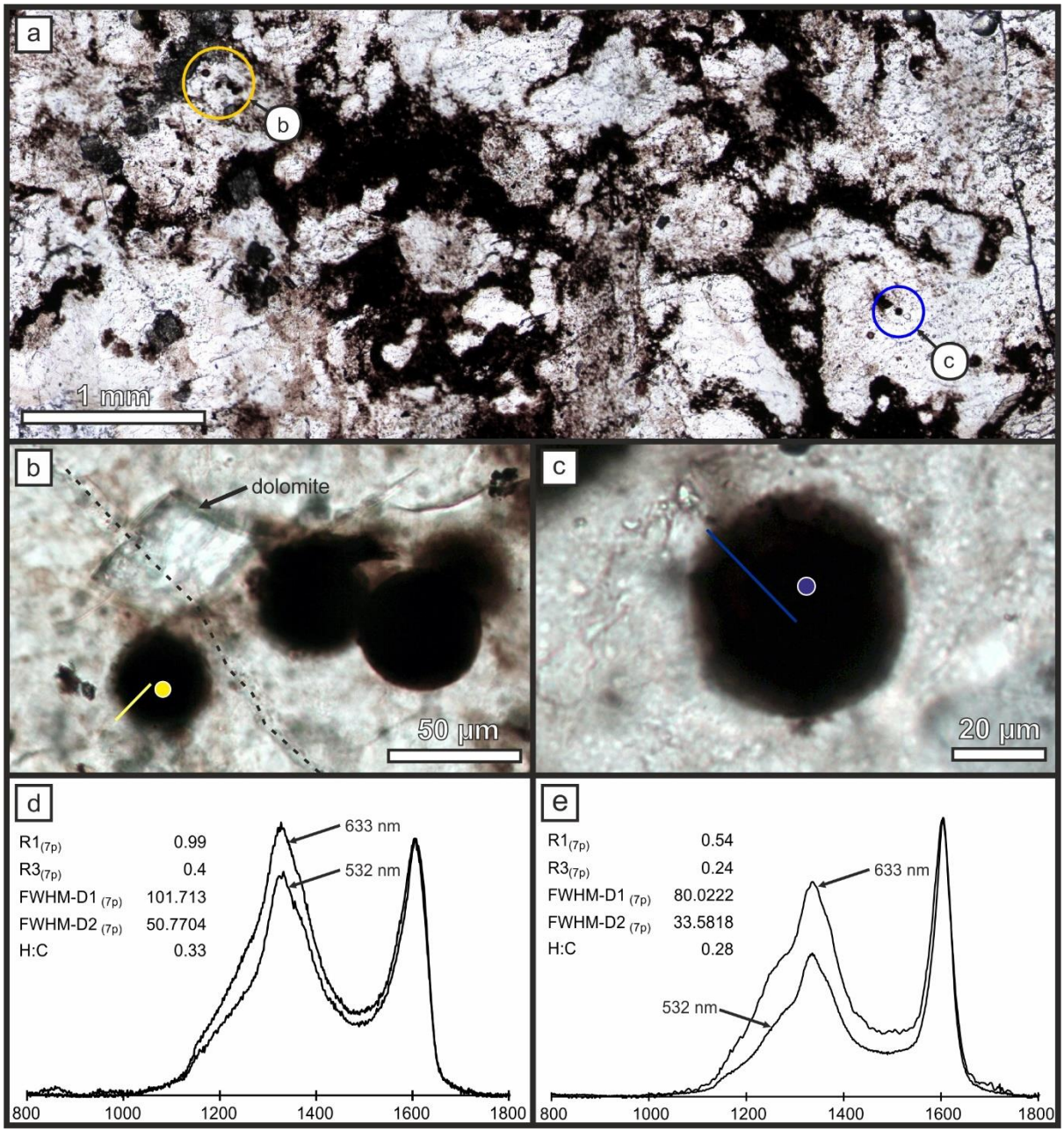
a
b
c
1 mm
b
dolomite
50 µm
c
20 µm
d
R1(7p) 0.99
R3(7p) 0.4
FWHM-D1 (7p) 101.713
FWHM-D2 (7p) 50.7704
H:C 0.33
633 nm
532 nm
800
1000
1200
1400
1600
1800
e
R1(7p) 0.54
R3(7p) 0.24
FWHM-D1 (7p) 80.0222
FWHM-D2 (7p) 33.5818
H:C 0.28
633 nm
532 nm
800
1000
1200
1400
1600
1800

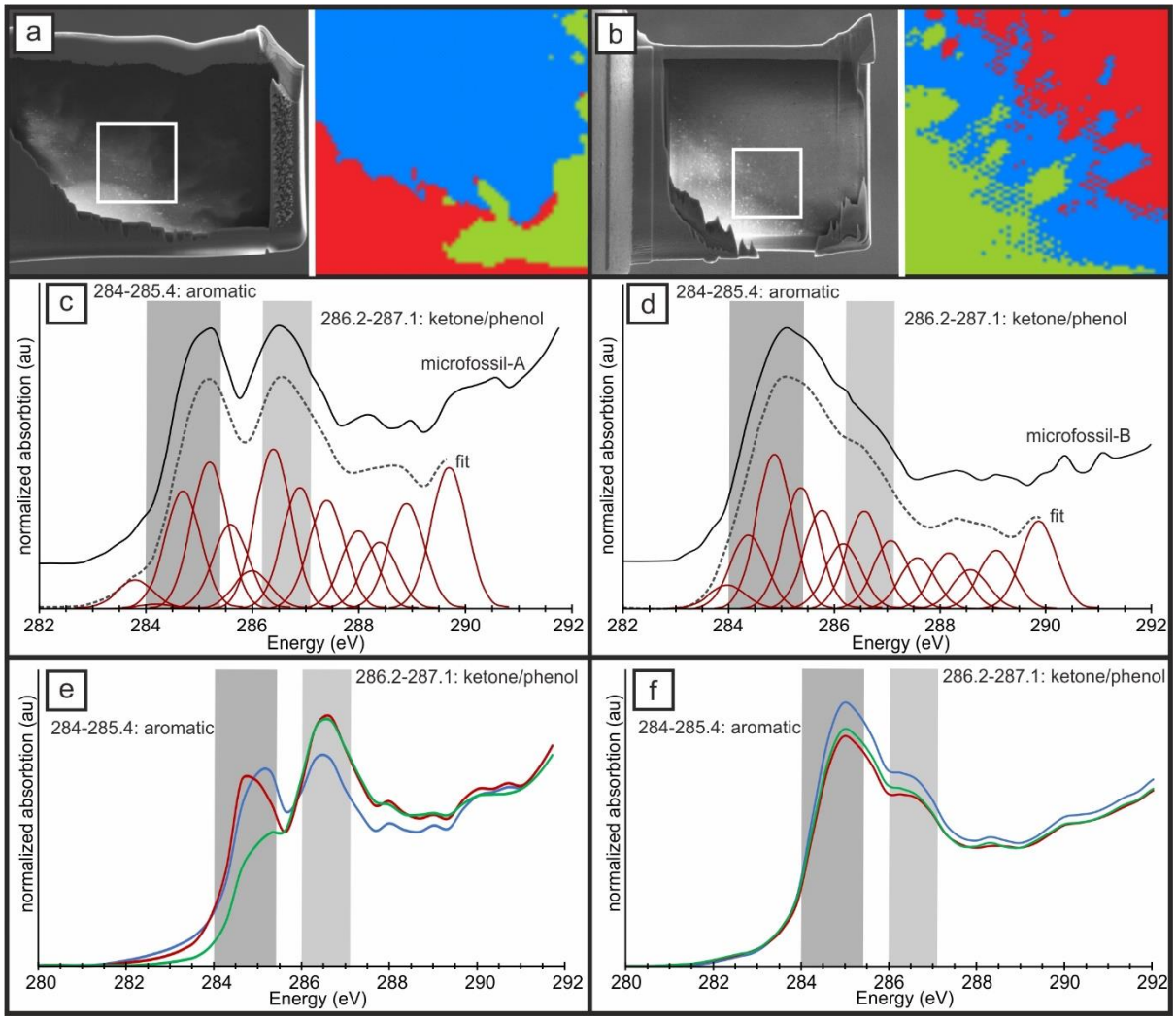
a
b
c
284-285.4: aromatic
286.2-287.1: ketone/phenol
microfossil-A
fit
normalized absorbtion (au)
282
284
286
288
290
292
Energy (eV)
d
284-285.4: aromatic
286.2-287.1: ketone/phenol
microfossil-B
fit
normalized absorbtion (au)
282
284
286
288
290
292
Energy (eV)
e
286.2-287.1: ketone/phenol
284-285.4: aromatic
normalized absorbtion (au)
280
282
284
286
288
290
292
Energy (eV)
f
286.2-287.1: ketone/phenol
284-285.4: aromatic
normalized absorbtion (au)
280
282
284
286
288
290
292
Energy (eV)

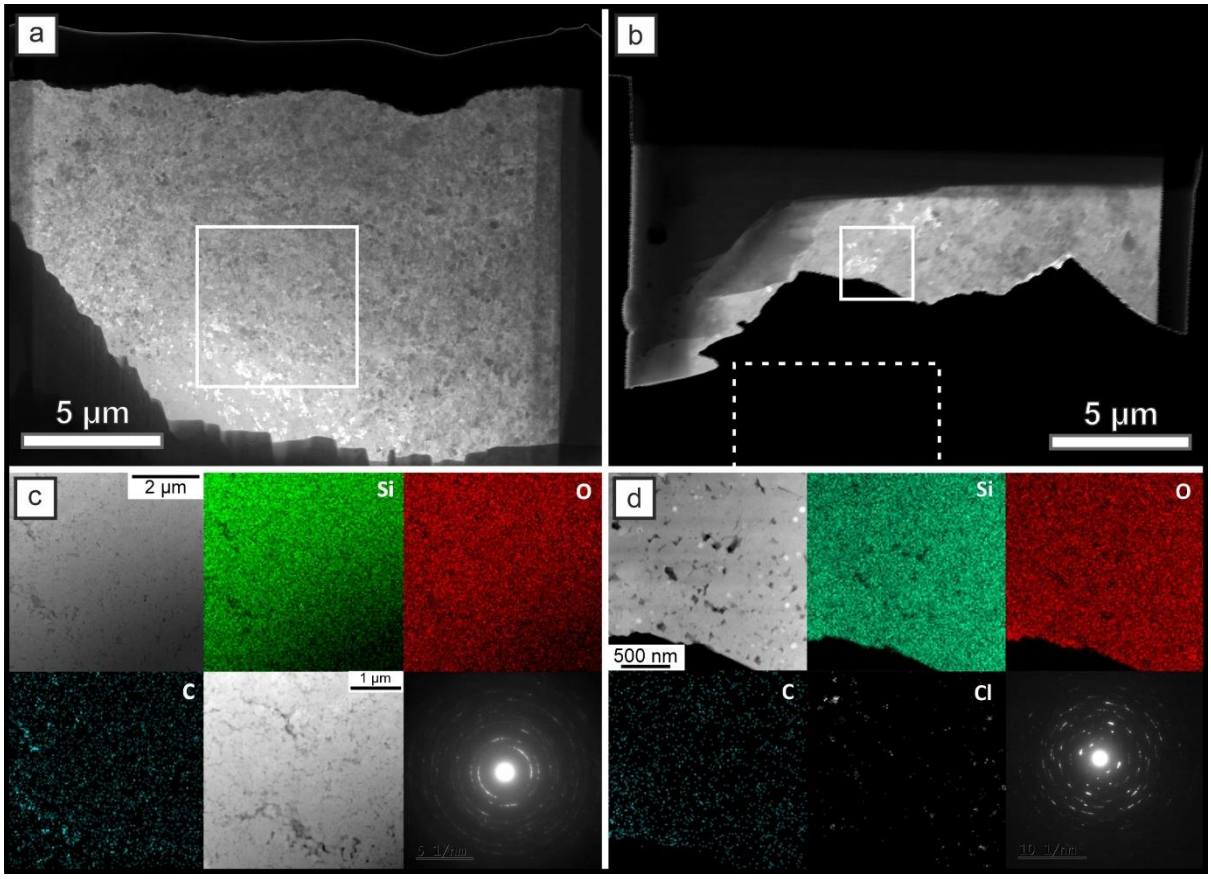
a
5 µm
b
5 µm
c
2 µm
Si
O
C
1 µm
d
Si
O
500 nm
C
Cl

**Table 1:** Sedimentology, diagenetic context and appearance of organic microfossils in Angmaat cherts. UOM: unrecognizable organic material; gy: gypsum; chc: chalcedony; qz: quartz; dol: dolomite.

| Sample | Lithology | primary sedimentary | secondary diagenetic | Microfossils and OM |
|---|---|---|---|---|
| WWB 17-10 | chert, minor dolomite | wavy lamination | pseudomorphs: gy | none |
| | | | laminated chert | filamentous, UOM |
| | | | laminated dolomite | UOM |
| | | | void fillings: chc | minor UOM |
| | | | closed fractures | UOM |
| NL 17-M | chert, dolomite | laminated with nodules | pseudomorphs: gy, dol | none |
| | | | laminated chert | coccoidal, UOM |
| | | | laminated dolomite | UOM |
| | | | nodular chert | coccoidal, UOM |
| | | | chert spherules | UOM |
| | | | void fillings: chc | UOM |
| | | | closed fractures | UOM |
| NL 17-N | chert | laminated with minor nodules | pseudomorphs: gy | none |
| | | | laminated chert | coccoidal, filamentous, UOM |
| | | | nodular chert | coccoidal, UOM |
| | | | void fillings: qz, chc, dol | minor UOM |
| | | | closed fractures | UOM |
| WWB 17-5 | chert, dolomite | nodular | pseudomorphs: dol, gy | none |
| | | | nodular chert | coccoidal, minor filamentous, UOM |
| | | | nodular dolomite | UOM |
| | | | chert spherules | UOM |
| | | | void fillings: chc, dol | in places filamentous and UOM |
| | | | Fracture filling dol | spherical organic structures |
| | | | stylolites in dolomite | UOM |

**Table 2:** Summery of peak decomposition procedures and extracted and calculated Raman parameters.

| Decomposition procedure | Peaks with starting position | Extracted parameters | Calculated parameters |
|---|---|---|---|
| No decomposition | none | Intensity of 1350 and 1600 $cm^{-1}$ maxima<br>Intensity at 1540 $cm^{-1}$<br>FWHM of 1600 $cm^{-1}$ maximum | Intensity ratio I-1600/I-1350<br>Intensity ratio I-1540/I-1600 |
| 4-peak decomposition after Kouketsu et al., 2014 | D1 - 1350 $cm^{-1}$<br>D2 - 1600 $cm^{-1}$<br>D3 - 1510 $cm^{-1}$<br>D4 - 1245 $cm^{-1}$ | FWHM-D1<br>FWHM-D2 | T-D1 (°C) = -2.15(FWHM-D1) + 478 |
| 5-peak decomposition after Delarue et al., 2016 | D1 - 1350 $cm^{-1}$<br>D2 - 1620 $cm^{-1}$<br>D3 - 1500 $cm^{-1}$<br>D4 - 1200 $cm^{-1}$<br>G - 1580 $cm^{-1}$ | Intensity of D1 and G<br>FWHM-D1 and -G | Intensity ratio $R1_{(5p)}$ = D1/G |
| 7-peak decomposition | D1 - 1340 $cm^{-1}$<br>D2 - 1610 $cm^{-1}$<br>D3 - 1415 $cm^{-1}$<br>D3' - 1540 $cm^{-1}$<br>D4 - 1165 $cm^{-1}$<br>D5 - 1230 $cm^{-1}$<br>G - 1570 $cm^{-1}$ | Intensity of D1, G and D3<br>FWHM-D1 and -D2<br>Position of G peak | Intensity ratios $R1_{(7p)}$ = D1/D2 and $R3_{(7p)}$ = D3/D2 |
| Decomposition 633 nm spectra after Ferralis et al., 2016 | D1 - 1330 $cm^{-1}$<br>D3 - 1400 $cm^{-1}$<br>D3' - 1500 $cm^{-1}$<br>D4 - 1150 $cm^{-1}$<br>D5 - 1260 $cm^{-1}$<br>(G+D2) - 1600 $cm^{-1}$ | Intensity of D1, D2, D4, D5 and (G+D2) | Intensity ratios D1/(G+D2) and (D4+D5)/(G+D2)<br>Ratios H:C = 0.871 * D5/(G+D2) - 0.0508 and H:C = 0.6024 * (D4+D5)/(G+D2) - 0.0739 |

**Table 2:** Raman parameters of OM measured with 532 nm laser and sorted by sample in relation to taxonomic and diagenetic context. [1]after Kouketsu et al., 2014 to estimate maximum thermal alteration; [2]after Delarue et al., 2016 to estimate the degree of carbonization; [3]7-peak fit to visualize the progressive change of the D2-peak with increasing maturity; sph: chert spherules; cod: coccoids; SOS: spherical organic structures. For spectral shapes (S4 and S1) see Figure 8. Errors are standard deviations of given parameter.

| Sample | context | n | no fitting | | | 4-peak-fit+ | | | 5-peak fit* | | | 7-peak fit | | | | |
|---|---|---|---|---|---|---|---|---|---|---|---|---|---|---|---|---|
| | | | 1600/1350 | 1540/1600 | FWHM-D2 | FWHM-D1 | FWHM-D2 | T-D1 (°C) | $R1_{(5p)}$ | FWHM-D1 | FWHM-G | $R1_{(7p)}$ | $R3_{(7p)}$ | FWHM-D1 | FWHM-D2 | G-position |
| WWB-17-10 | filaments | 22 | 1.41±0.03 | 0.29±0.01 | 52.1±3.4 | 103.9±6.8 | 48.4±3.4 | 254.6±14.7 | 1.73±0.16 | 110.9±11.8 | 81.9±14.6 | 0.77±0.03 | 0.33±0.02 | 90.9±4.5 | 40.5±1.9 | 1570.4±2.7 |
| | UOM-chert | 11 | 1.81±0.09 | 0.27±0.03 | 49.3±2.1 | 109.7±5.7 | 48.7±5.5 | 242.3±12.3 | 1.49±0.22 | 128.7±8.9 | 61.8±9.3 | 0.56±0.04 | 0.26±0.04 | 98.1±6.6 | 41.5±1.2 | 1573.2±2.1 |
| NL-17-M | coccoids | 12 | 1.23±0.03 | 0.47±0.02 | 65.4±2.8 | 113.9±4.2 | 63.6±2.7 | 232.9±8.9 | 2.03±0.23 | 148.7±5.2 | 126.4±11.3 | 0.94±0.03 | 0.47±0.02 | 107.4±4.7 | 56.5±3.1 | 1555.2±2.2 |
| | UOM | 10 | 1.19±0.02 | 0.59±0.04 | 79.4±4.1 | 138.0±7.7 | 79.9±4.3 | 181.3±16.6 | 1.89±0.1 | 148.7±9.8 | 102.9±22.5 | 1.05±0.05 | 0.60±0.06 | 121.4±2.0 | 67.5±3.1 | 1551.6±2.4 |
| | UOM-chc | 14 | 1.21±0.03 | 0.54±0.03 | 76.3±4.3 | 129.0±5.1 | 72.4±3.7 | 200.6±11.0 | 1.94±0.12 | 139.6±5.5 | 103.3±9.8 | 1.02±0.03 | 0.54±0.03 | 114.5±5.4 | 64.4±1.6 | 1550.5±1.9 |
| | UOM-gl | 10 | 1.33±0.08 | 0.43±0.09 | 67.5±6.5 | 119.2±11.3 | 60.6±9.4 | 221.6±24.3 | 1.65±0.18 | 128.8±15.9 | 100.8±24.1 | 0.88±0.08 | 0.43±0.08 | 102.6±10.9 | 53.7±8.5 | 1560.0±4.9 |
| NL-17-N | coccoids | 27 | 1.23±0.02 | 0.50±0.01 | 69.4±1.3 | 121.8±4.7 | 66.9±2.5 | 216.2±10.0 | 1.77±0.18 | 132.8±4.6 | 116.9±8.2 | 0.96±0.02 | 0.51±0.02 | 112.4±2.9 | 61.8±2.7 | 1555.6±2.7 |
| | filaments | 17 | 1.46±0.04 | 0.48±0.02 | 68.5±5.2 | 126.3±10.1 | 69.3±2.5 | 206.6±21.7 | 1.51±0.16 | 146.0±6.4 | 76.1±11.8 | 0.78±0.04 | 0.45±0.05 | 122.5±4.9 | 57.6±3.3 | 1561.8±4.5 |
| | UOM | 20 | 1.45±0.02 | 0.48±0.02 | 66.2±3.3 | 118.1±11.2 | 67.7±3.0 | 223.9±24.0 | 1.56±0.17 | 143.9±10.6 | 84.8±7.9 | 0.80±0.03 | 0.44±0.02 | 116.6±7.8 | 58.2±1.9 | 1558.7±2.8 |
| WWB-17-5 | filaments | 25 | 1.44±0.21 | 0.40±0.07 | 63.7±9.1 | 116.4±8.7 | 57.4±6.4 | 227.8±18.7 | 1.64±0.30 | 129.1±8.3 | 90.9±29.8 | 0.80±0.16 | 0.39±0.09 | 102.4±8.1 | 52.1±6.7 | 1561.2±8.6 |
| | SOS-dol | 21 | 1.63±0.23 | 0.27±0.08 | 50.8±7.0 | 110.5±9.4 | 46.1±7.2 | 240.5±20.2 | 1.52±0.23 | 127.8±8.0 | 59.7±20.6 | 0.66±0.12 | 0.27±0.08 | 96.9±9.8 | 39.4±4.8 | 1567.7±5.4 |
| | UOM | 30 | 1.25±0.08 | 0.38±0.06 | 65.8±6.0 | 112.8±7.2 | 56.4±3.6 | 235.6±15.6 | 1.78±0.17 | 121.8±6.7 | 102.5±18.4 | 0.92±0.07 | 0.40±0.04 | 100.2±8.3 | 50.3±3.4 | 1559.8±3.7 |
| 17-5A | cod-chert | 54 | 1.56±0.31 | 0.27±0.10 | 52.9±10.3 | 105.8±8.6 | 46.7±9.9 | 250.6±18.5 | 1.48±0.39 | 122.1±8.1 | 66.1±33.3 | 0.72±0.18 | 0.31±0.18 | 90.3±11.1 | 39.9±8.0 | 1570.7±7.7 |
| 17-5B | cod-chert | 65 | 1.51±0.31 | 0.27±0.11 | 62.8±12.9 | 105.3±7.1 | 47.4±7.9 | 251.5±15.2 | 1.56±0.39 | 116.1±8.7 | 73.6±33.1 | 0.71±0.15 | 0.27±0.10 | 95.6±9.2 | 40.2±5.8 | 1570.4±6.2 |
| 17-5A | high mature | 20 | 1.89±0.18 | 0.15±0.02 | 42.8±3.8 | 102.2±10.5 | 37.2±4.3 | 258.3±22.5 | 1.21±0.29 | 117.4±9.5 | 32.9±5.8 | 0.53±0.08 | 0.17±0.03 | 80.5±6.3 | 32.0±4.1 | 1578.2±4.1 |
| | low mature | 19 | 1.32±0.09 | 0.38±0.03 | 60.4±5.7 | 114.4±4.3 | 56.8±2.7 | 231.9±9.3 | 1.67±0.29 | 127.2±7.0 | 99.7±16.6 | 0.87±0.08 | 0.42±0.05 | 103.4±6.9 | 46.4±2.2 | 1563.3±2.6 |
| 17-5B | high mature | 22 | 1.86±0.17 | 0.14±0.01 | 41.8±5.0 | 101.6±10.2 | 36.4±4.8 | 259.5±21.9 | 1.04±0.19 | 114.0±12.3 | 34.1±3.7 | 0.53±0.07 | 0.15±0.02 | 84.1±6.5 | 32.6±3.2 | 1578.5±2.0 |
| | low mature | 27 | 1.23±0.10 | 0.38±0.03 | 61.5±2.8 | 112.9±7.4 | 56.8±3.3 | 235.1±15.9 | 1.85±0.27 | 120.8±6.1 | 102.4±19.6 | 0.93±0.08 | 0.39±0.05 | 102.9±6.2 | 48.9±3.4 | 1562.2±3.8 |

**Table 3:** Overview of parameters and H:C ratios extracted from 633 nm Raman spectra of OM. For spectral shapes (S4 and S1) see Figure 8. Errors are standard deviations of given parameters.

| Sample | context | n | D1/(G+D2) | FWHM-D1 | D5/(G+D2) | (D4+D5)/(G+D2) | H:C-D5 | H:C-D4+D5 |
|---|---|---|---|---|---|---|---|---|
| WWB-17-5 | filaments | 4 | 0.81±0.13 | 88.61±3.42 | 0.49±0.046 | 0.69±0.051 | 0.38±0.04 | 0.34±0.031 |
| | SOS-dol | 18 | 0.88±0.09 | 89.68±5.59 | 0.46±0.06 | 0.67±0.089 | 0.35±0.052 | 0.33±0.054 |
| | UOM | 17 | 1.01±0.05 | 88.75±6.93 | 0.53±0.036 | 0.76±0.053 | 0.41±0.031 | 0.38±0.032 |
| 17-5A | cod-chert | 54 | | | 0.48±0.053 | 0.69±0.084 | 0.37±0.056 | 0.34±0.051 |
| 17-5B | cod-chert | 65 | | | 0.51±0.041 | 0.75±0.077 | 0.39±0.036 | 0.38±0.046 |
| 17-5A | S4 | 20 | 0.73±0.04 | 84.35±5.88 | 0.43±0.036 | 0.59±0.049 | 0.32±0.032 | 0.28±0.029 |
| | S1 | 19 | 0.98±0.06 | 90.33±5.14 | 0.51±0.037 | 0.75±0.042 | 0.40±0.032 | 0.38±0.025 |
| 17-5B | S4 | 22 | 0.72±0.05 | 81.18±4.72 | 0.42±0.039 | 0.60±0.045 | 0.31±0.034 | 0.29±0.027 |
| | S1 | 27 | 1.00±0.06 | 92.30±4.87 | 0.52±0.039 | 0.75±0.06 | 0.40±0.034 | 0.38±0.036 |

**Supplementary material for:**

**Structural and chemical heterogeneity of Proterozoic organic microfossils of the ca. 1 Ga old Angmaat Formation, Baffin Island, Canada**

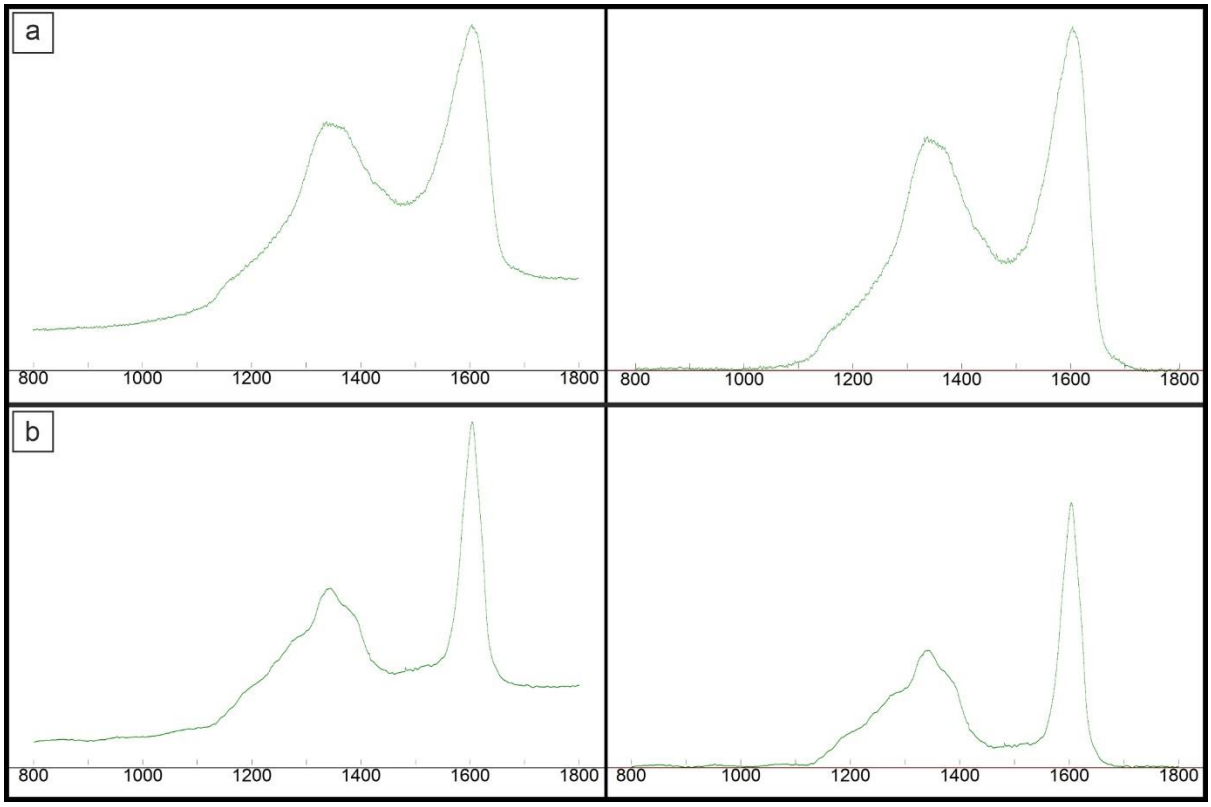


**Supplementary Figure 1:** Raman spectra from Angmaat chert before and after baseline correction was applied. (a): Raman spectrum of spectral shape S1 indicating lower mature OM. (b): Raman spectrum of spectral shape S4 indicating higher mature OM.

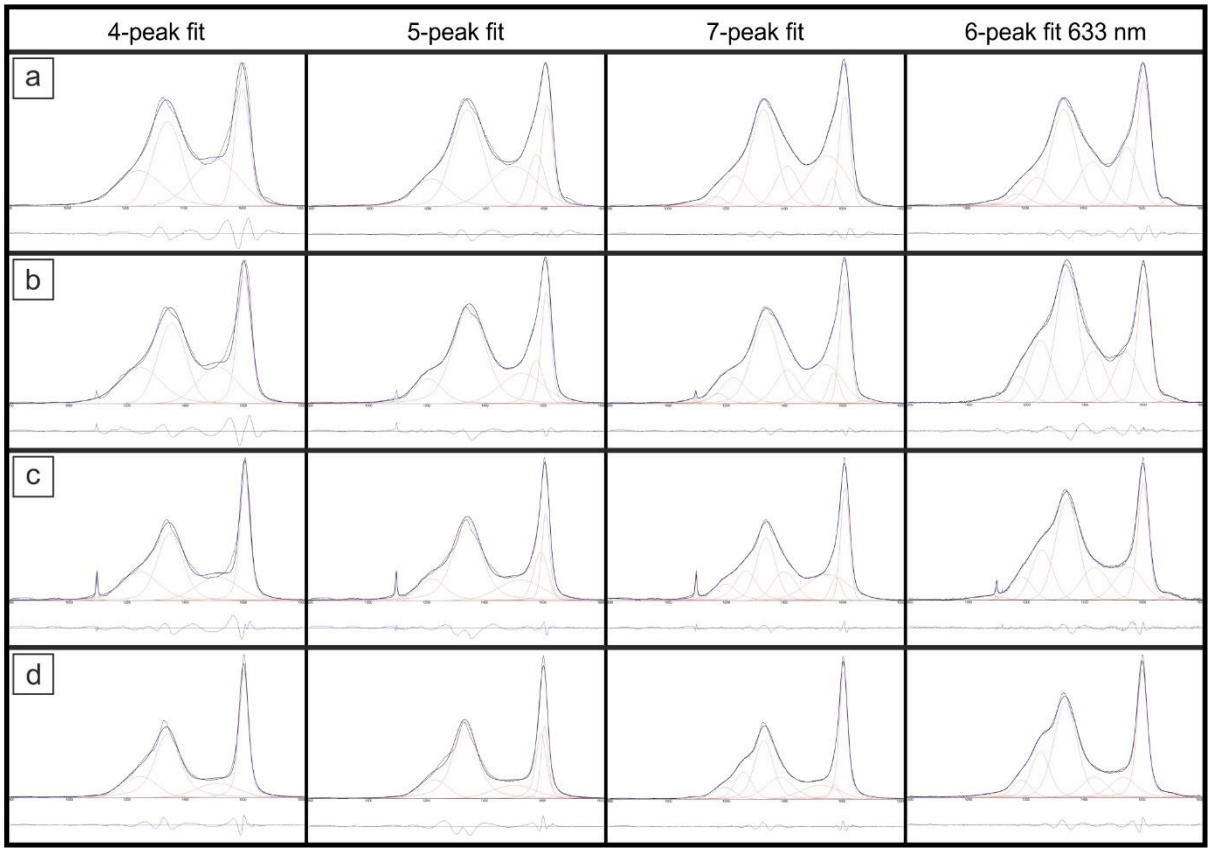


**Supplementary Figure 2:** Raman spectra from Angmaat chert showing spectral shapes S1 - S4 (a – d, black lines) with fitting procedures used for spectral decomposition (red peaks), decomposition results (blue lines) and difference spectra below each fitted spectrum.

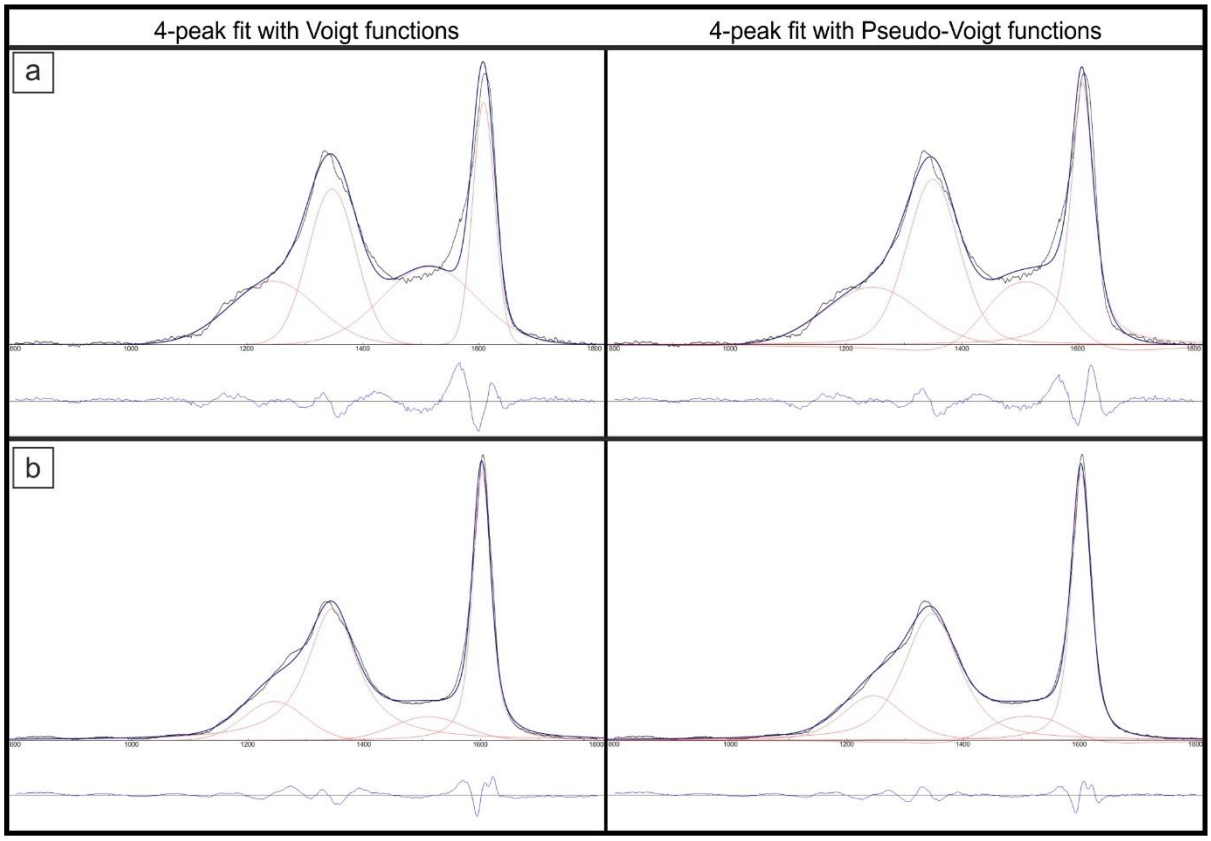


**Supplementary Figure 3:** Peak fitting of Raman-spectra of low mature **(a):** and high mature **(b):** OM from Angmaat chert according to fitting procedure G of Kouketsu et al., 2014 using Voigt functions (left) and Pseudo-Voigt functions (right). Note the negative excursions of the D3-peak resulting from the use of Pseudo-Voigt functions.

**Micro-XRF mapping:**

µ-XRF mapping was performed using the Bruker Tornado M4 micro-X-ray fluorescence analyzer of the department of Geosciences of the Friedrich-Schiller-University in Jena. We used the ca. 2 x 4 cm large billets of the respective thin sections NL-17-M, NL-17-N, WWB-17-10 and WWB-17-5A to determine the elemental composition and the distribution of the detected elements of the analyzed material. Elemental maps were recorded with spot size of 20 µm and a step sizes of ca. 27 µm at a dwell time of 35 ms at each spot. The current was set to 200 µA at a voltage of 50 kV and the sample chamber was evacuated to an air pressure of 20 mbar. The detection limit of this method is ca. 0.1 w%

All samples show Si as most common element without overlap with other detected elements and therefore indicative of the broadly siliceous (quartz) composition of the analyzed material. Other detected major elements are Ca, Mg, Fe, and S are all displayed in Supplementary Figures 4 and 5. Elements like Al, Mn and Ti are detected as minor components mostly concentrated in few small spots and are not shown here. In all analyzed samples Ca and Mg largely overlap as typical for a dolomitic composition with minor contents of Fe and S as indicated by a faint signal of these elements that overlaps with the stronger Ca and Mg signals. Stronger signals of S appear spotty throughout all samples and overlap mostly with similarly strong Fe signals indicative of small pyrite grains. However, a few larger spots enriched in S also overlap with Ca indicating a $CaSO_4$ composition (Supplementary Figure 4). This material is strictly limited to fracture fillings and the exact mineralogical composition of

this phase cannot be inferred. Apart from the appearance of Fe in the dolomitic phase and as potential pyrite it appears also as strong signal at thin laminations in and close to the dolomitic areas. Petrographic microscopy shows that such areas are composed of a brown mineral phase and with the exclusive appearance of Fe in this area in the µ-XRF maps this mineral phase is most likely an iron-oxide such as hematite.

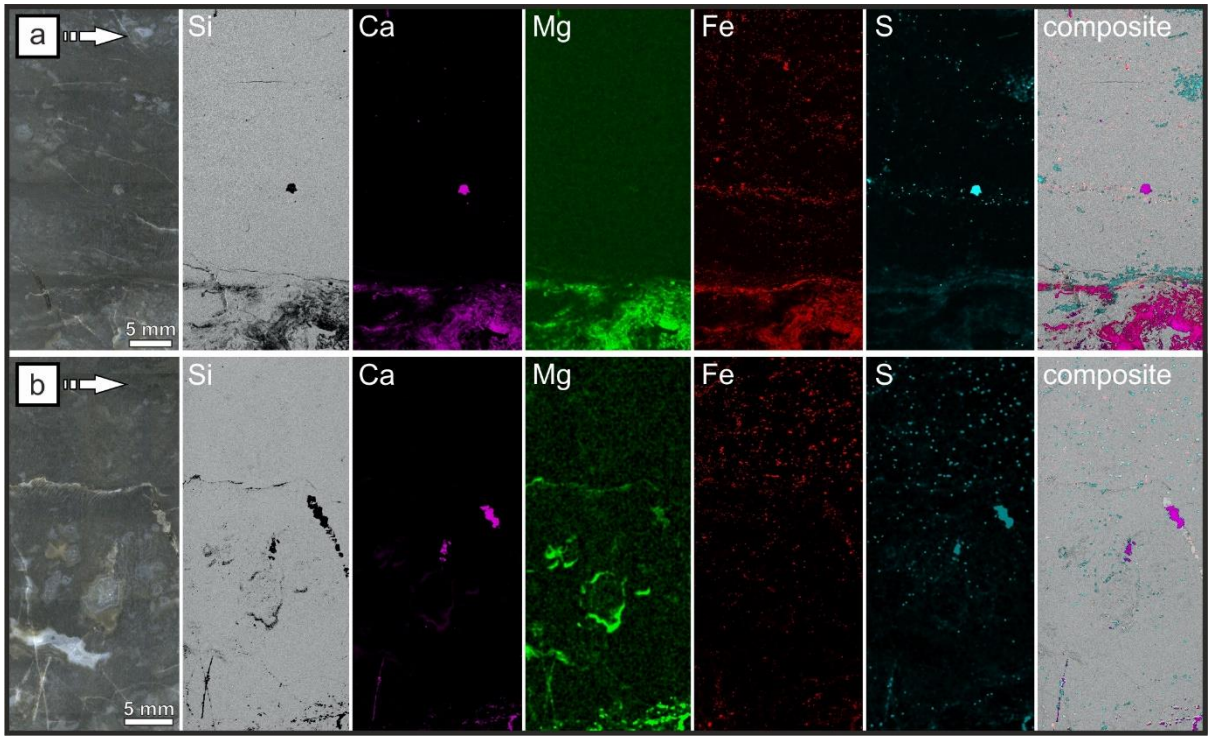


**Supplementary Figure 4:** µ-XRF element maps of black chert samples from the Angmaat Formation. **(a+b):** From left to right: Overview image of scanned billet (the scale applies to all images), elemental maps (Si, Ca, Mg, Fe and S) and composite map of elements to visualize minerals. Minerals inferred from the element maps are quartz (dark gray), dolomite (purple), pyrite (light blue) and iron oxides (pale red). The overlapping areas with Ca and S are $CaSO_4$-rich fracture fillings **(a):** Sample NL-17-M, laminated chert with few chert nodules. **(b):** Sample NL-17-N, laminated chert with few nodules and numerous up to 5 mm large chalcedony and dolomite filled voids. Note the Mg enrichment on the edges of the voids.

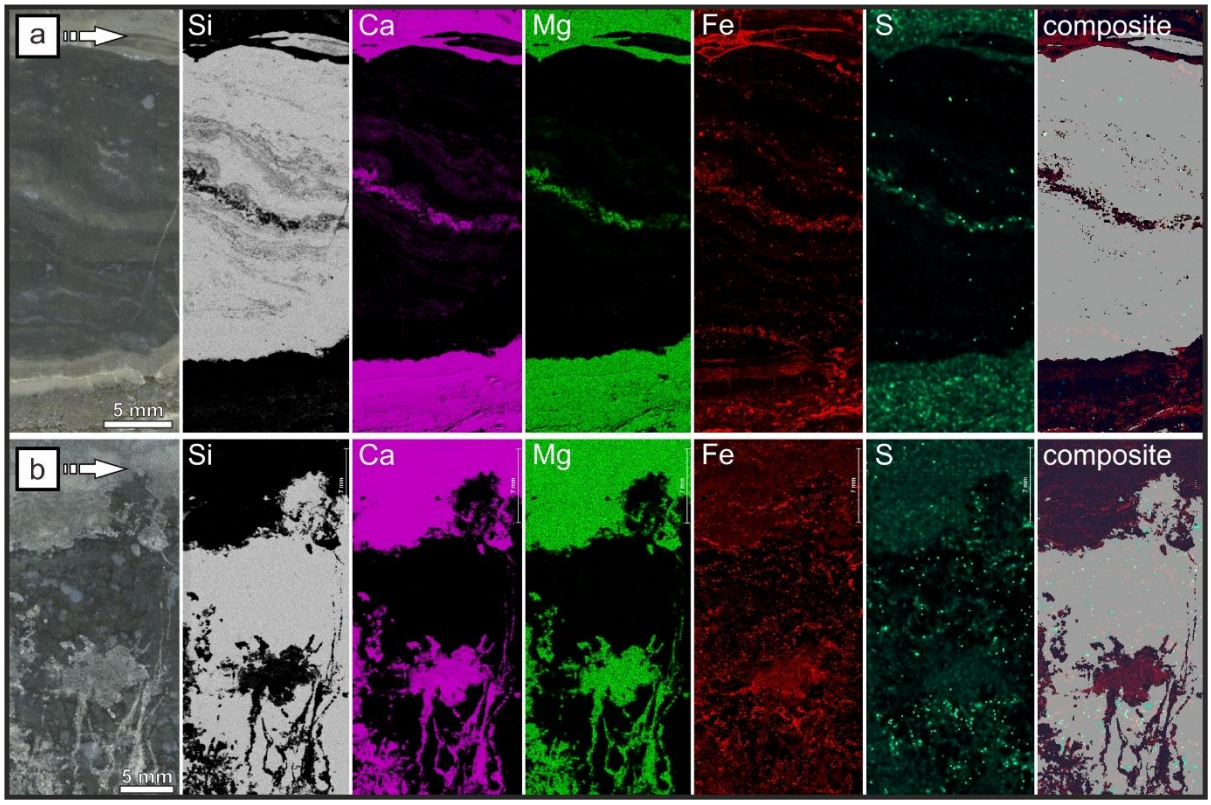


**Supplementary Figure 5:** µ-XRF element maps of black chert samples from the Angmaat Formation. **(a+b):** From left to right: Overview image of scanned billet (the scale applies to all images), elemental maps (Si, Ca, Mg, Fe and S) and composite map of elements to visualize minerals. Minerals inferred from the element maps are quartz (dark gray), dolomite (dark blue), pyrite (light blue) and iron oxides (red). The S in the Ca and Mg rich areas is indicative of minor portions of sulfate **(a):** Sample WWB-17-10, a wavy laminated chert. **(b):** Sample WWB-17-5A, a nodular chert with sub-vertical dolomite fractures.

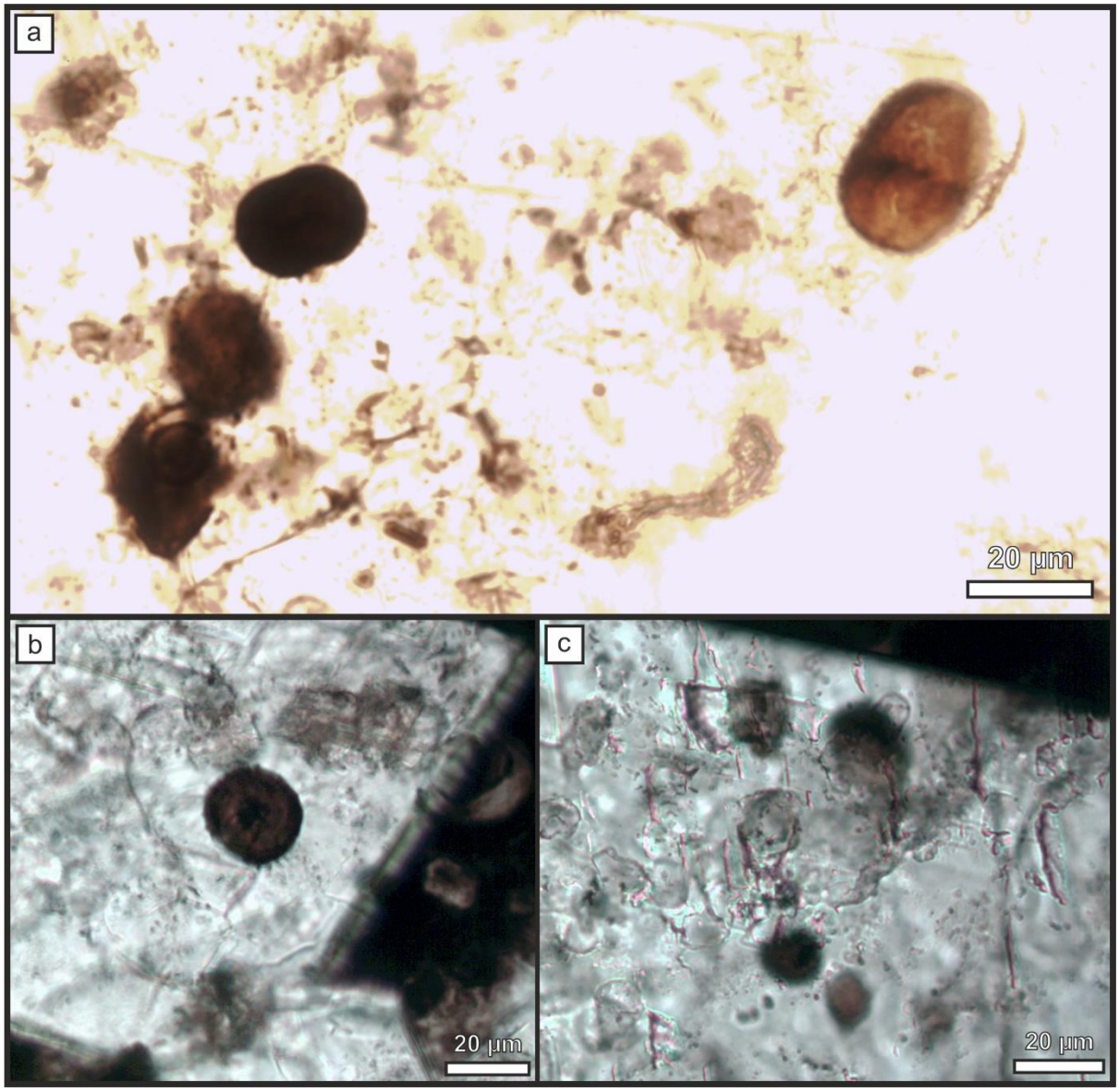


**Supplementary Figure 6:** Spherical organic structures (SOS) in secondary dolomite in sample WWB-17-5. Structures shown in a and b show internal textures that might indicate their origin as coccoidal microfossils while SOS in c show no internal textures and are more likely chert spherules coated by organic matter.

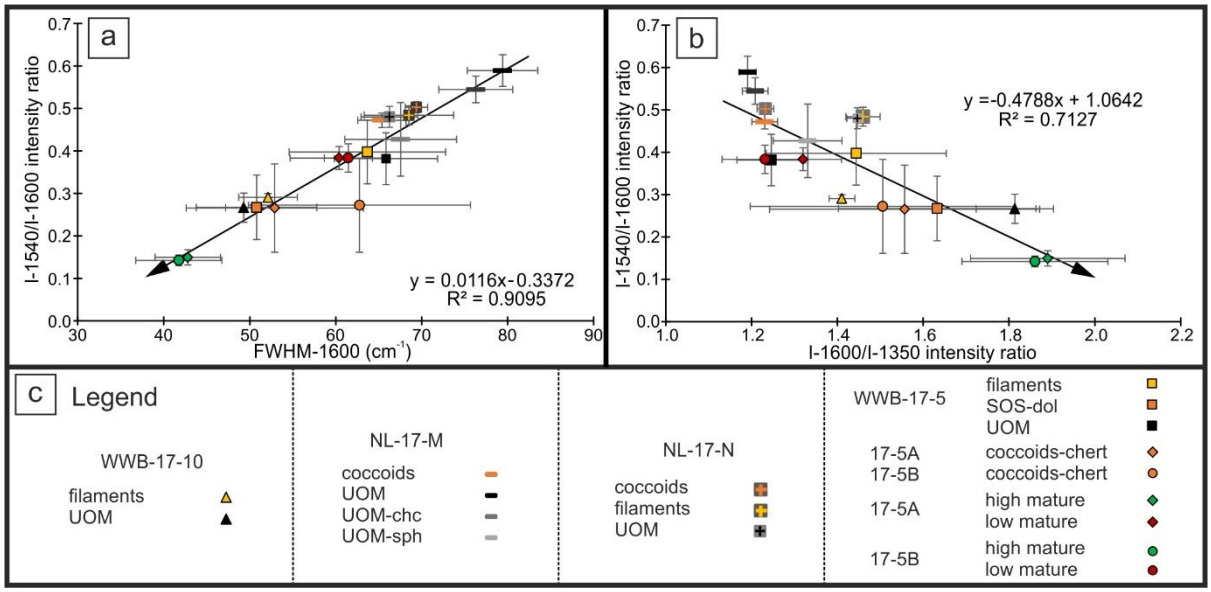


**Supplementary Figure 7:** Raman-parameters extracted prior to peak-fitting of Raman-spectra of OM obtained with 533 nm laser. **(a):** FWHM-1600 $cm^{-1}$ vs. intensity ratio I-1540/I-1600. **(b):** Intensity ratio I-1600/I-1350 vs. intensity ratio I-1540/I-1600. **(c):** Legend for a and b. **Note:** Black arrows in plots shows the approximate development of parameters with increasing maturity of organic matter.

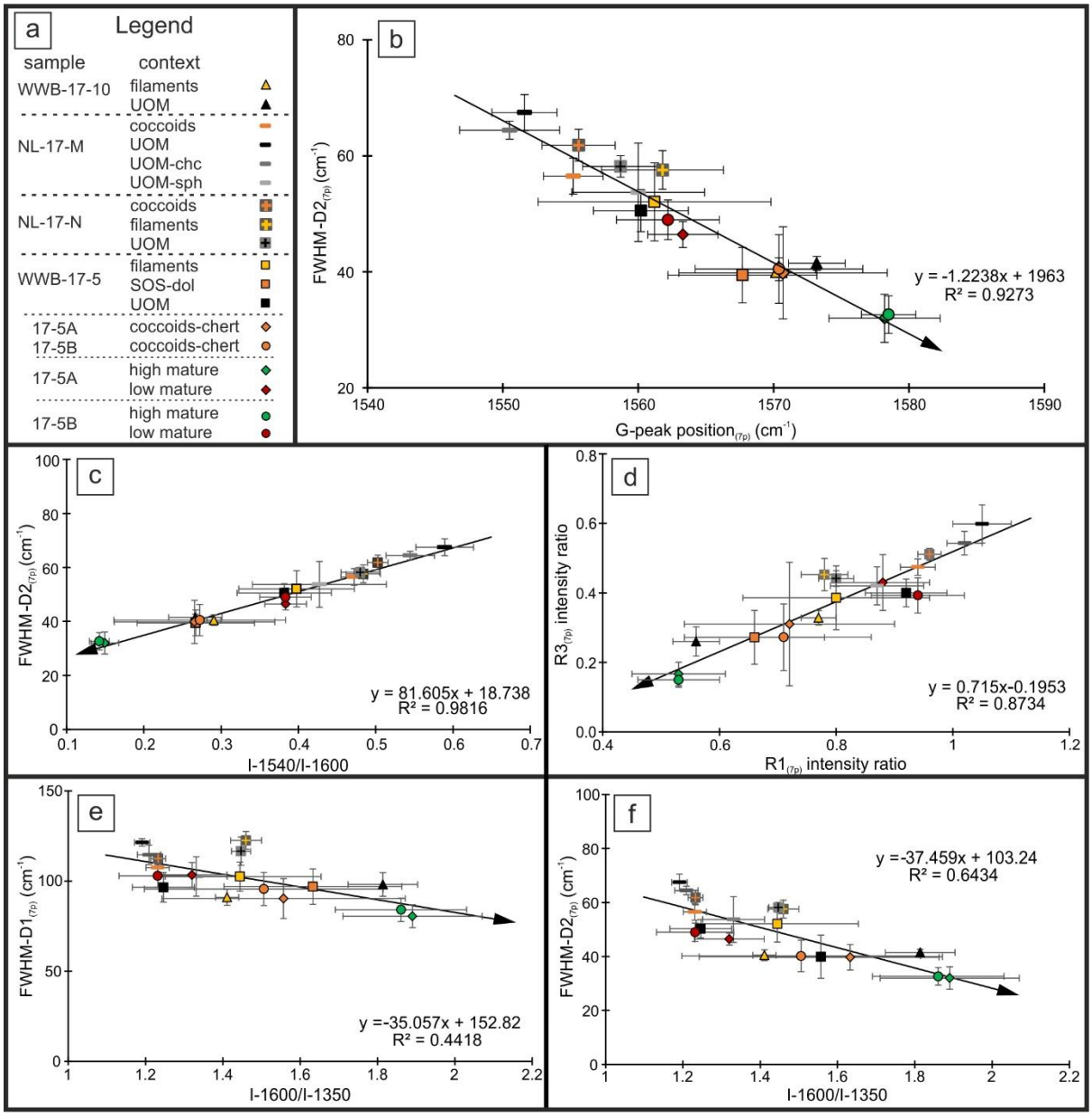


**Supplementary Figure 8:** Raman-parameters extracted prior to peak-fitting and from 7-peak fitting procedure of Raman-spectra OM obtained with 533 nm laser. **(a):** Legend for b - f. **(b):** FWHM-D2 vs. G-peak position of 7-peak fitting procedure. **(c):** FWHM-D2 of 7-peak fit vs. intensity ratio I-1540/I-1600. **(d):** R1 vs. R3 ratios extracted from 7-peak fitting procedure. **(e):** Intensity ratio I-1600/I-1350 vs. FWHM-D1 of 7-peak fit. (f): Intensity ratio I-1600/I-1350 vs. FWHM-D2 extracted from 7-peak fit. **Note:** Black arrows in plots shows the approximate development of parameters with increasing maturity of organic matter. Plots in b -d show a good linear correlation between parameters while linear correlations in plots in e and f are less well pronounced similar to Plots shown in Figure 9c-f.

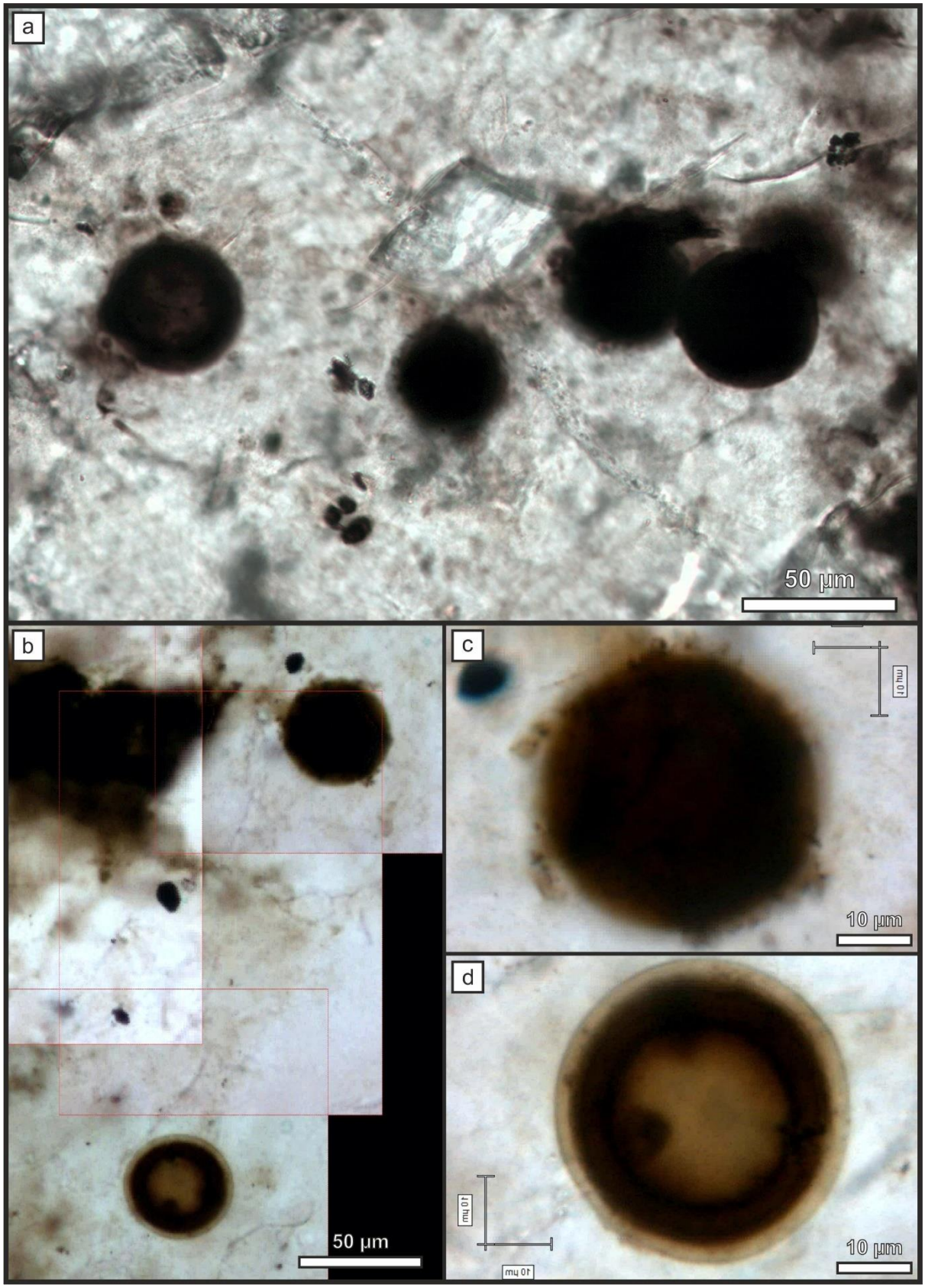


**Supplementary Figure 9**: Coccoidal microfossils from sample WWB-17-5 used for STXM analysis in their preservation context. (a): Small colony of four coccoidal microfossils preserved in chert most likely individuals of Gloeodiniopsis sp. The microfossil to the right shows potential cellular structures.

The microfossils chosen for STXM analysis is in the center of the image. **(b-d):** Two potential individuals of Gloeodiniopsis sp. preserved in chert. The individual shown in (c) was chosen for STXM-analysis while the neighboring individual in (d) clearly shows preserved internal cellular structures.

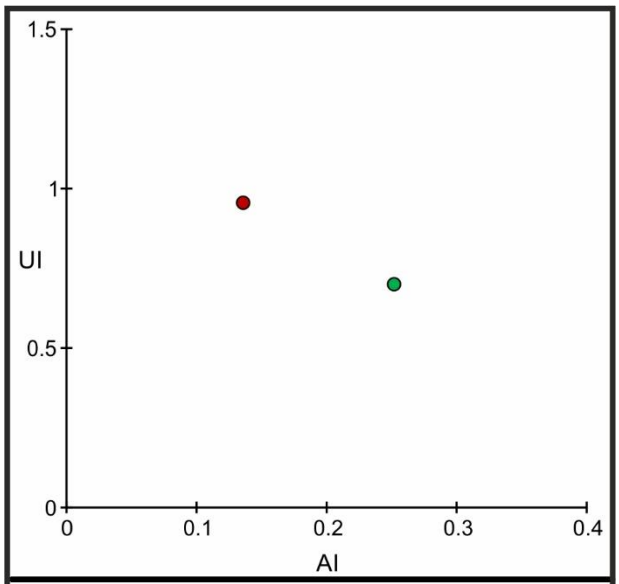


| Sample | AI | UI |
|---|---|---|
| microfossil-A | 0.136 | 0.955 |
| microfossil-B | 0.252 | 0.699 |

**Supplementary Figure 10:** Chemical variation of organic microfossils detected by STXM-mapping and represented by the aromaticity index (AI) plotted against the unsaturated index (UI) both extracted from NEXAFS spectra shown in Figure 14c and d.

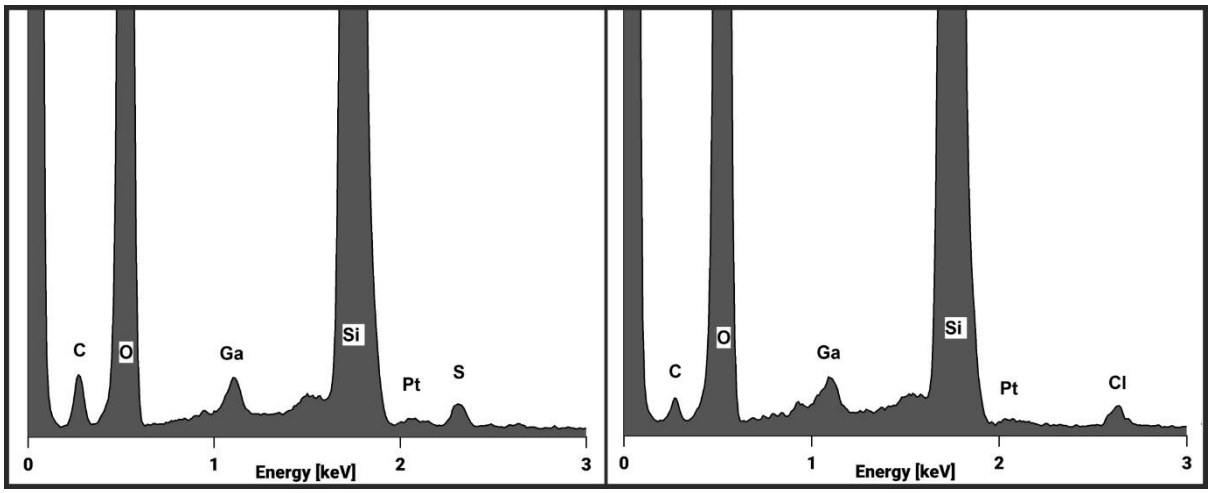


**Supplementary Figure 11:** TEM-EDX spectra of mapped areas from microfossil-A (left) and -B (right). Both samples show mostly Si and O with minor amounts of C, S and Cl. Ga and Pt are relicts from using a platinum strap to fix the sample on the sample holder.

**Supplementary Table 1:** Functional carbon groups and respective peak-positions in NEXAFS spectra after Alleon et al. (2017) and Bonneville et al. (2020).

| Functional group | Fit position (eV) |
|---|---|
| aromatic | 284 |
| quinones | 284.4 |
| aromatic/olefinic | 284.9 |
| aromatic | 285.4 |
| imines | 285.8 |
| ketone/phenol | 286.2 |
| ketone/phenol | 286.6 |
| ketone/phenol | 287.1 |
| aliphatic | 287.6 |
| amide | 288.2 |
| carboxylic | 288.6 |
| aldehydes | 289.1 |
| aliphatic | 289.9 |